

When Geometry Radiates Review

Gravitational Waves in Theory, Cosmology, and Observation

Azadeh Maleknejad^{a,b,c}

^a*Centre for Quantum Fields and Gravity, Swansea University, Swansea SA2 8PP, United Kingdom*

^b*Deutsches Elektronen-Synchrotron DESY, Notkestraße 85, 22607 Hamburg, Germany*

^c*Institute of Theoretical Physics, Universität Hamburg, 22761 Hamburg, Germany*

E-mail: azadeh.maleknejad@swansea.ac.uk

ABSTRACT: Gravitational waves provide a unique window into gravity, cosmology, and high-energy physics, enabling the exploration of fundamental phenomena across a wide range of scales. This review presents a coherent and pedagogical framework that bridges foundational theory with observational frontiers. We begin by developing the theory of gravitational radiation within linearized general relativity, deriving gravitational waves as solutions to the linearized Einstein equations and clarifying their physical interpretation, polarization states, and key properties. We then deepen the discussion through a more rigorous geometric perspective, tracing the connection between gravitational radiation and the algebraic structure of the Weyl tensor. This naturally leads to the Bondi–Sachs formalism, which provides a precise definition of gravitational waves in asymptotically flat spacetimes and establishes their role as genuine carriers of energy and angular momentum. Extending beyond flat backgrounds, we examine gravitational waves in an expanding universe, following their evolution across cosmological epochs and their generation during inflation. Within this setting, we explore adiabatic modes and consistency relations, which illuminate the infrared structure and universal behavior of long-wavelength perturbations, and derive the inflationary spectrum of vacuum gravitational waves together with their contribution to the integrated Sachs–Wolfe effect. The review further surveys the main observational strategies for detecting gravitational waves across a broad frequency range, including cosmic microwave background polarization, pulsar timing arrays, laser interferometers on Earth and in space, and resonant cavity–based detectors. We then discuss the astrophysical and cosmological mechanisms responsible for generating gravitational radiation. We conclude by summarizing the current status of the field and outlining promising directions for future theoretical and observational developments.

KEYWORDS: Gravitational radiation, Asymptotically flat space, Cosmology, Geometrical & algebraic aspects of gravitational waves, Sources of gravitational waves, Detection of gravitational waves

Contents

1	Introduction and Motivation	1
2	Linearized General Relativity and GWs	5
2.1	The Weak-Field Approximation and Wave Solutions	6
2.1.1	Gravitational Radiation of Compact Objects	8
2.2	Polarization States of GWs and Free Particles	12
2.2.1	Geodesic Distortion by Passing GWs	13
3	Theoretical Aspects of Gravitational Waves	16
3.1	Theoretical Issues of Linear Gravity	16
3.2	The Weyl Tensor: Geometry of Tidal Forces	17
3.3	When Geometry Radiates: Defining Gravitational Waves	22
3.3.1	GWs Carry Energy	27
3.3.2	GWs Carry Angular Momentum	27
3.4	At the Edge of Spacetime: From Poincaré to BMS	29
3.4.1	Asymptotic symmetries of Gravitational Fields	29
3.4.2	Why Radiative Spacetimes Have the Full BMS Group?	31
4	Expanding Universe and Gravitational Waves	33
4.1	Expansion History and Cosmological Eras	33
4.1.1	Cosmic Inflation	37
4.1.2	From the Inflationary Paradigm to Precision Cosmology	40
4.2	Inflation and GWs	41
4.3	IR Structure of Cosmological Perturbations	46
4.3.1	Adiabatic Modes in Cosmology	46
4.3.2	Maldacena’s Consistency Relation & Primordial Non-Gaussianity	50
4.4	Inflationary Gravitational Waves at Late Times	53
4.4.1	The Present-Day Spectrum of Gravitational Waves from Inflation	53
4.4.2	Integrated Sachs–Wolfe effect and Primordial GWs	57
5	Detection Techniques and Observational Frontiers	59
5.1	CMB Polarization: Imprints of Primordial Gravitational Waves	60
5.2	Pulsar Timing Arrays: Precision Cosmic Clocks for GW Detection	67
5.3	Laser Interferometry: Earth- and Space-Based GW Observatories	70
5.4	Photonic Qumodes: a Cutting-Edge Quantum Platform for GW Detection	75
6	Physical Mechanisms Driving Gravitational Radiation	84
6.1	Astrophysical Sources	85
6.1.1	Compact binary coalescences	85
6.1.2	Isolated neutron stars	86
6.1.3	Transient burst sources	87

6.1.4	Astrophysical Contributions to the Stochastic GW Background	87
6.2	Cosmological Sources	87
6.2.1	Inflation and Reheating	88
6.2.2	Cosmological Phase Transitions and Hydrodynamical Sources	92
6.2.3	Topological Defects	94
6.2.4	Primordial Black Holes and scalar-induced gravitational waves	95
7	Summary	96
	Acknowledgments	97

1 Introduction and Motivation

Gravitational waves (GWs) were first predicted by Einstein in 1916 as ripples in spacetime propagating at the speed of light, arising from the dynamical degrees of freedom of the metric in general relativity [1]. They embody a fascinating interplay of physics, mathematics, and phenomenology, yet their physical reality was debated for decades. In the 1930s, Einstein himself briefly doubted the physical reality of gravitational waves due to a misinterpretation of early solutions. He later revised his view, though questions about their true physicality remained. It wasn't until the 1950s, through the work of Bondi, Pirani, and others, that these issues were resolved. Bondi's analysis at null infinity demonstrated that gravitational waves carry energy and can have measurable physical consequences [2]. This marked the turning point in establishing gravitational waves as real, observable phenomena in general relativity that carry energy and angular momentum away from isolated systems.

With their physical interpretation rigorously established, attention turned toward their astrophysical sources and their detection. Indirect evidence arrived with the Hulse–Taylor binary pulsar in 1974 [3], whose orbital decay precisely matched the prediction for GW emission. Early detection efforts began with Weber's resonant bars and gradually evolved into large-scale interferometers, propelled by the vision of Weiss, Drever, and Thorne. These decades of theoretical and experimental progress culminated in the landmark direct detection by LIGO in 2015 [4], an achievement that inaugurated the era of GW astronomy.

Beyond established physics, gravitational waves provide a powerful probe of high-energy phenomena beyond the Standard Model (BSM) and a unique window into the unexplored frontiers of gravity and the early Universe. As messengers from the earliest moments of cosmic history, they access energy scales far beyond the reach of terrestrial accelerators, offering potential insights into new physics and even the quantum nature of spacetime. Stochastic gravitational wave backgrounds may originate from inflationary fluctuations [5, 6], violent post-inflationary dynamics such as preheating [7], or relics of high-energy phase transitions and topological defects [8, 9]. Intriguingly, in certain scenarios, GWs may not merely carry information about early-universe processes, they could

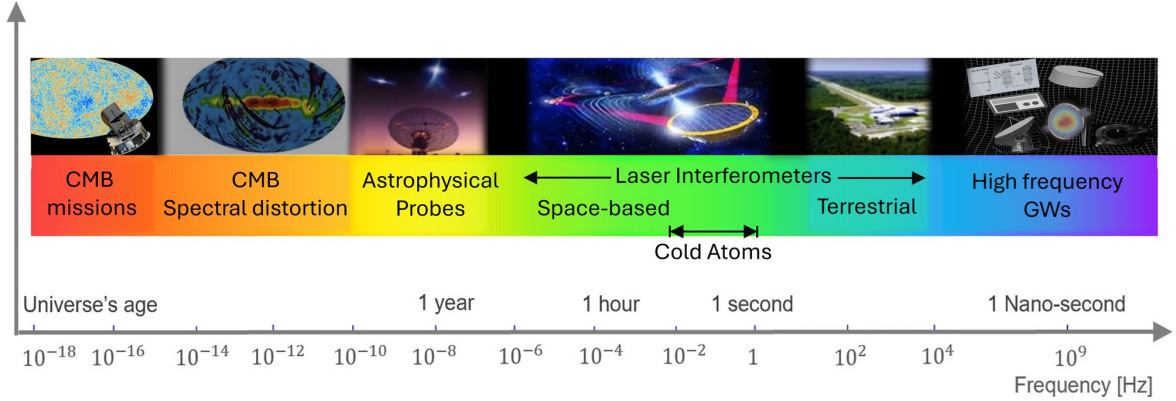


Figure 1: Gravitational rainbow. At the lowest frequencies, measurements of the cosmic microwave background (CMB) provide the most sensitive probe of gravitational waves. In the nanohertz range, pulsar timing arrays serve as powerful astrophysical detectors. At intermediate and frequencies as high as a few kilohertz, laser and atomic interferometers are actively probing the spectrum. Finally, we enter the realm of high-frequency gravitational waves above 10 kHz, where detection demands innovative techniques.

actively participate in its creation, potentially influencing the matter content of the Universe [10–21].

Just as electromagnetic radiation, gravitational waves possess their own spectrum (see Fig. 1). Although their frequency spectrum is, in principle, unbounded from above and below, only a finite range is observationally accessible. More precisely, their wavelengths are bounded below by the Hubble radius, corresponding to a minimum frequency of about 10^{-18} Hz, while detector sensitivity currently limits the upper end to 10 kHz range. Within this observational window, different frequency bands reveal complementary science: very-low-frequency GWs imprint the CMB polarization [22, 23]; nanohertz signals are tracked by pulsar timing arrays [24–26] and astrometric observations [27, 28]; millihertz waves will be measured by space interferometers such as LISA [29]; and the kilohertz regime is already accessed by ground-based detectors such as LIGO [4, 30, 31]. Future third-generation facilities, including the Einstein Telescope [32], promise even greater sensitivity. Atom interferometry offers a complementary pathway to laser interferometers for GW detection [33–35]. Terrestrial and space-based cold-atom concepts under development [36–46] aim to extend sensitivity into the mid-frequency band (10^{-2} –1 Hz), thereby bridging the gap between LISA and ground-based observatories. At the highest frequencies, innovative laboratory-scale concepts are being developed to extend gravitational wave sensitivity well beyond the MHz regime [47], including a number of novel approaches based on quantum-sensing techniques [48, 49]. This is not all: there are several further detectors and proposals for probing GWs across different frequency windows. For an overview of the global network of laser-interferometry detectors on Earth and in space, see Fig. 32. Together, these approaches build a multi-frequency gravitational wave astronomy, analogous to the multi-wavelength program of electromagnetic observations.



Figure 2: Timeline of GWs observatories from the first detection (Advanced LIGO, 2015) to planned facilities through the 2040s. Virgo joined in 2017 and KAGRA in 2020, establishing the first global ground-based network. Forthcoming projects—LIGO–India (early 2030s) [31], LiteBIRD (2032) [50], LISA (2035) [29], and the Einstein Telescope (expected from ~ 2035 –2040) [32]—extend coverage across frequency bands and improve sky localization, charting the roadmap for GW astronomy into the next decades.

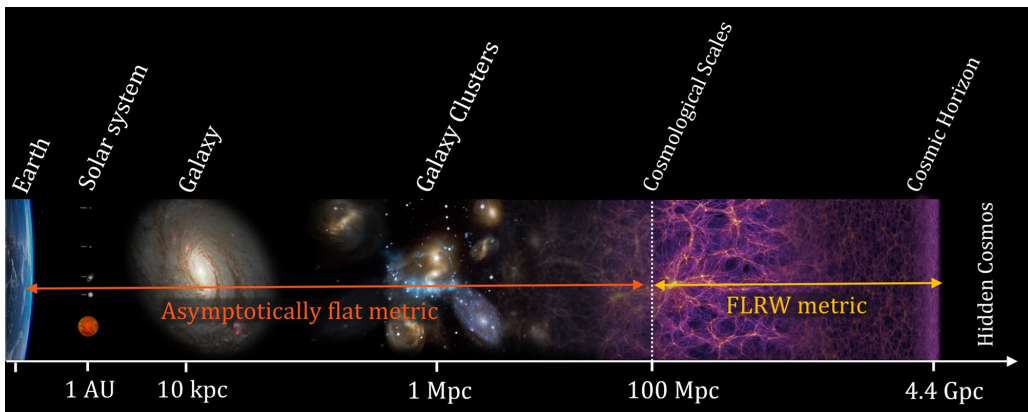


Figure 3: Hierarchy of astrophysical and cosmological scales. Observations reveal that our Universe is expanding and becomes statistically isotropic and homogeneous on scales larger than about 100 Mpc, defining the cosmological regime. Gravitational systems up to these scales are well described by asymptotically flat geometries, whereas on larger scales the spacetime must be modeled by the FLRW metric to capture the expansion of the Universe. The cosmic horizon marks the limit of observation, not the limit of existence.

Since gravitational waves are both generated and propagate through the gravitational backgrounds of the Universe, it is essential to describe them within the appropriate space-time geometry relevant to the physical scale under consideration. The behavior of gravity manifests differently across scales. On relatively small scales, up to roughly 100 Mpc, the expansion of the Universe is negligible, and gravitational dynamics can be accurately described within asymptotically flat geometries. On larger, cosmological scales, however, the expansion of space itself becomes dynamically relevant, and spacetime must instead be modeled by an FLRW background (see Fig. 3). In addition to this geometric distinction, there is also a conceptual difference between the sources of gravitational waves across these regimes. Individual astrophysical sources, such as binary mergers or supernovae, are typically deterministic, producing coherent signals with non-vanishing mean amplitude, $\langle h_{ij} \rangle \neq 0$. In contrast, cosmological sources, arising from processes in the early Universe such as inflation and phase transitions, tend to generate a stochastic gravitational wave

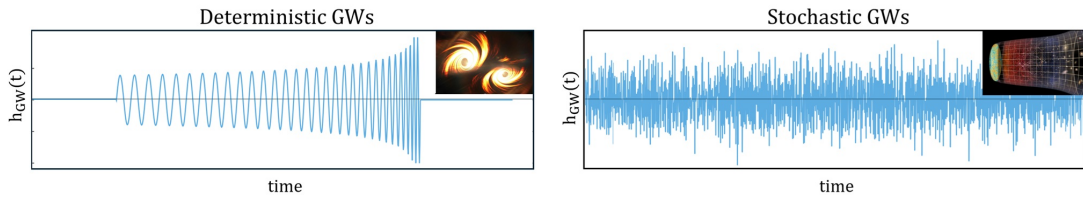


Figure 4: Comparison between deterministic and stochastic classical gravitational waves. Left: A smooth, deterministic waveform from an astrophysical binary merger. Right: A zero-mean Gaussian stochastic background, as expected from cosmological origins.

background (GWB) characterized by vanishing mean but nonzero two-point correlations, $\langle h_{ij}h_{ij} \rangle \neq 0$ (see Fig. 4). This distinction underlines why the statistical treatment of gravitational waves becomes crucial in cosmological contexts. This fundamental separation, both geometric and statistical, motivates the structure of this review. It is therefore divided into two parts: the first devoted to gravitational physics in asymptotically flat spacetimes, and the second to that in expanding cosmological geometries.

All figures presented in this work are original creations of the author, except where explicit attribution or citation is provided.

This review is structured as follows. Sec. 2 develops the framework of linearized general relativity, deriving GWs as solutions to the linearized Einstein equations and examining their physical meaning and properties. Sec. 3 deepens the discussion with a more rigorous treatment, tracing how gravitational radiation are linked to the Weyl tensor’s algebraic structure. This naturally leads to the Bondi–Sachs formalism, which clarifies the physical nature of GWs as real carriers of energy and angular momentum. Sec. 4 examines GWs in an expanding Universe, following their evolution across different cosmological epochs and their generation during inflation. We then explore Weinberg’s adiabatic modes and Maldacena’s consistency relations, which shed light on the infrared structure and the universal behavior of long-wavelength perturbations. We wrap up the section by deriving the inflationary spectrum of vacuum gravitational waves and discussing how they contribute to the integrated Sachs–Wolfe effect. In Sec. 5 we survey the principal observational techniques used to detect gravitational waves, including CMB polarization measurements, pulsar timing arrays, ground- and space-based laser interferometry, and photon-regeneration cavities as gravitational wave detectors. Sec. 6 is devoted to the physical mechanisms that generate gravitational radiation, beginning with astrophysical sources and followed by cosmological sources. Finally, in Sec. 7 we summarize and outline possible future directions.

Notation and Conventions: Throughout this review we set $c = 1$ while keeping G explicit, and we work within four-dimensional General Relativity unless stated otherwise.

Quantity	Definition / Convention
Reduced Planck mass	$M_{\text{Pl}}^2 \equiv (8\pi G)^{-1}$
Metric signature	$\eta_{\mu\nu} = \text{diag}(-, +, +, +)$

Quantity	Definition / Convention
Spacetime indices	Greek letters $\mu, \nu, \rho, \sigma = 0, \dots, 3$
Spatial indices	Latin letters $i, j, k = 1, 2, 3$
Partial derivative	$\partial_\mu \equiv \partial/\partial x^\mu$
Lie derivative	$\mathcal{L}_\xi X^\mu{}_\nu = \xi^\rho \nabla_\rho X^\mu{}_\nu - (\nabla_\rho \xi^\mu) X^\rho{}_\nu + (\nabla_\nu \xi^\rho) X^\mu{}_\rho$
Riemann tensor	$R^\rho{}_{\sigma\mu\nu} = \partial_\mu \Gamma^\rho_{\nu\sigma} - \partial_\nu \Gamma^\rho_{\mu\sigma} + \Gamma^\rho_{\mu\lambda} \Gamma^\lambda_{\nu\sigma} - \Gamma^\rho_{\nu\lambda} \Gamma^\lambda_{\mu\sigma}$
Ricci tensor	$R_{\mu\nu} = R^\rho{}_{\mu\rho\nu}$
Ricci scalar	$R = g^{\mu\nu} R_{\mu\nu}$
Gravitational waves in TT gauge	γ_{ij}
Cosmic scale factor	$a(t)$
Hubble parameter	$H \equiv \dot{a}/a$
Cosmic time	t
Bondi time	$u \quad (u = t - r)$
Conformal time	$\tau \quad (d\tau \equiv dt/a(t))$

Throughout the text, shaded boxes are used to introduce definitions essential for understanding the material in the current or subsequent sections. Finally, we will frequently use the following acronyms.

BBN	Big Bang Nucleosynthesis	LSS	Large-Scale Structure
BH	Black Hole	PND	Principal Null Directions
BMS	Bondi–Misner–Sachs group	PTA	Pulsar Timing Array
BSM	Beyond the Standard Model	GWB	Gravitational Wave Background
CMB	Cosmic Microwave Background	SLS	Surface of Last Scattering
GR	General Relativity	SM	Standard Model
GW	Gravitational Wave	SNR	Signal-to-Noise Ratio
HFGW	High-Frequency Gravitational Waves	TT	Transverse-Traceless gauge

2 Linearized General Relativity and GWs

Shortly after formulating the theory of general relativity, Albert Einstein linearized his field equations and discovered that the theory admits wave-like solutions [1], small perturbations of the Minkowski space-time, that propagate at the speed of light. These solutions, known today as gravitational waves, appear in the weak-field approximation, where the space-time metric is only slightly perturbed from flat space. Although this linearized approach may initially appear as a mere simplification, it has proven to be remarkably powerful in both theoretical and observational contexts within astrophysics and cosmology. It enables the

analysis of gravitational radiation from compact astrophysical sources such as binary black holes and neutron stars, and forms the theoretical foundation for modern gravitational wave detectors. We begin this section by considering the weak-field limit of general relativity and deriving the general solution to the linearized Einstein equations. We next investigate the properties of gravitational waves generated by localized sources, and analyze their polarization states and observable effects on freely falling test particles.

2.1 The Weak-Field Approximation and Wave Solutions

A weak gravitational field corresponds to a region of spacetime that is only mildly curved. In such regions, there exist coordinate systems in which the spacetime metric can be expressed as

$$g_{\mu\nu} = \eta_{\mu\nu} + \tilde{h}_{\mu\nu}, \quad (2.1)$$

where $\eta_{\mu\nu}$ is the Minkowski metric

$$\eta_{\mu\nu} = \text{diag}(-1, 1, 1, 1), \quad (2.2)$$

and $\tilde{h}_{\mu\nu}$ represents a small perturbation such that both it and its partial derivatives remain small

$$\tilde{h}_{\mu\nu} \ll 1 \quad \text{and} \quad \partial_\lambda^n \tilde{h}_{\mu\nu} \ll 1 \quad (\text{for all } n > 1). \quad (2.3)$$

This intuitive characterization will be given a mathematically rigorous formulation in Sec. 3. The formulation Eq. (2.3) sets the stage for linearizing Einstein's equations

$$R_{\mu\nu} - \frac{1}{2}Rg_{\mu\nu} = 8\pi GT_{\mu\nu}, \quad (2.4)$$

and studying the dynamics of gravitational waves as perturbations propagating in flat spacetime. Note that we can well consider small perturbations about some other background metric, such that $g_{\mu\nu} = \bar{g}_{\mu\nu} + \tilde{h}_{\mu\nu}$. In particular, later in Sec. 4, we will use a similar weak field approach for cosmological perturbations around the FLRW metric.

In the weak-field general relativity, we expand the field equations in powers of $\tilde{h}_{\mu\nu}$ and keep the linear terms. In fact, from the Einstein equation in Eq. (2.4), we find the linearized gravitational field equation as

$$\partial_\alpha \partial^\alpha \tilde{h}_{\mu\nu} + \partial_\mu \partial_\nu \tilde{h} - \partial_\nu \partial_\lambda \tilde{h}_\mu^\lambda - \partial_\mu \partial_\lambda \tilde{h}_\nu^\lambda - \eta_{\mu\nu} (\partial_\alpha \partial^\alpha \tilde{h} - \partial_\sigma \partial_\lambda \tilde{h}^{\lambda\sigma}) = -16\pi GT_{\mu\nu}, \quad (2.5)$$

where \tilde{h} is the trace of the field, $\tilde{h} = \tilde{h}_\mu^\mu$. Although linearized, the equation above does not yet resemble a wave equation. However, it can be significantly simplified through an appropriate field redefinition

$$h_{\mu\nu} \equiv \tilde{h}_{\mu\nu} - \frac{1}{2}\eta_{\mu\nu}\tilde{h}, \quad (2.6)$$

which is the trace-reverse cousin of $\tilde{h}_{\mu\nu}$, *i.e.* $h = -\tilde{h}$. The metric perturbation $h_{\mu\nu}$ possesses a gauge freedom that originates from the diffeomorphism invariance of general relativity.

Under an infinitesimal coordinate transformation

$$x^\mu \rightarrow x^\mu + \xi^\mu(x), \quad (2.7)$$

where ξ^μ is a smooth vector field, the background metric $\eta_{\mu\nu}$ changes according to the Lie derivative along ξ^μ , $\mathcal{L}_\xi \eta_{\mu\nu}$. Consequently, the perturbation transforms as

$$h_{\mu\nu} \rightarrow h_{\mu\nu} + \mathcal{L}_\xi \eta_{\mu\nu} = h_{\mu\nu} + \nabla_\mu \xi_\nu + \nabla_\nu \xi_\mu. \quad (2.8)$$

This transformation expresses the gauge freedom: the physical content of $h_{\mu\nu}$ remains unchanged under such a shift. To fix this gauge ambiguity, it is conventional to impose the Lorenz gauge condition

$$\partial^\mu h_{\mu\nu} = 0 \quad (\text{Lorenz gauge}). \quad (2.9)$$

In this gauge, the linearized Einstein field equations take the particularly simple and covariant form

$$\square h_{\mu\nu} = -16\pi G T_{\mu\nu}, \quad (2.10)$$

where $\square = \partial^\alpha \partial_\alpha$ is the d'Alembertian operator in flat spacetime.

We now turn to the vacuum case of the linearized Einstein field equations, obtained by setting $T_{\mu\nu} = 0$ in Eq. (2.10). This equation admits plane wave solutions of the form

$$h_{\mu\nu}(x) = e_{\mu\nu}(k) e^{ik \cdot x}, \quad (2.11)$$

where $e_{\mu\nu}(k)$ is a constant, symmetric tensor representing the amplitude and polarization of the wave, and k_μ is the wave 4-vector. Substituting into the wave equation shows that the wave vector must satisfy the null condition $k^\mu k_\mu = 0$, which confirms that gravitational waves propagate at the speed of light.

In the presence of matter or energy, the stress-energy tensor $T_{\mu\nu}$ acts as a source for the gravitational field, and the linearized Einstein equation becomes inhomogeneous. To solve it, we employ the Green's function method for the wave operator

$$\square G(x^\mu - y^\mu) = \delta^{(4)}(x^\mu - y^\mu), \quad (2.12)$$

where $G(x^\mu - y^\mu)$ is the Green's function of the flat-space d'Alembertian. The physically relevant solution is the retarded Green's function, which ensures causal propagation and takes the form

$$G(x^\mu - y^\mu) = \frac{1}{4\pi|\mathbf{x} - \mathbf{y}|} \delta(x^0 - y^0 - |\mathbf{x} - \mathbf{y}|), \quad \text{for } x^0 > y^0. \quad (2.13)$$

Using this, the solution to the sourced linearized gravitational field equations is given by

$$h_{\mu\nu}(\mathbf{x}, t) = -4G \int d^3y \frac{T_{\mu\nu}(\mathbf{y}, t - |\mathbf{x} - \mathbf{y}|)}{|\mathbf{x} - \mathbf{y}|}. \quad (2.14)$$

This expression reveals that the gravitational field at the spacetime point (t, \mathbf{x}) is determined entirely by the values of the source $T_{\mu\nu}$ along the past light cone of that point. In other words, gravitational effects propagate causally at the speed of light, just as expected for massless fields (see Fig. 5).

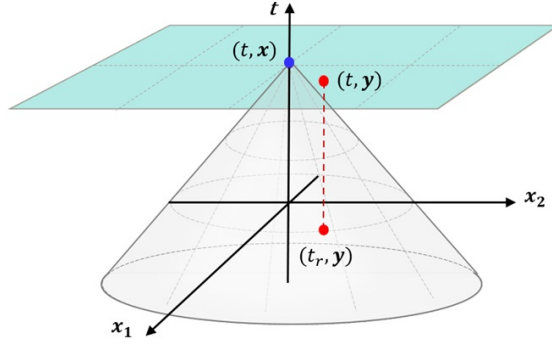


Figure 5: The variation of the gravitational field at a spacetime point (t, \mathbf{x}) arises from the cumulative influence of the source energy–momentum tensor $T_{\mu\nu}$ evaluated at points (t_r, \mathbf{y}) lying on its past light cone, where the retarded time is given by $t_r = t - |\mathbf{x} - \mathbf{y}|$.

2.1.1 Gravitational Radiation of Compact Objects

In many astrophysical scenarios, the gravitational source is spatially compact compared to the distance from the source to the observation point. In such cases, one can expand the integrand of the Green’s function solution (2.14) in a Taylor series about the field point, retaining only the leading-order contribution

$$\frac{1}{|\mathbf{x} - \mathbf{y}|} = \frac{1}{r} + \frac{y^i x_i}{r^3} + y^i y^j \left(\frac{3x_i x_j - r^2 \delta_{ij}}{r^5} \right) + \dots, \quad (2.15)$$

where $r = |\mathbf{x}|$ is the distance from the origin to the observation point. This is the multipole expansion of the Newtonian potential. Applying this expansion to the linearized solution (2.14) and keeping only the leading term yields the far-field approximation

$$h_{\mu\nu}(\mathbf{x}, t) = -\frac{4G}{r} \int d^3y T_{\mu\nu}(\mathbf{y}, t - r) + \mathcal{O}(r^{-2}), \quad (2.16)$$

which describes radiation that decays as $1/r$, a characteristic feature of outgoing spherical waves. Each component of the integral above has a direct physical interpretation:

- $\int T^{00} d^3y = Mc^2$ represents the total energy (mass) of the source,
- $\int T^{0i} d^3y = P^i c$ represents the total momentum of the source along the x^i direction,
- $\int T^{ij} d^3y = \Pi^{ij}$ represents the spatially integrated internal stresses of the source, encompassing pressure and shear.

For an isolated system, conservation of the energy-momentum tensor implies $\nabla_\mu T^{\mu\nu} = 0$. From this, it follows that M and P^i are constants of motion in the linear theory. Moreover, for compact sources, the total momentum P^i can be expressed as

$$P^i = \frac{\partial}{\partial y^0} \left[\int T^{00}(y^0, \mathbf{y}) y^i d^3y \right] \Big|_{y^0=t-r}. \quad (2.17)$$

The total four-momentum $P^\mu = (E, P^i)$ transforms as a Lorentz vector under changes of inertial frame. By performing a Lorentz boost with velocity $\mathbf{v} = \mathbf{P}/E$, we arrive in the center-of-momentum frame where

$$P^i = 0 \quad (\text{center-of-momentum frame}). \quad (2.18)$$

While the stress-energy tensor $T^{\mu\nu}(x)$ transforms covariantly under coordinate changes, one cannot, in general, find a global inertial frame in which $T^{0i}(x) = 0$ at all points, only the integrated momentum P^i can be set to zero by a suitable choice of frame.

In the center-of-momentum frame, the gravitational field reveals its most transparent form

$$h_{00} = -\frac{4GM}{r}, \quad (2.19)$$

$$h_{0i} = 0, \quad (2.20)$$

$$h_{ij} = -\frac{4G}{r} \int T_{ij}(t-r, \mathbf{y}) d^3y. \quad (2.21)$$

We can simplify these expressions for compact sources. Using integration by parts and assuming that the stress-energy tensor vanishes outside the source, we write¹

$$\int T^{ij} d^3y = -\frac{1}{2} \int [\partial_k(T^{ik})y^j + \partial_k(T^{jk})y^i] d^3y. \quad (2.22)$$

Now, applying energy-momentum conservation, $\partial_\mu T^{\mu\nu} = 0$, we obtain

$$\int \partial_k(T^{ik})y^j d^3y = -\frac{d}{dy^0} \left[\int T^{i0}(y^0, \mathbf{y})y^j d^3y \right]. \quad (2.23)$$

Using conservation again and integrating by parts, we find

$$\int (T^{i0}y^j + T^{j0}y^i) d^3y = \frac{d}{dy^0} \left[\int T^{00}(y^0, \mathbf{y})y^i y^j d^3y \right]. \quad (2.24)$$

This motivates introducing the (mass) quadrupole moment tensor of the source

$$I_{ij}(y^0) = \int T_{00}(y^0, \mathbf{y}) y^i y^j d^3y. \quad (2.25)$$

Thus, in the far-field limit, the spatial components of the metric perturbation become

$$h_{ij}(t, \mathbf{x}) = -\frac{2G}{r} \ddot{I}_{ij}(y^0), \quad (2.26)$$

where dot denotes derivative with respect to $y^0 = t-r$. It is often convenient to decompose this expression into its trace and traceless parts

$$h_{ij}(t, \mathbf{x}) = h(t, r) \delta_{ij} + \gamma_{ij}(t, \mathbf{x}), \quad (2.27)$$

¹Since the integration is performed outside the support of $T^{\mu\nu}$, total derivative terms such as $\int \partial_k(T^{ik}y^j) d^3y$ vanish.

where the traceless component is given by

$$\gamma_{ij}(t, \mathbf{x}) = -\frac{2G}{r} \ddot{Q}_{ij}(y^0), \quad (2.28)$$

and Q_{ij} is the reduced quadrupole moment

$$Q_{ij}(y^0) = I_{ij}(y^0) - \frac{1}{3} \delta_{ij} I_k^k(y^0). \quad (2.29)$$

The perturbation γ_{ij} is both transverse and traceless.

Up to now, we found that γ_{ij} is a symmetric, transverse-traceless (TT) tensor. These conditions ensure that gravitational waves are purely spatial, propagate perpendicular to their direction of travel, and carry no longitudinal or scalar modes. This defines the so-called TT gauge, characterized by the conditions

$$h_{0i}^{\text{TT}} = 0 \quad \text{and} \quad h^{\text{TT}} = 0, \quad (2.30)$$

where $h_{ij}^{\text{TT}} = \gamma_{ij}$. We remain within the Lorenz gauge, which imposes additional constraints in the TT gauge $\partial^0 h_{00}^{\text{TT}} = 0$, and $\partial^i h_{ij}^{\text{TT}} = 0$. For non-stationary (i.e., time-dependent) sources, these conditions imply that h_{00}^{TT} also vanishes. Consequently, the gravitational wave is fully described by the spatial components of a symmetric, transverse, and traceless tensor, leaving exactly two dynamical degrees of freedom. We return to this discussion in Sec. 2.2, where a more rigorous treatment is provided.

Radiation in Electromagnetism vs Gravity

Just as Maxwell's equations predict the existence of electromagnetic waves, the linearized Einstein equations reveal that gravity, too, supports wave-like solutions. However, unlike electromagnetic radiation, which begins at the dipole level, GWs first arise at the quadrupole order, a distinction that may seem counterintuitive at first glance. Let us pause for a moment and explore why. This fundamental difference stems from the nature of the sources and the symmetries of the underlying field equations. In electromagnetism, dipole radiation is ubiquitous because charges, positive and negative, can accelerate independently, even within an isolated system. For a localized charge distribution $\rho(t, \mathbf{y})$, the radiative electric field in the far zone can be expressed in terms of the electric dipole moment $p^i(t) \equiv \int d^3y \rho(t, \mathbf{y}) y^i$ and the radiative electric field takes the form

$$\mathbf{E}^{\text{rad}}(t, \mathbf{x}) = \frac{1}{4\pi\epsilon_0 c^2} \frac{1}{r} \hat{\mathbf{n}} \times \left(\hat{\mathbf{n}} \times \ddot{\mathbf{p}}(t-r) \right), \quad (2.31)$$

where $\hat{\mathbf{n}} = \mathbf{x}/r$ denotes the direction of propagation. Gravity, however, couples to energy-momentum, which is always positive in mass-dominated systems. As a result, momentum conservation guarantees a fixed mass dipole in the center-of-momentum frame as Eq. (2.18), forbidding both monopole and dipole gravitational radiation. To see how this constraint might be circumvented, consider a thought experiment involving a gravitational dipole: a pair of positive and negative masses accelerating apart. Such a system would self-accelerate, violating momentum conservation and

eliminating the possibility of a global center-of-momentum frame. Though unphysical, this setup illustrates how gravitational dipole radiation could, in principle, arise in a theory that allows negative mass.

Feature	EM	Linearized Gravity
Source	j^μ	$T^{\mu\nu}$
Wave equation	$\square A^\mu = j^\mu$	$\square h_{\mu\nu} = -16\pi G T_{\mu\nu}$
Conservation law	$\nabla_\mu j^\mu = 0$	$\nabla_\mu T^{\mu\nu} = 0$
Leading radiative	Dipole	Quadrupole
Monopole	× (charge conservation)	× (energy conservation)
Dipole	✓ (leading order)	× (momentum conservation)
Quadrupole	✓	✓ (leading order)
Radiated field	$E_i^{\text{rad}} \propto \ddot{p}_i$	$h_{ij}^{\text{TT}} \propto \ddot{Q}_{ij}^{\text{TT}}$
Spin of carrier	1 (photon)	2 (graviton)

Table 2: Comparison between electromagnetic and gravitational radiation in the linearized (weak-field) regime.

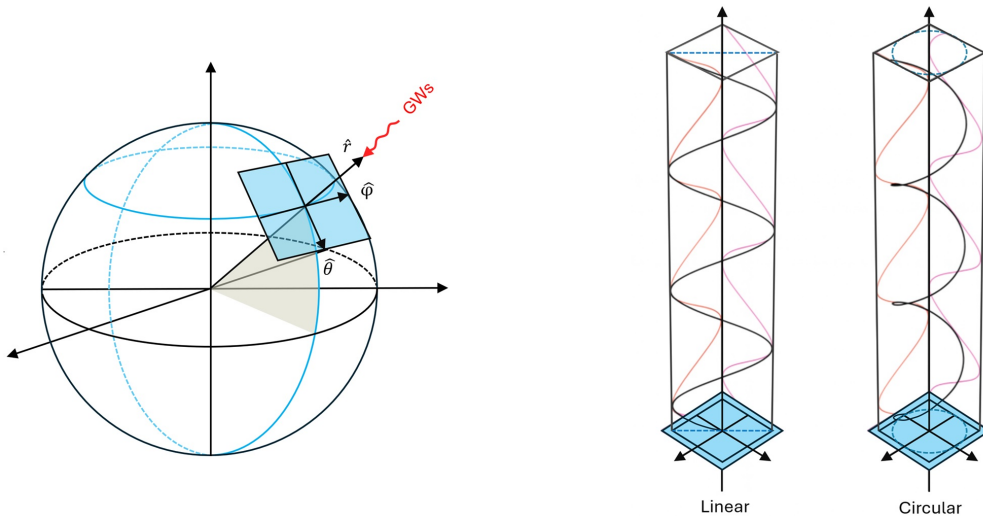


Figure 6: Left panel: the spherical coordinate frame along with its associated unit normal vectors. Right panel: illustrates linearly and circularly polarized waves: in linear polarization, the deformation pattern in the transverse plane oscillates along fixed axes, while in circular polarization, the deformation rotates uniformly within the transverse plane.

2.2 Polarization States of GWs and Free Particles

For a gravitational wave propagating in an arbitrary direction $\mathbf{k} = k\hat{n}$, the wave's spatial polarization tensor in the TT gauge can be extracted using the projection operator

$$e_{ij}^{\text{TT}}(\hat{k}) = \left(P_i^k P_j^l - \frac{1}{2} P^{kl} P_{ij} \right) e_{kl}(k) \quad (\text{polarization tensor}), \quad (2.32)$$

where the spatial projection tensor P_{ij} is defined as $P_{ij} = \delta_{ij} - \hat{n}_i \hat{n}_j$, and serves to project any tensor onto the 2d plane orthogonal to the wave propagation direction \hat{n} . Much like in electromagnetism, the two independent dynamical modes of the gravitational wave can be decomposed into distinct polarization states. Expressing $\hat{n} = -\hat{r}$ in terms of polar and azimuthal angles (θ, ϕ) as $\hat{r} = (\sin\theta \cos\phi, \sin\theta \sin\phi, \cos\theta)$, we define the complex polarization basis vectors

$$e_i^\pm(\hat{n}) = \frac{1}{\sqrt{2}} \left(\hat{\theta}_i \pm i\hat{\phi}_i \right) \quad (\text{polarization vector}), \quad (2.33)$$

where $\hat{\theta}$ and $\hat{\phi}$ are orthonormal unit vectors spanning the transverse plane, aligned respectively with increasing θ and ϕ . Since \hat{r} points opposite to the direction of photon propagation, the helicity (defined as the projection of the spin angular momentum along the direction of motion $h = \mathbf{S} \cdot \hat{n}$) is the negative of the projection along \hat{r} . For this reason, the labels e_i^\pm correspond to photon states of helicity ∓ 1 . These two helicity states correspond to circular polarizations as

$$e_i^\pm(\hat{n}) = e_i^{L,R}(\hat{n}). \quad (2.34)$$

From these, one can construct two equivalent bases for the polarization tensors (see Fig. 6):

- Linear polarization tensors, i.e. the familiar plus and cross modes

$$e_{ij}^+(\hat{n}) = \frac{1}{\sqrt{2}} \left(\hat{\theta}_i \hat{\theta}_j - \hat{\phi}_i \hat{\phi}_j \right), \quad e_{ij}^\times(\hat{n}) = \frac{1}{\sqrt{2}} \left(\hat{\theta}_i \hat{\phi}_j + \hat{\phi}_i \hat{\theta}_j \right), \quad (2.35)$$

- Circular polarization tensors, i.e. the right- and left-handed helicity states

$$e_{ij}^R(\hat{n}) = e_i^R \otimes e_j^R, \quad \text{and} \quad e_{ij}^L(\hat{n}) = e_i^L \otimes e_j^L. \quad (2.36)$$

These two bases are related through the transformation:

$$e_{ij}^{R,L}(\hat{n}) = \frac{1}{\sqrt{2}} \left(e_{ij}^+ \pm i e_{ij}^\times \right), \quad (2.37)$$

showing that circular polarizations are simply complex combinations of the linear ones.

In the special case where the wave propagates along the z -axis, i.e., $\hat{n} = \hat{z}$, the linear polarization tensors simplify to the following non-zero components:

$$e_{11}^+ = -e_{22}^+ = \frac{1}{\sqrt{2}}, \quad e_{12}^\times = e_{21}^\times = \frac{1}{\sqrt{2}}, \quad (2.38)$$

with all other components. For circular polarization, the non-zero components are:

$$e_{11}^{R,L} = -e_{22}^{R,L} = \frac{1}{\sqrt{2}}, \quad e_{12}^{R,L} = e_{21}^{R,L} = \pm \frac{i}{\sqrt{2}}, \quad (2.39)$$

with vanishing longitudinal components.

GW Polarizations in d Dimensions and Extended Frameworks

In d -dimensional General Relativity (GR), a massless spin-2 graviton carries

$$N_{\text{pol}} = \frac{d(d-3)}{2}, \quad (2.40)$$

independent polarization (radiative) degrees of freedom. This immediately implies that GR admits propagating gravitational wave modes only for $d \geq 4$. In particular, for $d = 3$ one obtains $N_{\text{pol}} = 0$, meaning that three-dimensional GR has no local gravitational radiation and no graviton polarization states. In contrast, many modified theories of gravity introduce additional dynamical degrees of freedom, which generically lead to extra gravitational wave polarization modes beyond the two transverse $(+, \times)$ modes of four-dimensional General Relativity (GR). In particular, in four dimensions the metric begins with ten degrees of freedom; fixing the coordinate system removes four, leaving six physical degrees of freedom corresponding to the six possible gravitational wave polarizations. Thus, up to four supplementary modes (two scalar and two vector polarizations) may arise, although a given theory of gravity need not include all of them simultaneously. For a thorough review of how additional degrees of freedom arise and propagate in modified gravity frameworks, see [51]. More general discussions of gravitational wave polarizations in alternative theories can be found in [52, 53].

2.2.1 Geodesic Distortion by Passing GWs

To gain a clearer understanding of the physical manifestation of each GW polarization state, it is instructive to examine their effect on the geodesic deviation between freely falling test particles. Consider two nearby test particles that interact only through gravity, initially at rest and separated by the spacelike vector

$$X^\mu(0) = (0, \xi_0^i). \quad (2.41)$$

The passage of a gravitational wave perturbs their geodesic motion, inducing a nonzero contribution to the geodesic-deviation equation. Recalling that the evolution of the separation four-vector X^μ between neighboring geodesics with tangent four-vector u^μ is governed by

$$\frac{D^2 X^\mu}{D\tau^2} = R^\mu{}_{\nu\lambda\sigma} u^\nu u^\lambda X^\sigma, \quad (2.42)$$

where

$$\frac{D}{D\tau} \equiv u^\mu \nabla_\mu \quad (2.43)$$

is the covariant derivative along the particle's worldline. In the local proper (detector) frame associated with the reference geodesic, the motion is static to zeroth order and receives corrections only at $\mathcal{O}(h_{\mu\nu})$, so that

$$u^\mu = (1, 0, 0, 0) + \mathcal{O}(h_{\mu\nu}). \quad (2.44)$$

Therefore, the geodesic deviation of the nearby particles is

$$\frac{D^2 X^i}{D\tau^2} = -R^i{}_{0j0} X^j. \quad (2.45)$$

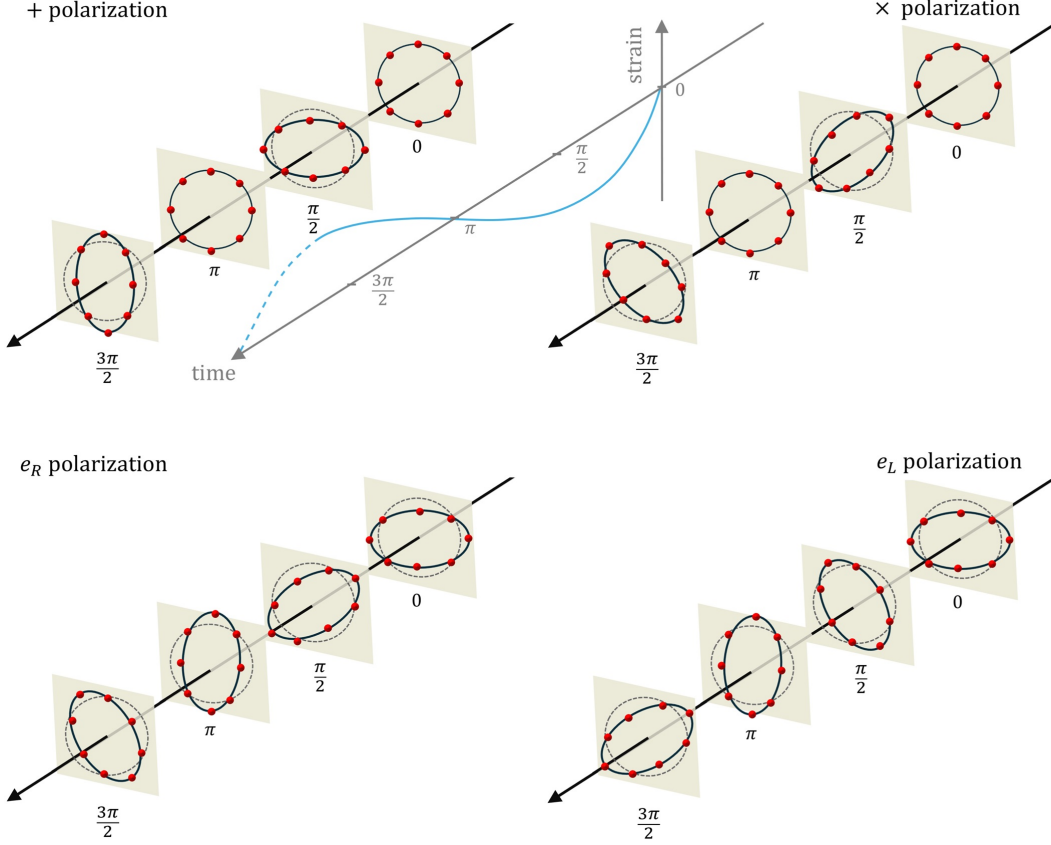


Figure 7: Effect of GW polarization states on a ring of freely falling particles. Solid lines and red dots show particle positions over time; dashed lines mark their unperturbed locations. Top: plus and cross polarizations. Bottom: right- and left-handed circular polarizations. Image credit: Adapted and modified from [54].

In the rest frame of the particle, we have $dx^i = 0$, and the line element reduces to

$$ds^2 = -d\tau^2 = -(1 + h_{00}) dt^2. \quad (2.46)$$

In the TT gauge, $h_{00}^{\text{TT}} = 0$ at leading order, so the coordinate time and the particle's proper time coincide up to second order in the perturbation,

$$\tau = t + \mathcal{O}(h_{ij}^{\text{TT}2}). \quad (2.47)$$

Using this, the geodesic deviation simplifies to

$$\frac{d^2 X^i(t)}{dt^2} = \frac{1}{2} \partial_t^2 h_{ij}^{\text{TT}} \xi_0^j, \quad (2.48)$$

which integrates to the displacement of the separation vector

$$X^i(t) = \xi_0^j (\delta_{ij} + \frac{1}{2} h_{ij}^{TT}(t, \mathbf{x})). \quad (2.49)$$

That shows a passing gravitational wave induces a deformation of the separation vector between freely falling test particles. Fig. 7 illustrates this tidal effect for each of the four possible polarization states of gravitational waves, showing how the ring of freely falling particles is periodically stretched and compressed as the wave propagates through spacetime.

Gravitational Memory Effect²

Before proceeding to the next part, let us pause to discuss a fascinating phenomenon; the remarkable way in which spacetime itself remembers the passage of GWs, leaving behind a permanent trace of the universe’s most violent events. When a burst of gravitational radiation carries a non-oscillatory component, i.e. the waveform exhibits a net offset $\Delta h_{ij}^{TT} \neq 0$, the spacetime curvature leaves a lasting imprint on freely falling test particles. After the wave has passed, the geodesic deviation in Eq. (2.49) no longer returns to zero but retains a permanent displacement,

$$\Delta X^i \simeq \frac{1}{2} \Delta h^{TT i}_j \xi^j(0) \neq 0. \quad (2.50)$$

This enduring change in the relative separation of particles, known as the gravitational memory effect [55–57], reveals that spacetime itself retains memory of the passing gravitational wave. Although one may formally remove this step in the metric by performing a large diffeomorphism, such as a late-time spatial shear,

$$x^i \longrightarrow x^i + \frac{1}{2} \sigma^i_j x^j, \quad \sigma^i_i = 0, \quad \sigma^i_j = -\Delta h^{TT i}_j, \quad (2.51)$$

this transformation is not a mere gauge redundancy. Because it does not vanish at null infinity, it maps the geometry between inequivalent asymptotic vacua [58, 59]. Consequently, the memory effect stands as a genuine observable: a permanent, measurable shift in relative distance or interferometric phase, encoding the asymptotic difference between the early and late gravitational wave configurations. The gravitational wave memory effect, first explored in gravitational physics by Zel’dovich & Polnarev [55], was later developed in depth by many others [56, 57]. Observational prospects for detecting the memory effect have been proposed using ground-based interferometers such as LIGO [60], space-based detectors including LISA [61], as well as through observations with Pulsar Timing Array experiments [62]. We will return to this connection when we examine the infrared structure of asymptotically flat spacetimes in Sec. 3.4.2, and again in the context of cosmology and Weinberg’s adiabatic modes in Sec. 4.3.

3 Theoretical Aspects of Gravitational Waves

In the previous section, we employed the weak-field approximation to derive gravitational waves. This approach dates back to Einstein himself, who was the first to identify gravitational waves as solutions within the linearized GR theory. Yet, due to the conceptual and mathematical ambiguities of the time, he later questioned their physical reality within the full nonlinear theory. This uncertainty slowed progress for decades, until the pioneering works of Bondi, Pirani, Robinson, and Trautman finally resolved it, showing, through a fully consistent physical and mathematical treatment of asymptotically flat spacetimes, that gravitational waves are real, radiative solutions that carry energy and angular momentum. In this section, we will first discuss the theoretical issues and ambiguities of linearized gravity. Next, we will examine the algebraic structure of the Weyl tensor and its geometric interpretation as the carrier of tidal forces. Finally, we will conclude by exploring how spacetime geometry can radiate, leading to a precise definition of GWs.

3.1 Theoretical Issues of Linear Gravity

Einstein's field equations are intrinsically nonlinear

$$G_{\mu\nu}[g] = R_{\mu\nu} - \frac{1}{2}g_{\mu\nu}R = 8\pi G T_{\mu\nu}. \quad (3.1)$$

The Einstein tensor $G_{\mu\nu}[g]$ is a nonlinear functional of the metric $g_{\mu\nu}$ and its derivatives. Hence, spacetime curvature couples to itself through the very structure of the equations. Let us now take a more rigorous look at the weak-field approximation introduced in Sec. 2. We consider small perturbations $h_{\mu\nu}$ around flat spacetime

$$g_{\mu\nu} = \eta_{\mu\nu} + h_{\mu\nu}, \quad |h_{\mu\nu}| \ll 1. \quad (3.2)$$

Expanding the Einstein tensor in powers of $h_{\mu\nu}$ gives

$$G_{\mu\nu}[g] = G_{\mu\nu}^{(1)}[h] + G_{\mu\nu}^{(2)}[h] + \mathcal{O}(h^3), \quad (3.3)$$

where $G_{\mu\nu}^{(1)}$ is linear and $G_{\mu\nu}^{(2)}$ is quadratic in $h_{\mu\nu}$. Substituting this into Einstein's equations yields

$$G_{\mu\nu}^{(1)}[h] = 8\pi G T_{\mu\nu} - G_{\mu\nu}^{(2)}[h] + \mathcal{O}(h^3). \quad (3.4)$$

The quadratic term $G_{\mu\nu}^{(2)}$ acts as an additional source, and one may define the effective stress-energy tensor of the gravitational field as

$$t_{\mu\nu}^{(\text{grav})} = -\frac{1}{8\pi G} G_{\mu\nu}^{(2)}[h]. \quad (3.5)$$

The field equations can then be written in the form

$$G_{\mu\nu}^{(1)}[h] = 8\pi G \left(T_{\mu\nu} + t_{\mu\nu}^{(\text{grav})} \right). \quad (3.6)$$

This relation makes manifest that the gravitational perturbation itself contributes to the total source of curvature, encapsulating the idea that gravity gravitates. Owing to its

universal coupling to all forms of energy, including its own, the gravitational field renders general relativity inherently nonlinear. A further subtlety concerns the condition $|h_{\mu\nu}| \ll 1$ (and similarly for its derivatives). The metric, however, is not a directly observable quantity; its components depend on the chosen coordinates. By an appropriate coordinate transformation, the same physical spacetime can appear with metric components that are either large or small. Thus, the weak-field limit must be defined in terms of coordinate-invariant physical quantities.

These considerations lead to several key conceptual questions:

- i) Do the full, nonlinear Einstein equations admit propagating solutions that can meaningfully be interpreted as gravitational waves?
- ii) In the weak-field limit, do these solutions reduce to the familiar linearized waves?
- iii) How can one consistently define gravitational energy and momentum in a generally covariant theory where energy cannot be localized?
- iv) Given that the metric is not itself an observable, how should one formulate a physically meaningful and coordinate-invariant definition of the weak-field limit?

For decades, the physical reality of gravitational waves remained clouded due to the above conceptual ambiguities. A decisive turning point came with F. Pirani's insightful analysis [63], which linked the Weyl tensor to measurable tidal effects and inspired a new understanding of radiation in general relativity. Building on these ideas, H. Bondi in 1957 introduced the first mathematically precise definition of gravitational waves [2]. His pioneering work, together with subsequent contributions by I. Robinson and A. Trautman, established that the full, nonlinear Einstein equations admit genuine radiative solutions that carry energy and angular momentum to infinity. In what follows, we briefly review these seminal developments.

3.2 The Weyl Tensor: Geometry of Tidal Forces

Even before Bondi's seminal Nature paper in 1957 [2], Felix Pirani made a brilliant early attempt to define gravitational waves in purely geometric terms [63]. His insight was to analyze the algebraic structure of the Weyl tensor through the Petrov classification as a means to identify radiative regions of spacetime. In doing so, Pirani proposed that the physicality of gravitational waves should be anchored not in coordinate-dependent metrics, but in the measurable tidal effects encoded in the curvature tensor, i.e. in the relative acceleration of nearby geodesics governed by the Weyl tensor in vacuum. This idea elegantly shifted the focus from perturbative metrics to intrinsic geometry, offering a criterion that applies even in exact solutions. The approach is well motivated: far from the source, the Ricci tensor vanishes, and the full Riemann tensor reduces to its traceless part which is the Weyl tensor (see Fig. 8). In what follows, we briefly outline Pirani's idea and the resulting geometric characterization of radiative spacetimes.

In 4d, the Riemann curvature tensor possesses 20 independent components. Of these, 10 correspond to the Ricci tensor, while the remaining 10 are captured by the traceless

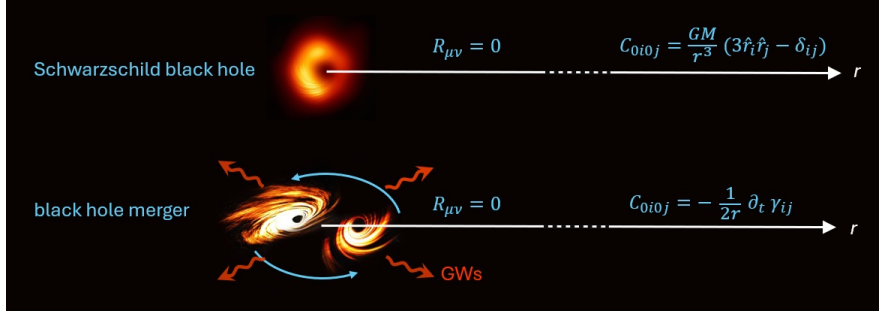


Figure 8: The Weyl tensor encodes the free gravitational field, tidal shear and distortion, independent of matter. To highlight the behavior of the Weyl tensor in different regimes, we consider two illustrative examples: the Schwarzschild solution, which is non-radiative and exhibits a leading-order Weyl tensor decay of $\mathcal{O}(1/r^3)$, and a radiative binary black hole merger, where the leading-order Weyl tensor component falls off as $\mathcal{O}(1/r)$ in the far-field (null infinity) limit.

Weyl tensor, which encodes the conformal structure of spacetime.

$$C_{\mu\nu\lambda\sigma} = R_{\mu\nu\lambda\sigma} - (g_{\mu[\lambda}R_{\sigma]\nu} - g_{\nu[\lambda}R_{\sigma]\mu}) + \frac{1}{3}R g_{\mu[\lambda}g_{\sigma]\nu}. \quad (3.7)$$

More precisely, it is unchanged under a conformal transformation of the metric

$$g_{\mu\nu} \mapsto g'_{\mu\nu} = \Omega^2 g_{\mu\nu}, \quad (3.8)$$

$$C_{\mu\nu\lambda}{}^\sigma \mapsto C'_{\mu\nu\lambda}{}^\sigma = C_{\mu\nu\lambda}{}^\sigma. \quad (3.9)$$

Note that $C'_{\mu\nu\lambda\sigma} = \Omega^2 C_{\mu\nu\lambda\sigma}$. More intuitively, the Weyl tensor expresses the tidal forces that a free-falling body feels along a geodesic. However, unlike the Ricci tensor, it does not have information about the change of the volume, but only how the shape of the body is distorted by the tidal forces.

In four dimensions, the Weyl tensor can be viewed as a linear operator acting on the six-dimensional space of antisymmetric rank-two tensors (bivectors),

$$(C \cdot B)_{\mu\nu} = \frac{1}{2} C_{\mu\nu}{}^{\alpha\beta} B_{\alpha\beta}, \quad B_{\mu\nu} = -B_{\nu\mu}. \quad (3.10)$$

A bivector represents an oriented two-plane in the tangent space and can be expressed as

$$B_{\alpha\beta} = v_{[\alpha} w_{\beta]} = v_\alpha w_\beta - v_\beta w_\alpha. \quad (3.11)$$

Formally, one considers Eq. (3.10) and seeks its eigenbivectors and corresponding eigenvalues,

$$\frac{1}{2} C^{\mu\nu}{}_{\alpha\beta} X_{\mu\nu} = \lambda X_{\alpha\beta}. \quad (3.12)$$

Among them, we are interested in eigenbivectors, constructed from null vectors play a privileged role: they are invariant under rescaling of l^μ and encode the geometry of lightlike directions. At any given point in spacetime, the Weyl tensor can possess at most four

linearly independent eigenbivectors, each corresponding to a null direction in the underlying geometry known as the principal null directions (PNDs). Physically, their importance stems from the fact that the causal structure of a Lorentzian geometry is determined entirely by its null cones: null vectors specify the propagation of signals, gravitational radiation, and the horizons of black-hole spacetimes. In particular, by examining how the Weyl tensor maps null bivectors into themselves, one probes directly how the free gravitational field influences the focusing, twisting, and shearing of null congruences.

We now show how a single null direction l^μ can be completed into a full null tetrad. First choose a second null vector n^μ such that $l_\mu n^\mu = -1$. The 2-dimensional subspace orthogonal to both k^μ and n^μ , is spacelike and admits an orthonormal basis $\{e_1^\mu, e_2^\mu\}$. From these one constructs two complex null vectors

$$m^\mu = \frac{1}{\sqrt{2}}(e_1^\mu + i e_2^\mu), \quad \bar{m}^\mu = \frac{1}{\sqrt{2}}(e_1^\mu - i e_2^\mu), \quad (3.13)$$

satisfying $m^\mu m_\mu = \bar{m}^\mu \bar{m}_\mu = 0$, $m^\mu \bar{m}_\mu = 1$, and $l_\mu m^\mu = n_\mu m^\mu = 0$. The four null vectors $\{l^\mu, n^\mu, m^\mu, \bar{m}^\mu\}$ form a null tetrad.³ Once the tetrad is constructed, we can introduce bivectors built from l^μ as

$$X_{\mu\nu} = l_{[\mu} m_{\nu]}, \quad (3.14)$$

and its square satisfies $X_{\mu\nu} X^{\mu\nu} = 0$. Similarly, its complex conjugate

$$\bar{X}_{\mu\nu} = l_{[\mu} \bar{m}_{\nu]}, \quad (3.15)$$

is also a simple null bivector.

The principal null directions and their degeneracies give rise to the Petrov classification, thereby linking the algebraic structure of curvature to the causal geometry of spacetime. Originally introduced by A. Petrov in 1954 [65] and later reinterpreted by F. Pirani [63], the Petrov classification characterizes the possible algebraic symmetries of the Weyl tensor at each spacetime point. Now you may ask why do these special null directions matter physically? The answer lies in how the curvature acts on the relative motion of neighboring geodesics—particularly null geodesics that represent bundles of light rays or gravitational waves. Consider a smooth one-parameter family of null geodesics $x^\mu(\lambda, s)$, where λ is an affine parameter along each geodesic and s labels the distinct geodesics in the congruence. The tangent vector is obtained by differentiating with respect to λ at fixed s , while the geodesic-deviation vector arises from differentiating with respect to s at fixed λ , i.e.

$$l^\mu \equiv \left. \frac{\partial x^\mu}{\partial \lambda} \right|_s, \quad \xi^\mu \equiv \left. \frac{\partial x^\mu}{\partial s} \right|_\lambda. \quad (3.16)$$

These vectors satisfy the commutation relation

$$[l, \xi]^\mu = l^\nu \nabla_\nu \xi^\mu - \xi^\nu \nabla_\nu l^\mu = 0, \quad (3.17)$$

³The null tetrad formalism is the central geometric structure of the Newman–Penrose approach [64] and underlies its spin-coefficient representation of curvature and gravitational radiation.

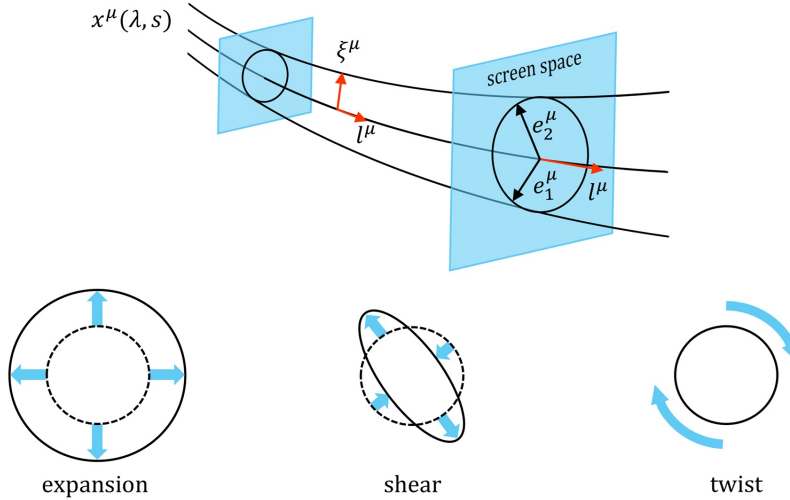


Figure 9: A congruence of null geodesics $x^\mu(\lambda, s)$ labelled by the affine parameter λ and the transverse parameter s . The tangent vector along each geodesic is l^μ . The separation between neighbouring geodesics is described by the geodesic-deviation vector ξ^μ . The screen space is the two-dimensional subspace orthogonal to both l^μ and the auxiliary null vector n^μ , which at each fixed value of λ is spanned by an orthonormal basis $\{e_1^\mu, e_2^\mu\}$. Within this screen the cross-section of the light bundle is defined, along with the expansion, shear, and twist.

which holds for any smooth congruence. The screen space (or optical plane) is the 2-dimensional subspace orthogonal to both l^μ and n^μ . It is spanned by a pair of orthonormal vectors $\{e_1^\mu, e_2^\mu\}$, which serve as a basis for projecting tensors and defining the transverse degrees of freedom. The screen projector onto this 2D subspace is defined by

$$h_{\mu\nu} = g_{\mu\nu} + l_\mu n_\nu + n_\mu l_\nu, \quad (3.18)$$

which projects any vector onto the space orthogonal to both l^μ and n^μ (see Fig. 9). Next we define the optical tensor as the doubly projected derivative

$$\Theta_{\mu\nu} \equiv h_\mu^\alpha h_\nu^\beta \nabla_\beta l_\alpha. \quad (3.19)$$

This is the object that decomposes into

$$\Theta_{\mu\nu} = \frac{1}{2}\theta h_{\mu\nu} + \sigma_{\mu\nu} + \omega_{\mu\nu}, \quad (3.20)$$

giving expansion, shear, and twist of the null congruence as ⁴

$$\theta \equiv h^{\mu\nu} \nabla_\nu l_\mu, \quad \sigma_{\mu\nu} \equiv B_{(\mu\nu)} - \frac{1}{2}\theta h_{\mu\nu}, \quad \omega_{\mu\nu} \equiv B_{[\mu\nu]}. \quad (3.21)$$

⁴Frobenius' theorem states that a vector field v^μ is hypersurface orthogonal iff it satisfies the integrability condition $v_{[\mu} \nabla_\nu v_{\rho]} = 0$. Consequently, hypersurface-orthogonal geodesic congruences possess vanishing vorticity, $\omega_{\mu\nu} = 0$ [66].

In vacuum, the Riemann tensor reduces to the Weyl tensor, so the relative acceleration between two nearby null geodesics is governed by

$$\frac{D^2 \xi^\mu}{d\lambda^2} = -C^\mu{}_{\nu\rho\sigma} l^\nu \xi^\rho l^\sigma. \quad (3.22)$$

The right-hand side encodes how spacetime curvature focuses, shears, or twists the light bundle. When projected onto the two-dimensional screen space orthogonal to l^μ (the subspace spanned by the complex null vectors m^μ and \bar{m}^μ), this equation splits into an isotropic focusing (the expansion) and an anisotropic distortion (the shear). If l^μ is a PND with eigenvalue λ , then inserting the eigenbivector relation Eq. (3.12) together with the explicit form of the null bivector Eq. (3.14) yields

$$\frac{D^2 \xi^\mu}{d\lambda^2} = \lambda(\xi.l) l^\mu. \quad (3.23)$$

Geometrically, this shows that along a PND the Weyl curvature produces no transverse tidal distortion: the optical tensor has vanishing shear, so the cross-section of a narrow bundle of null geodesics remains circular to first order. Thus a PND generates a locally shear-free null congruence. If the PND is repeated (double, triple, or quadruple), this shear-free property extends to an entire null congruence whose integral curves form a geodesic, shear-free null vector field throughout the spacetime [67, 68].

Petrov Classification

It organizes the possible algebraic symmetries of the Weyl tensor into precisely six distinct categories, known as the Petrov types presented in Table 3 and summarized in the left panel of Fig. 10.

Petrov Type	Conditions on PNDs	Spacetime
I	4 simple	General vacuum
II	2 simple + 2 coincide	
D	2 pairs coincide	Stationary, asymptotically flat
III	1 simple + 3 coincide	
N	4 coincide	Gravitational radiation
O	Weyl tensor vanishes	Conformally flat

Table 3: Petrov Classification of Spacetime, ordered from the most general to the most symmetric.

Near localized massive sources, the spacetime is typically of Petrov type I, reflecting its most general algebraic structure. As one moves outward, higher-order terms in the Weyl tensor successively peel off, and the spacetime transitions through types II and III, ultimately approaching type N at future null infinity where only the radiative

component of the gravitational field remains. Type D regions are associated with the gravitational fields of isolated massive objects, e.g., stars and black holes, which is entirely characterized by its mass and angular momentum. The two coincided PNDs present radially ingoing and outgoing null congruences near the object. Type O regions are conformally flat places with zero Weyl tensor, e.g., exact Minkowski and FRW. In this case, any gravitational effects must be due to the immediate presence of matter or the field energy of some non-gravitational field. Type N regions are those regions with transverse gravitational radiation. A spacetime region is type N, if and only if there exists a null vector, k_μ , such that

$$C_{\mu\nu\lambda\sigma}k^\sigma = 0. \quad (3.24)$$

The four coinciding PNDs are given by this null vector which is the wave vector of the propagating gravitational wave.

Peeling Theorem

The Petrov type of a spacetime need not be uniform: it may vary from region to region. The right panel of Fig. 10 illustrates how the algebraic type can change along outgoing null directions. This effect is due to the peeling theorem in general relativity [69], which describes the asymptotic behavior of the Weyl tensor as one goes to null infinity. Let γ be a null geodesic from a point p to null infinity, with affine parameter r . The peeling theorem states that, as r approaches infinity

$$C_{abcd} = \frac{C_{abcd}^{(1)}}{r} + \frac{C_{abcd}^{(2)}}{r^2} + \frac{C_{abcd}^{(3)}}{r^3} + \frac{C_{abcd}^{(4)}}{r^4} + \dots, \quad (3.25)$$

where $C_{abcd}^{(1)}$ is type N, $C_{abcd}^{(2)}$ is type III, $C_{abcd}^{(3)}$ is type II and $C_{abcd}^{(4)}$ is type I [66]. To summarize, the Weyl tensor of a radiative spacetime must be of type N very far from the sources, i.e. in the asymptotic future.

3.3 When Geometry Radiates: Defining Gravitational Waves

Herman Bondi in his Nature paper [2] followed by a subsequent paper by Bondi, Pirani, and Robinson [70], provided the first mathematically precise definition of gravitational waves in the full Einstein equation. Moreover, he proved that gravitational radiation carries energy. In what follows, we review these results in the context of asymptotically flat spacetimes. Throughout this discussion in Secs. 3.3 and 3.4, we work in Bondi retarded coordinates (u, r, z, \bar{z}) , which are well suited for describing radiation propagating toward null infinity. These coordinates are related to the standard spherical coordinates (t, r, θ, ϕ) by

$$u = t - r, \quad z = \cot \frac{\theta}{2} e^{i\phi}, \quad \bar{z} = \cot \frac{\theta}{2} e^{-i\phi}. \quad (3.26)$$

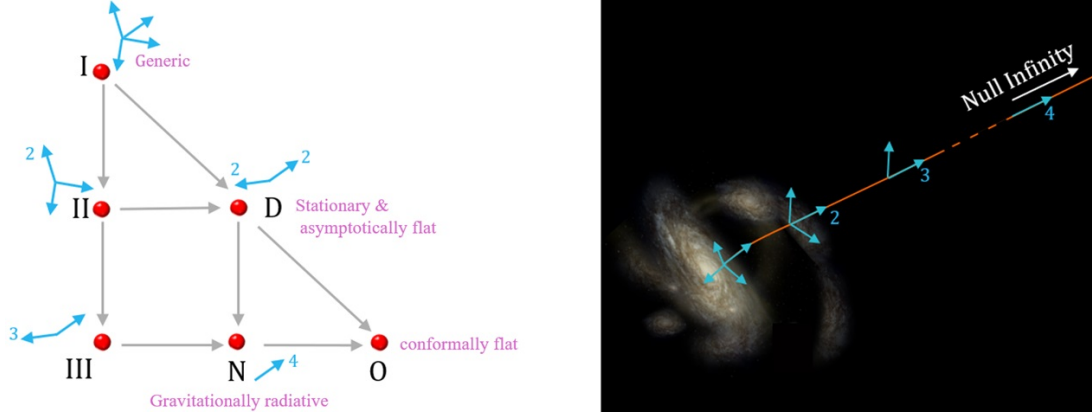


Figure 10: Left panel: The schematic form of the Petrov classification of the Weyl tensor. The blue arrows correspond to each of the principal null directions and the number on arrows represent the number of coinciding PNDs. Right panel: The Petrov type of the gravitational field varies along outgoing null directions: it is type I near localized sources, successively transitions through types II and III, and approaches type N at future null infinity, where only the radiative component remains. The blue arrow indicates the evolution of the Weyl tensor’s Petrov type as one moves toward null infinity in an asymptotically flat spacetime.

The coordinate u denotes the Bondi (retarded) time and labels outgoing null hypersurfaces. For comparison, the advanced time in Minkowski spacetime is given by

$$v = t + r. \quad (3.27)$$

The angular coordinates on the sphere are collectively denoted by $\Theta^A = (z, \bar{z})$ and provide a complex parametrization of the unit two-sphere. In these coordinates, the metric on the sphere takes the form

$$\gamma_{z\bar{z}} = \frac{2}{(1 + z\bar{z})^2}. \quad (3.28)$$

In this coordinate system the Minkowski spacetime metric is

$$ds^2 = -du^2 - 2dudr + 2r^2\eta_{z\bar{z}}dzd\bar{z}. \quad (3.29)$$

Before proceeding further, we need to introduce three essential geometric notions that underlie the analysis of gravitational radiation in general relativity.

- **Asymptotic flatness:** An asymptotically flat spacetime is a Lorentzian manifold in which the curvature vanishes at large distances from some region so that the geometry becomes indistinguishable from Minkowski. Outside the source, the Ricci tensor is zero, and therefore, the asymptotic flatness imposes asymptotic falloff conditions on the Weyl tensor as Eq. (3.25).

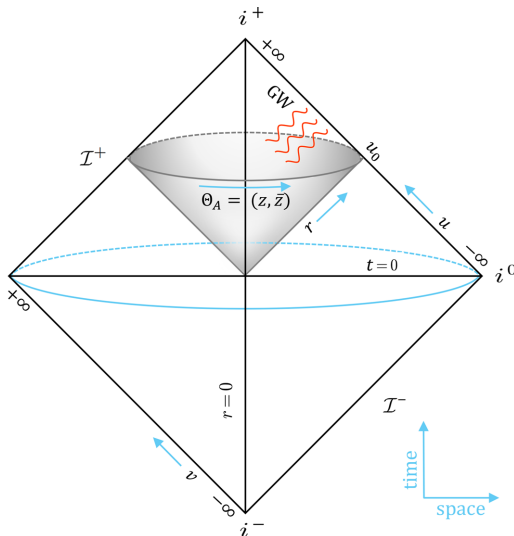


Figure 11: Penrose diagram of an asymptotically flat spacetime. The future and past null infinities, \mathcal{I}^\pm , are parametrized by the retarded and advanced Bondi times u and v . The blue ring, i_0 , denotes spatial infinity. The gray cone in the upper half represent null surface at $u = u_0$. The orange wavy lines indicate outgoing gravitational waves (GWs) propagating toward future null infinity.

- Future null infinity: \mathcal{I}^+ is defined as the endpoints of all future-directed null geodesics along which $r \rightarrow \infty$. This null surface is the product of S^2 with a null line u taking values in \mathbb{R} . Each null hypersurface, σ_{u_0} , intersects \mathcal{I}^+ in a 2-sphere with $u = u_0$. (See Fig. 11)
- The topology of \mathcal{I}^+ , is that of a null hypersurface with the structure $\mathbb{R} \times S^2$, where the \mathbb{R} factor corresponds to the retarded time and the S^2 factor represents angular directions. At each fixed retarded time, the cross-sections of \mathcal{I}^+ are 2-spheres, forming the so-called celestial sphere CS^2 .

Now, we want to study gravitational theories in which the metric is asymptotic, but not exactly equal to, flat metric, and we abbreviate $\Theta^A = (z, \bar{z})$. A natural starting point is to impose the Bondi gauge,

$$g_{rr} = 0, \quad g_{rA} = 0, \quad \partial_r \det\left(\frac{g_{AB}}{r^2}\right) = 0, \quad (3.30)$$

which fixes the four local diffeomorphism degrees of freedom associated with (r, u, Θ^A) . Under these conditions, the most general four-dimensional asymptotically flat metric takes the form

$$ds^2 = -Udu^2 - 2e^{2\beta}dudr + g_{AB} \left(d\Theta^A + \frac{1}{2}U^A du \right) \left(d\Theta^B + \frac{1}{2}U^B du \right). \quad (3.31)$$

where r is the luminosity distance and the metric coefficients appear in the six functions. Here U^A contributes two angular components and g_{AB} , constrained by $\det(g_{AB}/r^2) =$

$\det \eta_{AB}$, carries two independent degrees of freedom. Thus the Bondi gauge fixes four diffeomorphisms and leaves precisely six independent metric functions, the expected number for a general spacetime metric modulo coordinate freedom. Any geometry can be described locally by the metric Eq. (3.31). In Bondi gauge the hypersurface Einstein equation $G_{ur} = 0$ fixes the function β rather than leaving it as free data. Using the determinant condition $\det g_{AB} = \det \eta_{AB}$ and the asymptotic expansion, we have

$$g_{AB} = \eta_{AB} + \frac{\gamma_{AB}}{r} + O(r^{-2}), \quad (3.32)$$

and the constraint equation $G_{ur} = 0$ implies the standard hypersurface relation

$$\partial_r \beta = \frac{r}{16} g^{AC} g^{BD} (\partial_r g_{AB}) (\partial_r g_{CD}), \quad (3.33)$$

as derived in [59, 71, 72] which integrates to

$$\beta(u, r, x^A) = \beta_\infty(u, x^A) - \frac{1}{32} \frac{\gamma_{AB} \gamma^{AB}}{r^2} + O(r^{-3}). \quad (3.34)$$

Asymptotic flatness fixes the integration function $\beta_\infty(u, x^A)$: since $g_{ur} = -1$ as $r \rightarrow \infty$, hence $\beta_\infty = 0$. Thus β is not an independent degree of freedom but is completely determined by the shear γ_{AB} , vanishing at null infinity and beginning at order $1/r^2$. Therefore, in Bondi gauge and after imposing the constraint equation, one degree of freedom is eliminated and we are left with five independent degrees of freedom.

Imposing the asymptotic flatness condition at large r with fixed (u, z, \bar{z}) leads to falloff conditions on the metric components. For the natural choice made by Bondi, van der Burg, Metzner, and Sachs (BMS) [58], the large- r structure of the metric is constrained to be ⁵

$$\begin{aligned} ds^2 = & -du^2 - 2dudr + 2r^2 \eta_{z\bar{z}} dz d\bar{z} \\ & + \frac{2m_B}{r} du^2 + r \gamma_{zz} dz^2 + r \gamma_{\bar{z}\bar{z}} d\bar{z}^2 + D^z \gamma_{zz} dudz + D^{\bar{z}} \gamma_{\bar{z}\bar{z}} dud\bar{z} \\ & + \frac{1}{r} \left(\frac{4}{3} (N_z + u \partial_z m_B) - \frac{1}{4} \partial_z (\gamma_{zz} \gamma^{zz}) \right) dudz + c.c. + \dots, \end{aligned} \quad (3.35)$$

where D_z is the covariant derivative with respect to $\eta_{z\bar{z}}$ while γ_{zz} , m_B and N_z are r independent and functions of (u, z, \bar{z}) . The first three terms in Eq. (3.35) are simply the flat Minkowski metric, and the remaining terms are the leading corrections:

- The first quantity $m_B(u, z, \bar{z})$ is the Bondi mass aspect (for Kerr BH, $m_B = GM$),
- The next one is $N_z(u, z, \bar{z})$, which is the Bondi angular momentum aspect (for a Kerr BH $N_z = 2GmL$),

⁵Compared with the notation adopted in Strominger's book [73], we make a slight adjustment for consistency with the conventions used throughout this review. In particular, what is written as C_{zz} in [73] is denoted here by γ_{zz} for gravitational waves, and their $\gamma_{z\bar{z}}$ is written here as $\eta_{z\bar{z}}$. The conventions of [73] follow those standard in the infrared-gravity and BMS literature, whereas in this work we adopt the notation commonly used in cosmology, expressed in terms of complex spherical-angle coordinates.

- The last term is γ_{zz} which describes the gravitational waves. This quantity is transverse to \mathcal{I}^+ and r^{-1} -suppressed comparing to the dominant orders. The Bondi news tensor is defined as

$$N_{zz} = \partial_u \gamma_{zz}, \quad (3.36)$$

which is the gravitational analogue of the field strength in gauge field theories, i.e. $F_{uz} = \partial_u A_z$.

For later convenience, let us recall a simple but useful identity. On each cut of future null infinity S_u^2 , endowed with the standard measure $d^2z \eta_{z\bar{z}}$, any covariant total derivative on the sphere integrates to zero. Explicitly, for any smooth vector field V^A on S^2 ,

$$\int_{S^2} d^2z \eta_{z\bar{z}} D_A V^A = 0. \quad (3.37)$$

Post-Newtonian Weak-Field, Slow-Rotation Geometry (Lense–Thirring Metric)

To build intuitive insight into the structure of the Bondi metric, it is useful to begin with the line element describing the weak-field, slow-rotation geometry of an isolated gravitating system [74]. In this post-Newtonian regime the metric takes the form

$$ds^2 = -\left(1 - \frac{2GM}{r}\right) dt^2 + \frac{4G}{r^2} (\hat{r} \times \mathbf{J}) \cdot d\vec{r} dt + \left[\left(1 + \frac{2GM}{r}\right) \delta_{ij}\right] dx^i dx^j. \quad (3.38)$$

The above metric contains the the following terms

- M : the total ADM/post-Newtonian mass (monopole),
- \mathbf{J} : the total ADM angular momentum (dipole).

Unlike the Bondi metric introduced in Eq. (3.35), the spacetime above is stationary: neither M nor \mathbf{J} varies in time. In this sense, M represents the static, isotropic limit of the Bondi mass aspect $m_B(u, z, \bar{z})$. The gravitomagnetic interaction responsible for frame dragging

$$g_{0i} = \frac{4G}{r^2} (\hat{r} \times \mathbf{J})_i, \quad (3.39)$$

encodes the characteristic dipolar $1/r^2$ falloff produced by the angular momentum \mathbf{J} . In the Bondi description, the corresponding contribution appears in

$$g_{uz} = \frac{N_z}{r} + \dots, \quad (3.40)$$

where N_z is the Bondi angular-momentum aspect, carrying precisely the dipole moment associated with \mathbf{J} .

3.3.1 GWs Carry Energy

The Bondi mass at a Bondi time, u_1 , is defined as the integral over $S_{u_1}^2$ (the sphere with u_1 at \mathcal{I}^+), as

$$M_B(u_1) = \frac{1}{4\pi G} \int_{S^2} d^2z \eta_{z\bar{z}} m_B(u_1, z, \bar{z}), \quad (3.41)$$

which is positive and time-dependent, such that it is always non-increasing with time. Moreover, in the limit $u \rightarrow -\infty$, S_u^2 asymptotically approaches the spatial infinity, i^0 , and the Bondi mass is equal to the (conserved) ADM mass [75, 76]

$$M_{\text{ADM}} = \lim_{u \rightarrow -\infty} M_B(u). \quad (3.42)$$

The time evolution of m_B is given by the Einstein equation component G_{uu} at \mathcal{I}^+ as

$$\partial_u m_B = \frac{1}{4} [D_z^2 N^{zz} + D_{\bar{z}}^2 N^{\bar{z}\bar{z}}] - \frac{1}{4} N_{zz} N^{zz} - 4\pi G \lim_{r \rightarrow \infty} [r^2 T_{uu}^M], \quad (3.43)$$

where T_{uu}^M is the matter field's energy-momentum tensor. Using the Einstein equation in (3.41) and considering a compact source with $r^2 T_{uu}^M \sim \mathcal{O}(r^{-1})$ at future null infinity, we have

$$M_B(u_2) - M_B(u_1) = -\frac{1}{4} \int_{u_1}^{u_2} du \int d^2z \eta_{z\bar{z}} N_{zz} N^{zz}, \quad (u_2 > u_1), \quad (3.44)$$

in which the $D_z^2 N^{zz}$ terms vanishes under the S^2 integral. This is the famous Bondi mass-loss formula, which measures the amount of mass-loss after some radiation through \mathcal{I}^+ (see the Penrose diagram in Fig. 11). That is zero in case the Bondi news vanishes. Otherwise, the Bondi mass is decreasing with time in the form of gravitational radiation.⁶

3.3.2 GWs Carry Angular Momentum

The Bondi angular momentum associated with the i -th rotation generator $Y_{(i)}^A$ at a Bondi time u_1 is defined by

$$J_i(u_1) = \frac{1}{8\pi G} \int_{S^2} d^2z \eta_{z\bar{z}} Y_{(i)}^A(z, \bar{z}) N_A(u, z, \bar{z}), \quad (3.45)$$

where $Y_{(i)}^A(z, \bar{z})$ denotes the three rotation Killing vectors of the round sphere can be written in the geometric form

$$Y_{(i)}^A(z, \bar{z}) = \varepsilon_{ijk} \hat{r}^j D^A \hat{r}^k, \quad (3.46)$$

where \hat{r}^i is the unit radial vector on S^2 . They generate the $\text{SO}(3)$ isometries of S^2 and each $Y_{(i)}^A$ corresponds to a rotation about one of the three Cartesian axes in \mathbb{R}^3 . The evolution of the angular-momentum aspect is governed by the Bondi constraint equation

$$\begin{aligned} \partial_u N_z &= \frac{1}{4} \partial_z (D_z^2 \gamma^{zz} - D_{\bar{z}}^2 \gamma^{\bar{z}\bar{z}}) - u \partial_u \partial_z m_B + \frac{1}{4} \partial_z (\gamma_{zz} N^{zz}) + \frac{1}{2} \gamma_{zz} D_z N^{zz} \\ &\quad - 8\pi G \lim_{r \rightarrow \infty} [r^2 T_{uz}^M]. \end{aligned} \quad (3.47)$$

⁶The Bondi mass and the mass loss formula were generalized for spacetimes with non-zero cosmological constant in [77].

Integrating the above, similar to the mass aspect, one can find the amount of angular momentum carried by the GWs as

$$\partial_u J_i(u_1) = \frac{1}{16\pi G} \int_{S^2} d^2z \eta_{z\bar{z}} \gamma_{zz}(u, z, \bar{z}) Y_{(i)}^A(z, \bar{z}) D_A N^{zz}(u, z, \bar{z}). \quad (3.48)$$

Integrating this relation over retarded time yields the total change in Bondi angular momentum between two cuts u_1 and u_2 of future null infinity

$$J_i(u_2) - J_i(u_1) = -\frac{1}{16\pi G} \int_{u_1}^{u_2} du \int_{S^2} d^2z \eta_{z\bar{z}} Y_{(i)}^A(z, \bar{z}) \gamma_{zz}(u, z, \bar{z}) D_A N^{zz}(u, z, \bar{z}). \quad (3.49)$$

This quantity is known as the Bondi angular-momentum flux and represents the net angular momentum carried away by GWs through future null infinity during the interval $[u_1, u_2]$. In particular, a nonzero flux implies that the outgoing radiation transports angular momentum from the source to \mathcal{I}^+ , thereby reducing the Bondi angular momentum of the system. Thus gravitational waves, in addition to carrying energy and momentum, also carry angular momentum to null infinity.

Energy–Momentum Tensor and Flux of GWs

To get a better understanding of the results we found above, let us define the effective energy–momentum tensor of gravitational waves and the associated energy and angular-momentum fluxes. In the short-wavelength (Isaacson) approximation, gravitational waves behave like an effective radiative field whose energy–momentum tensor is

$$T_{\mu\nu}^{\text{GW}} = \frac{1}{32\pi G} \bar{\nabla}_\mu \gamma_{\alpha\beta} \bar{\nabla}_\nu \gamma_{\alpha\beta}. \quad (3.50)$$

For an observer with four-velocity u^μ , the energy density of gravitational waves is defined as

$$\rho_{\text{GW}} = T_{\mu\nu}^{\text{GW}} u^\mu u^\nu. \quad (3.51)$$

In nearly flat spacetime, choosing $u^\mu = (1, 0, 0, 0)$ gives the standard expression

$$\rho_{\text{GW}} = \frac{1}{32\pi G} \dot{\gamma}_{ij} \dot{\gamma}_{ij}. \quad (3.52)$$

That is related to the right-hand side of Eq. (3.44). The angular momentum carried by gravitational waves is characterized through the associated flux. For rotations about the i -axis, the angular-momentum flux is

$$\frac{dJ_i}{dt} = -\frac{1}{32\pi G} \epsilon_{ijk} \int d\Omega r^2 \dot{\gamma}_{jl} \dot{\gamma}_{kl}. \quad (3.53)$$

The above flux is related to the right-hand side of Eq. (3.48). These relations encode the essential energetic and dynamical content of gravitational radiation in the wave zone and provide the foundation for computing the energy and angular momentum carried away from compact astrophysical systems by the gravitational field.

3.4 At the Edge of Spacetime: From Poincaré to BMS

In their pioneering analysis of gravitational waves, Bondi, van der Burg, Metzner [58] and Sachs [78] set out to characterize the asymptotic symmetry group of spacetimes approaching Minkowski space at future null infinity \mathcal{I}^+ . Rather than recovering the expected Poincaré symmetry, they uncovered an infinite-dimensional symmetry, the BMS group. This surprising result revealed that the gravitational field possesses a far richer asymptotic structure than previously anticipated, with far-reaching implications for radiation, gravitational memory, and the infrared behavior of gravity [79]. Crucially, this richness is intimately connected to the presence of gravitational waves and their imprints at null infinity—a connection we will return to and explore in more detail below. In what follows, we present a brief summary of this historical development. For a more in-depth exposition, see [73, 80].

3.4.1 Asymptotic symmetries of Gravitational Fields

The asymptotic symmetry group of gravitational fields in asymptotically flat spacetimes is defined as the set of vector fields whose Lie derivatives preserve both the Bondi gauge Eq. (3.30) and asymptotic flatness conditions. More concretely, for a vector field ξ^μ of the form

$$\xi = \xi^u \partial_u + \xi^r \partial_r + \xi^A \partial_A, \quad (3.54)$$

the Bondi gauge and fall-off preserving conditions require the following asymptotic expansions

$$\xi^u = f(z, \bar{z}) + \frac{u}{2} D_A Y^A(z, \bar{z}) + O(r^{-1}), \quad (3.55)$$

$$\xi^A = Y^A(z, \bar{z}) - \frac{1}{r} D^A f(z, \bar{z}) + O(r^{-2}), \quad (3.56)$$

$$\xi^r = -\frac{r}{2} D_A Y^A(z, \bar{z}) + \frac{1}{2} D^2 f(z, \bar{z}) + O(r^{-1}), \quad (3.57)$$

where $f(z, \bar{z})$ is an arbitrary function on CS^2 and the vector field $Y^A(z, \bar{z})$ is a conformal Killing vector on the 2-sphere, obeying

$$D_A Y_B + D_B Y_A = \gamma_{AB} D_C Y^C. \quad (3.58)$$

This equation implies that the Lie derivative of the metric takes the conformal form

$$\mathcal{L}_Y \gamma_{AB} = \Omega \gamma_{AB}, \quad \Omega \equiv D_C Y^C, \quad (3.59)$$

so that the trace gives the conformal factor explicitly. On the round sphere S^2 , Eq. (3.58) admits exactly six independent solutions. This follows from the fact that

$$\text{Conf}(S^2) \cong SL(2, \mathbb{C}), \quad (3.60)$$

whose Lie algebra $\mathfrak{sl}(2, \mathbb{C})$ is isomorphic to $\mathfrak{so}(3, 1)$, the six-dimensional Lorentz algebra consisting of three rotations and three boosts. The three rotational generators appear as

true Killing vectors on the celestial sphere: they preserve the round metric and therefore satisfy

$$\mathcal{L}_Y \gamma_{AB} = 0 \quad (\text{rotations}). \quad (3.61)$$

The remaining three generators correspond to Lorentz boosts. Boosts do not preserve the spatial metric, since they mix time and space, but they induce Möbius transformations on S^2 and therefore are conformal Killing vectors. Hence the six generators of the Lorentz group, forming $\mathfrak{so}(3,1)$, act on the celestial sphere as the six global conformal symmetries of CS^2 .

Having identified the the Lorentz algebra $\mathfrak{so}(3,1)$ on CS^2 , one may naturally ask: where are the translations of 4d Minkowski space? Remarkably, translations from the scalar function $f(z, \bar{z})$ that parametrizes supertranslations. Unlike the Lorentz transformations, which are fixed by the conformal geometry of the sphere, the function $f(z, \bar{z})$ is completely arbitrary. It assigns to each null direction on the celestial sphere an independent shift along the null generators of \mathcal{I}^+ . In this sense, translations correspond to the lowest spherical-harmonic modes of an infinite-dimensional space of functions on S^2 . Since $f(z, \bar{z})$ is an arbitrary function of angle on the celestial sphere, it can be expanded in spherical harmonics,

$$f(z, \bar{z}) = \sum_{\ell=0}^{\infty} \sum_{m=-\ell}^{\ell} f_{\ell m} Y_{\ell m}(z, \bar{z}). \quad (3.62)$$

The ordinary spacetime translations arise from the four lowest modes with $\ell = 0$ and $\ell = 1$. All higher multipoles $\ell \geq 2$ generate genuine supertranslations, which deform the structure of \mathcal{I}^+ in an angle-dependent manner (see Fig. 12). More precisely, a supertranslation is defined by a smooth function $f(\hat{n})$ on the celestial sphere that shifts retarded time according to

$$u \mapsto u + f(\hat{n}), \quad (3.63)$$

linking the geometry of CS^2 to the infinite-dimensional BMS group.

Structure of the BMS₄ Algebra

The four-dimensional BMS algebra is a semidirect product between the Lorentz algebra and the infinite-dimensional abelian algebra of supertranslations. Let T_f denote a supertranslation with parameter $f(\theta, \phi)$ and let Y denote a Lorentz generator. Their commutation relations are

$$[T_f, T_{f'}] = 0, \quad [Y, T_f] = T_{Y.f}, \quad (3.64)$$

showing that Lorentz transformations act nontrivially on the space of supertranslations by mixing the spherical-harmonic components of f . This yields the semidirect product⁷

$$\text{BMS}_4 = SL(2, \mathbb{C}) \ltimes \mathcal{T}, \quad (3.65)$$

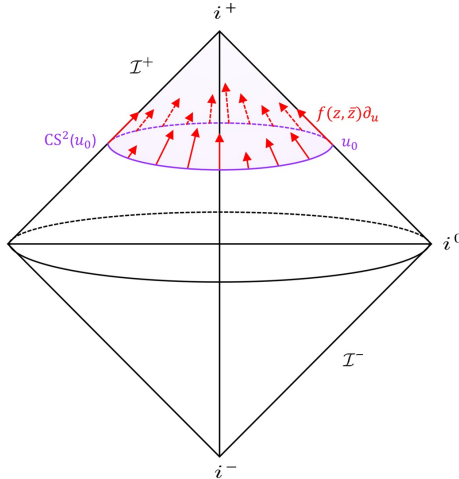


Figure 12: Illustration of the supertranslation action $f(z, \bar{z}) \partial_u$ on the celestial sphere at fixed Bondi time u_0 . Each direction on \mathcal{I}^+ undergoes an angle-dependent shift along the null generators, highlighting the geometric meaning of BMS_4 supertranslations.

where \mathcal{T} is the group of smooth functions on the celestial sphere CS^2 under addition. Thus BMS_4 extends the Poincaré group by an infinite-dimensional set of transformations acting nontrivially under Lorentz rotations and boosts.

3.4.2 Why Radiative Spacetimes Have the Full BMS Group?

Up to now we showed that the asymptotic symmetry group of asymptotically flat spacetimes in Bondi gauge is the BMS group. Yet a natural question remains: why is the asymptotic symmetry structure of gravity so vastly richer than that of Minkowski spacetime? The answer lies in the presence of gravitational radiation. Unlike in flat space, where no dynamical degrees of freedom propagate, an asymptotically flat spacetime can carry gravitational waves, and these waves leave imprints at null infinity that enlarge the space of physically distinguishable configurations. It is precisely this radiative freedom that opens the door to the infinite-dimensional structure of the BMS group.

In exact Minkowski spacetime the asymptotic metric at \mathcal{I}^+ is globally Lorentz invariant, and the Bondi shear vanishes,

$$\gamma_{AB}^{\text{Mink}} = 0. \quad (3.67)$$

⁷Definition (Semidirect product): Let N and H be groups, and let $\rho : H \rightarrow \text{Aut}(N)$ be a homomorphism describing an action of H on N by automorphisms. The semidirect product of N by H , denoted $N \rtimes_{\rho} H$, is defined as the set $N \times H$ equipped with the group law

$$(n_1, h_1)(n_2, h_2) = (n_1 \rho(h_1)(n_2), h_1 h_2). \quad (3.66)$$

With this multiplication, N is a normal subgroup of $N \rtimes_{\rho} H$, while H embeds as a (not necessarily normal) subgroup. The product is semidirect because the group law in N is twisted by the action of H , encoding the nontrivial way in which elements of H act on elements of N .

Under a supertranslation with parameter $f(z, \bar{z})$, the shear transforms as

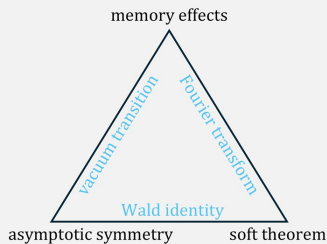
$$\delta_f \gamma_{AB} = -2D_A D_B f + \gamma_{AB} D^2 f. \quad (3.68)$$

Demanding that Minkowski spacetime remain invariant forces this variation to vanish. Using Eq. (3.62), the only solutions are the $\ell = 0, 1$ spherical harmonics—corresponding to the usual time and space translations. Thus the complete invariance group of Minkowski spacetime is precisely the Poincaré group. The picture changes dramatically once gravitational wave is present. If gravitational radiation passes through future null infinity, the shear changes between early and late retarded times. Integrating the news gives the net change

$$\Delta \gamma_{AB} = \gamma_{AB}(u = +\infty) - \gamma_{AB}(u = -\infty) = \int_{-\infty}^{+\infty} N_{AB} du. \quad (3.69)$$

This nonzero shift is the gravitational memory effect: freely falling observers experience a permanent relative displacement even after the wave has passed. What is striking is that the mathematical form of this shift is highly constrained. On the two-sphere at null infinity, any symmetric tracefree tensor constructed from a scalar function $f(z, \bar{z})$ takes the form shown in Eq. (3.68). Thus, if the memory-induced shift $\Delta \gamma_{AB}$ matches this expression for some f , then the initial and final vacuum configurations are related by a supertranslation. Radiative processes therefore move the system between inequivalent vacua connected by supertranslations. These transformations cease to act trivially: instead, they map an infinite continuum of physically distinct gravitational vacua into one another. The enlargement of the asymptotic symmetry group from Poincaré to the full BMS group is, in this sense, a direct imprint of gravitational waves—the memory they leave, the resulting infinite vacuum degeneracy, and the refined geometric structure of spacetime at future null infinity \mathcal{I}^+ .

Infrared Triangle



Infrared triangle expresses the equivalence between asymptotic symmetries, soft theorems, and memory effects in gauge theory and gravity. The first corner is formed by the infinite-dimensional Bondi–Metzner–Sachs (BMS) asymptotic symmetry group, discovered by Bondi, van der Burg, and Metzner [58], and independently by Sachs [59]. The second corner contains the universal soft theorems, beginning with Weinberg’s 1965 soft photon and graviton theorems [81]. It was later revealed by Strominger that gravitational memory is equivalent to the soft graviton theorem [82]. The third corner comprises the family of gravitational wave memory effects, encompassing

both linear and nonlinear memory, as originally described by Zel’dovich and Polnarev [55], Christodoulou [57], and further developed in [56, 83]. Strominger & Zhiboedov showed in [84] that gravitational memory corresponds to a transition between BMS vacua and that the Fourier transform of the memory formula yields Weinberg’s soft theorem. The structure was later explicitly named the infrared triangle in [73].

Analogous IR effects also arise in QED, where an infrared triangle relates large gauge symmetries, soft photon theorems, and electromagnetic memory effects. Large gauge transformations at null infinity give rise to conserved charges whose Ward identities reproduce the universal soft photon theorem [79, 85–88]. These symmetries have a direct physical imprint in the form of a permanent electromagnetic memory effect. For the parity-violating (chiral) electromagnetism memory effect see [89].

4 Expanding Universe and Gravitational Waves

In Secs. 2 and 3, we explored gravitational radiation in Minkowski and asymptotically flat spacetimes. In this part, we shift our attention to the generation and evolution of gravitational waves in a cosmological background. The gravitational dynamics can be accurately described by asymptotically flat geometries only on scales smaller than about 100 Mpc, where the expansion of the Universe is negligible. On larger, cosmological scales, the expansion becomes dynamically relevant and the spacetime must instead be modeled by the FLRW metric (see Fig. 3). We begin this section with the expansion history of the Universe and the sequence of cosmological eras, then examine gravitational waves produced during inflation and their behavior in (quasi)–de Sitter geometry. Finally, we turn to the infrared structure of inflation, discuss Weinberg’s adiabatic theorem, and conclude with Maldacena’s consistency relation for cosmological correlators.

4.1 Expansion History and Cosmological Eras

Modern cosmology is based on two key observations: i) the universe is expanding, and ii) on large scales (> 100 Mpc) the matter distribution is homogeneous and isotropic. The average spacetime is then described by the Friedmann-Lemaître-Robertson-Walker (FLRW) metric

$$ds_{\text{FLRW}}^2 = -dt^2 + a^2(t)\left(\frac{dr^2}{1 - Kr^2} + r^2 d\Omega^2\right), \quad (4.1)$$

where t is the cosmic time, $a(t)$ is the scale factor, and $K = 0, +1, -1$ describe flat, positively curved and negatively curved spacelike 3-hypersurfaces, respectively. This spacetime is conformally flat, with a vanishing Weyl tensor (Petrov type D). From now on, we restrict our discussion to the case of the flat universe with $K = 0$, which is favored by present

observations.⁸ Now, we define the conformal time τ in terms of the physical time t as

$$d\tau \equiv \frac{1}{a(t)} dt, \quad (4.2)$$

We also define the Hubble parameter, H , which measures the expansion rate of the Universe

$$H \equiv \frac{\dot{a}}{a}. \quad (4.3)$$

Using this relation, we find that the flat FLRW geometry is conformally equivalent to Minkowski spacetime

$$g_{\mu\nu}(\tau, \mathbf{x}) = a^2(\tau) \eta_{\mu\nu}. \quad (4.4)$$

The factor a^2 uniformly rescales the Minkowski geometry, stretching both space and time by the scale factor $a(\tau)$. Light rays (null geodesics) remain unaffected by this conformal rescaling, since for $ds^2 = 0$ the scale factor cancels out. Consequently, the causal structure of the Universe in conformal coordinates is identical to that of flat spacetime, making the conformal time τ a natural variable for describing wave propagation, such as GWs, CMB photons, and cosmological perturbations, in an expanding universe.

Let us now consider a perfect fluid

$$T_{\mu\nu} = (\rho + P) u_\mu u_\nu + P g_{\mu\nu}, \quad (4.5)$$

where ρ is the energy density measured in the rest frame of the fluid, P is the isotropic pressure, and u^μ is the 4-velocity of the fluid (normalized as $u_\mu u^\mu = -1$). For an equation of state

$$P = w\rho, \quad (4.6)$$

the Einstein field equations reduce to the Friedmann equations, i.e.

$$3M_{\text{Pl}}^2 \left(\frac{\dot{a}}{a}\right)^2 = \rho \quad \text{and} \quad M_{\text{Pl}}^2 \frac{\ddot{a}}{a} = -\frac{1}{6}(1+3w)\rho, \quad (4.7)$$

where $M_{\text{Pl}}^2 \equiv (8\pi G)^{-1}$ is the reduced Planck mass. Solving these equations for a constant equation-of-state parameter w , we have

$$a(t) = \left(\frac{t}{t_I}\right)^{\frac{2}{(1+3w)+2}} \quad \text{and} \quad a(\tau) = \left(\frac{\tau}{\tau_I}\right)^{\frac{2}{(1+3w)}}, \quad (4.8)$$

where t_I and τ_I are some positive constants. The behavior of the scale factor during different cosmological eras is summarized in Table 4.

⁸The curvature density parameter, $\Omega_K \equiv -\frac{K}{a^2 H^2}$, quantifying the fractional contribution of spatial curvature to the total energy density. Current observations constrain it to $|\Omega_K| < 0.002$ 98% C.L. [90].

⁹Stiff era is a hypothetical phase between inflation and the radiation era, appearing in models where a scalar field becomes kinetic-energy dominated [91–93]. Although unconfirmed, it is consistent with current bounds if it ends before BBN and is phenomenologically notable for enhancing high-frequency primordial gravitational waves [94].

Cosmological era	Eq. of state	Scale factor	Hubble	SEC
Cosmic inflation	$w = -1 + \frac{2}{3}\epsilon$	$a(t) = \exp(Ht)$ $a(\tau) = -\frac{1}{H\tau}$	$H(t) = H_{\text{inf}}$ $\mathcal{H}(\tau) = -\frac{1}{\tau}$	No
Stiff era ⁹	$w = 1$	$a(t) = \left(\frac{t}{t_S}\right)^{\frac{1}{3}}$ $a(\tau) = \left(\frac{\tau}{\tau_S}\right)^{\frac{1}{2}}$	$H(t) = \frac{1}{3t}$ $\mathcal{H}(\tau) = \frac{1}{2\tau}$	Yes
Radiation era	$w = \frac{1}{3}$	$a(t) = \left(\frac{t}{t_I}\right)^{\frac{1}{2}}$ $a(\tau) = \frac{\tau}{\tau_I}$	$H(t) = \frac{1}{2t}$ $\mathcal{H}(\tau) = \frac{1}{\tau}$	Yes
Matter era	$w = 0$	$a(t) = \left(\frac{t}{t_J}\right)^{\frac{2}{3}}$ $a(\tau) = \left(\frac{\tau}{\tau_J}\right)^2$	$H(t) = \frac{2}{3t}$ $\mathcal{H}(\tau) = \frac{2}{\tau}$	Yes

Table 4: Equation of state, scale factor, and Hubble parameter for each cosmological era. The last column shows validity of the Strong Energy Condition (SEC), i.e., whether $\rho + 3P > 0$. Here, $\mathcal{H} \equiv aH$.

To gain insight into the causal structure of cosmological spacetime, let us consider the propagation of light, characterized by the null condition $ds^2 = 0$. For a radial null geodesic, this condition leads to

$$r(\tau) - r(\tau_I) = \int_{\tau_I}^{\tau} d\tau' = \int_{a_I}^a \frac{d \ln a'}{a' H(a')}, \quad (4.9)$$

where τ is the conformal time. This integral defines the comoving distance that light can travel between τ_I and τ , and hence determines the size of the observable region of the Universe at a given epoch. In terms of the comoving (particle) horizon, $(aH)^{-1}$, we can write

$$(aH)^{-1} = \frac{(1 + 3w)}{2} \tau_I a^{(1+3w)/2}, \quad (4.10)$$

which depends on the scale factor a and the equation-of-state parameter w . The characteristic physical distance scale of the expanding Universe is set by the Hubble radius,

$$R_H = \frac{1}{H}, \quad (4.11)$$

which is the boundary between regions that are causally connected and those that are not. A perturbation mode with comoving wavenumber k has a corresponding physical wavelength $\lambda_{\text{phys}}(t) = \frac{a(t)}{k}$, which grows with the cosmic expansion and can be compared with R_H to determine whether the mode lies inside or outside the Hubble horizon. Modes satisfying $\lambda_{\text{phys}} \leq R_H$ (or equivalently, $k \geq aH$) are said to be sub-horizon and evolve causally, while those with $\lambda_{\text{phys}} > R_H$ (super-horizon) remain effectively frozen until re-entry [95]. Today, the Hubble radius is approximately $R_H^{(0)} \simeq 4.4$ Gpc, corresponding to

the present Hubble parameter $H_0 \simeq 67.7 \text{ km s}^{-1} \text{ Mpc}^{-1}$ [90]. Hence, the largest scales inside the horizon today correspond to

$$k_0 = \frac{H_0}{c} \simeq 2.25 \times 10^{-4} \text{ Mpc}^{-1}, \quad \lambda_0 \simeq 4.4 \text{ Gpc}. \quad (4.12)$$

The observed statistical homogeneity and isotropy of the cosmic microwave background (CMB) across our entire cosmic horizon imply that perturbation modes with wavelengths as large as λ_0 must have been in causal contact, or in thermal equilibrium, at some stage of cosmic evolution.

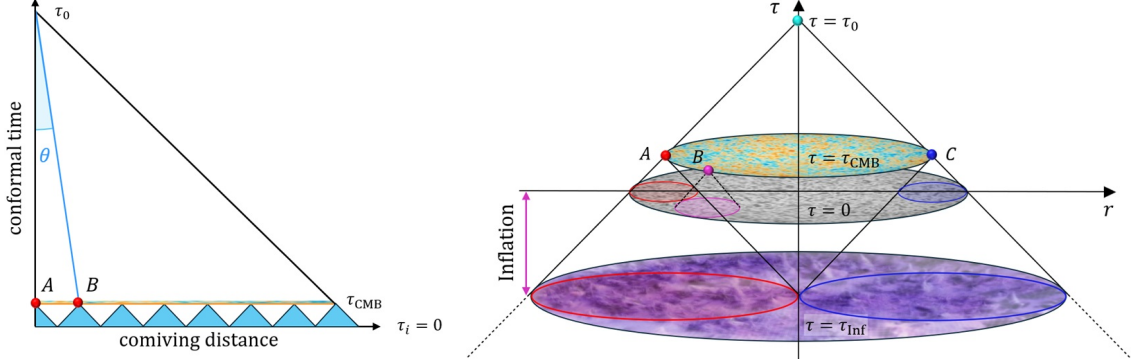


Figure 13: Left panel: The (comoving) causal past of an observer today at τ_0 (redshift $z_0 = 0$), in FLRW spacetime made of ONLY ordinary matter, i.e. $1 + 3w > 0$. The orange line shows the last scattering surface, τ_{CMB} (at redshift $z_{\text{rec}} \simeq 1090$). A and B are two causally disconnected points at the last scattering surface. In fact, the angle spanned by the shaded area at the surface of last scattering is the comoving horizon at recombination. Right panel: The causal past of an observer today, including the epoch of cosmic inflation. Inflation extends conformal time to $\tau_{\text{inf}} < 0$, enlarging the causal domain of the Universe. Consequently, regions that are outside each other's horizons at $\tau = 0$ were in causal contact during inflation, thereby resolving the horizon problem and explaining the observed uniformity of the CMB.

Horizon Problem ¹⁰

Ordinary forms of matter, with positive pressure, satisfy the strong energy condition (SEC), i.e. $\rho + 3P > 0$ ($1 + 3w > 0$). Thus, from Eq. (4.10), the comoving horizon increases as the universe expands. Now, let us compute the angle spanned by the comoving horizon at recombination, θ . As we see in Fig. 13, θ is given as

$$\sin \theta = \frac{2(\tau_{\text{CMB}} - \tau_i)}{\tau_0 - \tau_{\text{CMB}}}. \quad (4.13)$$

On the other hand, we can read the τ integral in Eq. (4.9) as

$$\tau - \tau_I = - \int_{z_1}^{z_2} \frac{dz}{H(z)}, \quad (4.14)$$

where z is the redshift parameter $1+z = \frac{1}{a(z)}$, in which we set the scale factor today to unity, $a_0 = 1$. Moreover, the Hubble parameter is

$$H(z) = \sqrt{\Omega_m(1+z)^3 + \Omega_\gamma(1+z)^4 + \Omega_\Lambda}, \quad (4.15)$$

where $\Omega_m = 0.3$, $\Omega_\gamma = \frac{\Omega_m}{1+z_{eq}}$, and $\Omega_\Lambda = 1 - \Omega_m$ are the matter, radiation, and (late time) dark energy fraction today. Using Eqs. (4.14) and (4.15) in Eq. (4.13) and solving the integral, we find

$$\theta_c \simeq 2.3^\circ. \quad (4.16)$$

At recombination, the causal wavenumber is

$$k_{\text{causal}} \simeq a_* H_* \approx 4 \times 10^{-3} \text{ Mpc}^{-1}, \quad (4.17)$$

corresponding to a comoving wavelength $\lambda_{\text{causal}} \simeq 250 \text{ Mpc}$. Only perturbation modes with $k \gtrsim k_{\text{causal}}$ could have been in causal contact and reached thermal equilibrium by the time of recombination (Fig. 13, left panel). In contrast, the mode corresponding to our present cosmic horizon, with $\lambda_0 \simeq 4.4 \text{ Gpc}$ given by Eq. (4.12), gives

$$\frac{k_{\text{causal}}}{k_0} \simeq 17. \quad (4.18)$$

That implies the region encompassing our observable Universe today would have consisted of roughly $(17)^3 \sim 10^4$ causally disconnected domains at recombination. On the other hand, the observed homogeneity of the CMB implies that even modes as large as λ_0 were once in causal contact, an apparent contradiction known as the horizon problem. As we see in the following, cosmic inflation, an early period of accelerated expansion in which the SEC is violated, solves the horizon problem dynamically and allows our universe to arise from generic initial conditions.

4.1.1 Cosmic Inflation

Our discussion of the horizon problem was based on the validity of the SEC ($1+3w > 0$) and, therefore, the growing Hubble sphere of the standard Big Bang cosmology. A simple solution, therefore, is a phase of decreasing Hubble radius in the early history of the universe,

$$\frac{d(aH)^{-1}}{dt} < 0 \quad \text{where} \quad 1+3w < 0. \quad (4.19)$$

If this lasts long enough the horizon problem can be solved (see the right panel of Fig. 13 and Fig. 14).

¹⁰The covariant form of the strong energy condition (SEC) is $(T_{\mu\nu} - \frac{1}{2}g_{\mu\nu}T) u^\mu u^\nu \geq 0$ for all timelike vectors u^μ .

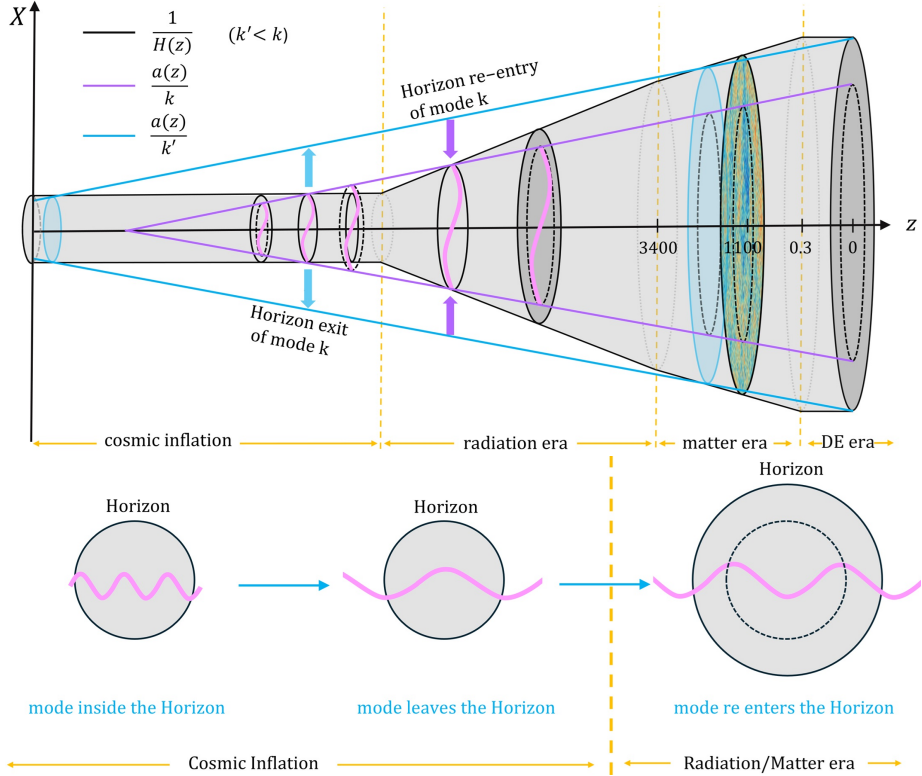


Figure 14: Top panel: The Hubble radius, $\frac{1}{H}$, and the physical wavelength, $\frac{a}{k}$, as functions of the scale factor. Notice that X is the physical coordinate, $X = ax$. The black line shows $1/H$, the red and blue lines denote the physical wavelength of two modes that re-entered the cosmic Horizon during radiation domination (RD) and matter domination (MD) eras, respectively. The shaded gray region shows causally connected points. Bottom panel: close-up view of the horizon relative to the cosmic horizon.

To quantify this idea, let us compute the total amount of expansion that took place between the moment a comoving mode k crossed the Hubble radius during inflation and the end of inflation, a quantity known as the number of e-folds, N_k . It is defined as $N_k \equiv \ln\left(\frac{a_{\text{end}}}{a_k}\right)$, where a_k and a_{end} denote the scale factor at horizon exit of mode k and at the end of inflation, respectively. The required number of e-folds for the present horizon scale $k_0 = 2.25 \times 10^{-4} \text{ Mpc}^{-1}$, this gives

$$N \simeq 61.4 + \frac{1}{2} \ln\left(\frac{H_{\text{inf}}}{10^{14} \text{ GeV}}\right), \quad (4.20)$$

which sets the minimal duration of inflation required to solve the horizon problem and to ensure that our entire observable Universe originated from a single, causally connected patch before inflation began. For typical inflationary energy scales $H_{\text{inf}} \sim 10^{13} - 10^{14} \text{ GeV}$, the Universe must have expanded by roughly 60 e-folds during inflation.

The inflation paradigm postulates a brief period (within $t_{\text{inf}} \approx \frac{N_0}{H_{\text{inf}}}$) of quasi-exponential accelerated expansion during which the scale factor increased by about 60 e-folds [96–99].

This considerable expansion is sourced by a negative pressure component in the energy-momentum of the matter contents and drives the universe towards almost perfect homogeneity, isotropy, and flatness that we have observed. During inflation, the spacetime is very close to a de Sitter space $w \simeq -1$, and the Hubble parameter, H , is almost constant. The scale factor grows exponentially, $a(t) \propto e^{Ht}$, and the deviation from a perfect de Sitter space is quantified in terms of two slow-roll parameters ¹¹

$$\epsilon \equiv -\frac{\dot{H}}{H^2} \quad \text{and} \quad \eta = \frac{\ddot{H}}{2\dot{H}H}, \quad (4.21)$$

which should be small during the slow-roll inflation. This causes the comoving Hubble radius $(aH)^{-1}$ to shrink rapidly, so physical scales that were once much smaller than the Hubble radius ($k = aH$) are stretched to super-horizon sizes. Modes that were initially causally connected (inside the horizon) are driven far apart, and after inflation these same comoving scales re-enter the horizon during the radiation and matter eras (see Fig. 14).

Beyond Cosmic No-Hair Theorem

At cosmological scales, the Universe exhibits an extraordinary degree of homogeneity and isotropy. Since cosmic evolution may begin from generic initial conditions beyond our control, this striking simplicity naturally invites a dynamical explanation—one in which a homogeneous and isotropic state arises as an attractor of the cosmic evolution. The first such attempt was made by Hawking, Gibbons, and Moss in [100, 101] arguing that the late-time behavior of any accelerating Universe is an isotropic Universe. This statement was dubbed as cosmic no-hair conjecture. The first rigorous attempt to establish this conjecture was provided in Wald’s seminal work [75]. Wald’s cosmic no-hair theorem asserts that a broad class of initially expanding Bianchi-type cosmological models (with the exception of Bianchi type IX), whose total energy–momentum tensor consists of a positive cosmological constant supplemented by matter satisfying the strong and dominant energy conditions, evolve exponentially rapidly toward de Sitter spacetime, within only a few Hubble times.

Inflation was originally proposed to explain the observed flatness and large-scale homogeneity of the Universe, offering a dynamical mechanism through which horizon-scale correlations are generated. This motivation led to a reassessment of Wald’s theorem in inflationary contexts, culminating in a generalized cosmic no-hair theorem for inflation presented in [102]. This result demonstrates that, although anisotropies may grow during inflation in the presence of spinning fields, i.e. evading the traditional cosmic no-hair conjecture, their amplitude remains parametrically small and is subject to a universal upper bound. An example of inflationary models with anisotropic hair is the dilaton–Maxwell theory [103]. The authors of [104] extended the discussion of the cosmic no-hair conjecture to include initial anisotropies and demonstrated,

¹¹Besides the definitions introduced in Eq. (4.21), two other slow-roll conventions are widely used in the literature. The potential slow-roll parameters are $\epsilon_V \equiv \frac{M_{\text{Pl}}^2}{2} \left(\frac{V'}{V}\right)^2$ and $\eta_V \equiv M_{\text{Pl}}^2 \frac{V''}{V}$; the Hubble slow-roll parameters are $\epsilon_H \equiv -\frac{\dot{H}}{H^2}$ and $\eta_H \equiv \frac{\dot{\epsilon}_H}{\epsilon_H H}$.

through fully nonlinear numerical simulations, that inflation can emerge from highly inhomogeneous, gradient-dominated initial conditions, provided the inflaton field remains within a sufficiently flat region of its potential. Their analysis, however, is restricted to scalar-field models, and further investigations are required to assess the impact of spinning fields, e.g. gauge fields interacting with the inflaton, on the persistence or decay of cosmic inhomogeneities during inflation.

4.1.2 From the Inflationary Paradigm to Precision Cosmology

The inflationary paradigm was pioneered by Starobinsky (1980) [96], Sato (1981) [97], Guth (1981) [98], and Linde (1982) [99], who independently proposed that a brief period of accelerated expansion in the early Universe could resolve the flatness, horizon, and monopole problems of standard Big Bang cosmology. A profound realization soon followed: if inflation stretches all preexisting irregularities, it must also amplify the inevitable quantum fluctuations of the inflaton field and of spacetime itself. This idea was first developed in pioneering works by Mukhanov and Chibisov [105], Hawking [106], Starobinsky [107], Guth and Pi [108], and Bardeen, Steinhardt and Turner [109]. They formulated the theory of cosmological perturbations in an inflating background and demonstrated that inflation generically produces a nearly scale-invariant, Gaussian, and adiabatic spectrum of curvature perturbations, a strikingly specific and testable prediction. As their wavelengths exceed the Hubble radius, these quantum fluctuations lose their quantum coherence and become effectively classical, but inherently stochastic fields. These perturbations serve as the seeds of the large-scale structure of the Universe, eventually growing under gravity into the cosmic web of galaxies and clusters we observe today. In addition to tensor modes, inflation also predicts a stochastic background of scalar (curvature) perturbations. These fluctuations seed the temperature anisotropies of the cosmic microwave background and eventually grow into the large-scale structure of the Universe. Their statistical properties are described by the scalar power spectrum $\Delta_{\zeta}^2(k)$, which quantifies the variance of curvature perturbations per logarithmic interval in wavenumber. For slow-roll inflation, the scalar power spectrum takes the form

$$\Delta_{\zeta}^2(k) = \frac{1}{8\pi^2\epsilon} \frac{H^2}{M_{\text{Pl}}^2} \left(\frac{k}{aH} \right)^{n_s-1} \Big|_{k=aH}, \quad (4.22)$$

where H is the Hubble parameter during inflation and $n_s = 1 - 4\epsilon + 2\eta$ is the scalar spectral index.

More than a decade later, the inflationary predictions were spectacularly confirmed by the detection of temperature anisotropies in the cosmic microwave background (CMB) by the COBE satellite [110], providing the first direct evidence for primordial perturbations. Subsequent missions refined this picture with ever-increasing precision. The WMAP satellite [111] mapped the CMB sky with degree-scale resolution, measured the spectral index $n_s < 1$, and confirmed the predicted slight red tilt of the primordial spectrum. The PLANCK mission [90] further improved the precision, establishing that the fluctuations are Gaussian and adiabatic to remarkable accuracy. The observations precisely determine the

amplitude of the scalar power spectrum at the pivot scale as

$$\Delta_{\zeta}^2(k_*) \simeq 2.1 \times 10^{-9}, \quad (4.23)$$

providing one of the most important observational anchors for inflationary cosmology. The latest PLANCK results [90] give

$$n_s = 0.9649 \pm 0.0042, \quad (4.24)$$

confirming, with high statistical significance, the deviation from exact scale invariance predicted by slow-roll inflation. This remarkable progression represents one of the central achievements of modern cosmology, establishing a direct link between the primordial fluctuations of the early Universe—most plausibly arising from quantum fluctuations during inflation—and the large-scale structure we observe today. Continued advances from ground-based and suborbital experiments, including ACT (2011–2023) [112], BICEP/KECK (2016–2021) [113], and the BICEP ARRAY [114], have substantially improved sensitivity to the CMB B -mode polarization signal. Upcoming observations from the SIMONS OBSERVATORY, with a first major data release expected around 2026 [115], together with future space missions such as LITEBIRD [22] and the proposed CMB-S4 experiment [23], aim to detect the subtle imprint of primordial gravitational waves—an observation that would provide the next decisive test of inflation. Taken together, these measurements have transformed inflation from a bold theoretical proposal into the leading framework for early-universe cosmology, offering compelling empirical support for the view that the cosmic structures we see today originated from quantum fluctuations stretched to macroscopic scales during an epoch of accelerated expansion.

4.2 Inflation and GWs

A key prediction of the inflationary paradigm is the existence of a stochastic background of primordial gravitational waves (PGWs) generated by tensor fluctuations of the spacetime metric in the very early Universe. Just like the temperature anisotropies of the CMB, this relic GW background forms a random field with no distinct features in either the time or frequency domain. However, GWs carry a crucial advantage over photons: while the CMB decoupled roughly 4×10^5 years after the Big Bang, primordial gravitational waves have been free-streaming since inflation, potentially tracing back to energy scales near the Planck regime (see Fig. 15). For detailed discussions of the thermal history of the Universe, including the evolution from inflation and reheating through Big Bang nucleosynthesis and recombination, see [116–122].

We are interested in the tensor perturbations of the metric that correspond to gravitational waves observed today. At linear order, the perturbed FLRW metric can be written as

$$ds^2 = a^2(\tau) [-d\tau^2 + (\delta_{ij} + \gamma_{ij}(\mathbf{x}, \tau)) dx^i dx^j], \quad (4.25)$$

where the symmetric, traceless, and transverse tensor γ_{ij} represents the two physical polarization states of gravitational waves. The quadratic action for γ_{ij} is

$$S_{\gamma}^{(2)} = \frac{M_{\text{Pl}}^2}{8} \int d\tau d^3x a^2(\tau) [(\gamma'_{ij})^2 - (\partial_{\ell} \gamma_{ij})^2], \quad (4.26)$$

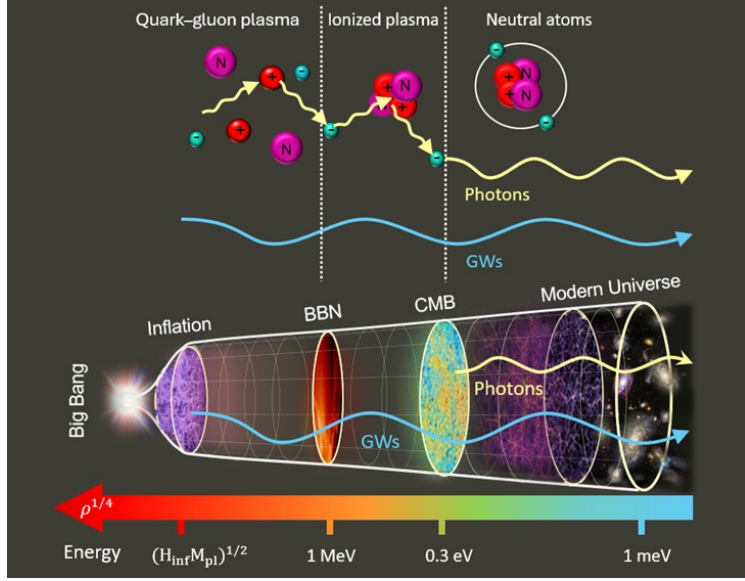


Figure 15: Schematic illustration of the thermal and structural history of the Universe, from cosmic inflation and Big Bang nucleosynthesis (BBN) to the formation of the cosmic microwave background (CMB), the emergence of large-scale structure, and the modern Universe. After inflation ended, the Universe remained for a long period filled with a hot, charged plasma. In this phase, photons were repeatedly scattered by free charged particles and could not propagate freely. Only when protons and electrons combined to form neutral atoms did the Universe become transparent, allowing CMB photons to decouple and free-stream across space, carrying a snapshot of the Universe at that epoch. In contrast, gravitational waves, though universally coupled to all forms of energy, interact so weakly that they were never in thermal equilibrium. The cosmic medium has always been transparent to them, meaning that once detected, these primordial gravitational waves could reveal direct information about the Universe’s highest energy scales and earliest moments, far beyond the reach of any electromagnetic probe. The horizontal axis in this illustration represents the energy scale of the Universe, defined as $\rho^{1/4}$, which decreases as the Universe expands and cools.

where primes denote derivatives with respect to conformal time τ . The evolution of GW modes is governed by the linearized Einstein equations, which in conformal time for the FLRW background reduce to

$$\gamma''_{ij} + 2\frac{a'}{a}\gamma'_{ij} - \partial_i^2 \gamma_\lambda = 16\pi G a^2 \pi_{ij}^T. \quad (4.27)$$

Here π_{ij}^T is the transverse and traceless part of the anisotropic stress tensor.¹² In what

¹²The anisotropic stress tensor can be decomposed as

$$\pi_{ij} \equiv \delta T_{ij} - \frac{1}{3}\delta_{ij}\delta T^k_k = \partial_{ij}^2 \pi^S - \frac{1}{3}\partial^2 \pi^S \delta_{ij} + 2\partial_{(i}\pi_{j)}^V + \pi_{ij}^T, \quad (4.28)$$

with $\partial_i \pi_i^V = \partial_i \pi_{ij}^T = 0$. Here, π^S , π_i^V , and π_{ij}^T denote the scalar, vector, and tensor components, respectively,

follows, we study the evolution of the initial quantum fluctuations of these tensor modes in the expanding background during inflation. Since inflation is dominated by a nearly homogeneous scalar field, any anisotropic stress from matter fields can be neglected, so we set $\pi_{ij}^T = 0$.

The field operator can be expanded in Fourier modes as

$$\gamma_{ij}(\tau, \mathbf{x}) = \sum_{\lambda} \int \frac{d^3k}{(2\pi)^3} \left[\gamma_{\lambda}(\tau, \mathbf{k}) \hat{b}_{\lambda}(\mathbf{k}) e^{i\mathbf{k}\cdot\mathbf{x}} \epsilon_{ij}^{\lambda}(\hat{\mathbf{k}}) + \gamma_{\lambda}^*(\tau, \mathbf{k}) \hat{b}_{\lambda}^{\dagger}(\mathbf{k}) e^{-i\mathbf{k}\cdot\mathbf{x}} \epsilon_{ij}^{\lambda*}(\hat{\mathbf{k}}) \right], \quad (4.29)$$

where $\epsilon_{ij}^{\lambda}(\hat{\mathbf{k}})$ denotes the polarization tensor, and $\hat{b}_{\lambda}(\mathbf{k})$ and $\hat{b}_{\lambda}^{\dagger}(\mathbf{k})$ are the annihilation and creation operators, respectively, satisfying

$$[\hat{b}_{\lambda}(\mathbf{k}), \hat{b}_{\lambda'}^{\dagger}(\mathbf{k}')] = (2\pi)^3 \delta_{\lambda\lambda'} \delta^{(3)}(\mathbf{k} - \mathbf{k}'). \quad (4.30)$$

The tensor perturbations can be treated as a stochastic field, whose statistical properties are captured by the two-point correlation function of the corresponding quantum operators,

$$\langle \hat{\gamma}_{\lambda}(\mathbf{k}) \hat{\gamma}_{\lambda'}^{\dagger}(\mathbf{k}') \rangle = (2\pi)^3 \delta^{(3)}(\mathbf{k} - \mathbf{k}') \delta_{\lambda\lambda'} P_{\gamma}(k), \quad (4.31)$$

where $P_{\gamma}(k)$ denotes the tensor power spectrum. For convenience, one often defines the dimensionless tensor power spectrum as

$$\Delta_T^2(k) \equiv \frac{k^3}{2\pi^2} P_{\gamma}(k), \quad (4.32)$$

which directly characterizes the amplitude of the stochastic gravitational wave background generated during inflation. In the scale-invariant limit, $\Delta_T^2(k)$ becomes nearly constant, reflecting the uniform excitation of tensor modes across different wavelengths.

As is evident from Eq. (4.26), the field γ_{ij} is not yet canonically normalized. To introduce a canonically normalized variable, we define

$$v_{ij} \equiv \frac{aM_{\text{Pl}}}{2} \gamma_{ij}. \quad (4.33)$$

In terms of v_{ij} , the action becomes

$$S^{(2)} = \frac{1}{2} \int d\tau d^3x \left[(v'_{ij})^2 - (\partial_{\ell} v_{ij})^2 + \frac{a''}{a} v_{ij}^2 \right], \quad (4.34)$$

and leads to the field equation

$$v_{\lambda}'' + \left(k^2 - \frac{a''}{a} \right) v_{\lambda} = 0. \quad (4.35)$$

This equation describes the propagation of quantum tensor modes in a time-dependent background, where the term $\frac{a''}{a} \simeq \frac{2+3\epsilon}{\tau^2}$ acts as an effective mass induced by cosmic expansion. Its general solution can be expressed in terms of Hankel functions as

$$v_{\lambda}(\tau, k) = \frac{\sqrt{\pi|\tau|}}{2} e^{i(1+2\nu_T)\pi/4} \left[c_1 H_{\nu_T}^{(1)}(-k\tau) + c_2 H_{\nu_T}^{(2)}(-k\tau) \right], \quad (4.36)$$

with π_{ij}^T capturing the transverse and traceless part of the anisotropic stress [122].

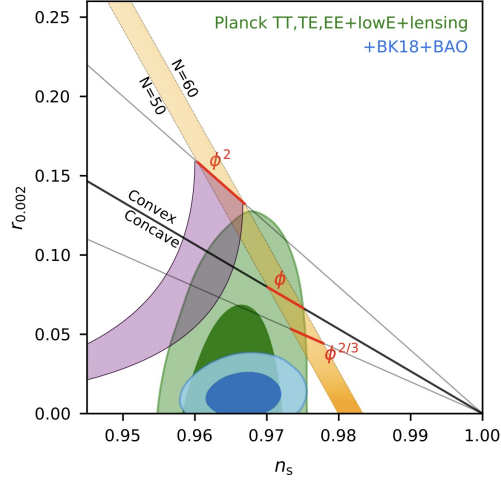


Figure 16: Constraints on the scalar spectral index and the tensor-to-scalar ratio (n_s, r) at $k = 0.002 \text{ Mpc}^{-1}$ from PLANCK, with BK18 & BAO data, compared with predictions of representative inflationary models. Image credit: BICEP/Keck Collaborations [124].

where c_1 and c_2 are constants determined by the choice of initial conditions and ν_T is ¹³

$$\nu_T \simeq \frac{3}{2} + \epsilon. \quad (4.38)$$

Assuming seeds of perturbations to be from the quantum fluctuations, so-called Bunch-Davies vacuum, imposes the initial value in the asymptotic past as

$$\lim_{\tau \rightarrow -\infty} v_\lambda(\tau, \mathbf{k}) = \frac{1}{\sqrt{2k}} e^{-ik\tau}. \quad (4.39)$$

Consequently, the corresponding mode function γ_λ (up to an overall phase) takes the form

$$\gamma_\lambda(\tau, k) = \frac{\sqrt{\pi} |\tau|^3}{2} \frac{H}{M_{\text{Pl}}} H_{\nu_T}^{(1)}(-k\tau). \quad (4.40)$$

Now, let us compute the tensor power spectrum for modes after horizon crossing. During inflation, the quantum fluctuations of the metric are stretched to super-horizon scales ($k \ll aH$), where they effectively freeze and behave as classical perturbations. The amplitude of each mode at horizon exit ($k = aH$) determines the primordial tensor spectrum. The dimensionless tensor power spectrum is given by

$$\Delta_T^2(k) = \frac{2}{\pi^2} \frac{H^2}{M_{\text{Pl}}^2} \left(\frac{k}{aH} \right)^{n_T} \Big|_{k=aH}, \quad (4.41)$$

¹³The asymptotic behavior of the Hankel function is as [123]

$$\lim_{z \rightarrow \infty} H_\nu^{(1)}(z) = \sqrt{\frac{2}{\pi z}} e^{-i(2\nu+1)\pi/4} e^{iz}, \quad \lim_{z \rightarrow 0} H_\nu^{(1)}(z) = -\frac{i}{\pi} \left(\frac{2}{z} \right)^\nu \Gamma[\nu]. \quad (4.37)$$

where H is the Hubble parameter during inflation. Evaluating the spectrum at horizon exit ($k = aH$) ensures that each mode is characterized by the value of H when it left the horizon. The quantity n_T in Eq. (4.41) is the tensor spectral index, defined as

$$n_T \equiv \frac{d \ln \Delta_T^2}{d \ln k} = -2\epsilon. \quad (4.42)$$

A strictly scale-invariant spectrum corresponds to $n_T = 0$, in which case the power Δ_T^2 is independent of the wavenumber k . Inflation predicts a slight red tilt ($n_T < 0$), meaning that longer-wavelength modes have slightly larger amplitudes. The overall amplitude of the tensor spectrum is directly related to the energy scale of inflation, while its nearly scale-invariant shape reflects the quasi-de Sitter nature of the inflationary expansion.

A key observable quantity in inflationary cosmology is the tensor-to-scalar ratio

$$r_* = \frac{\Delta_T^2(k_*)}{\Delta_\zeta^2(k_*)}, \quad (4.43)$$

which measures the relative amplitude of primordial GW perturbations to scalar (curvature) perturbations. For single-field slow-roll (single-clock) inflation, the tensor and scalar amplitudes are directly linked through the slow-roll parameter, $r_* = 16 \epsilon_*$, providing a direct probe of the energy scale and dynamics of inflation. The most recent joint analysis by the PLANCK and BICEP/Keck collaborations places a stringent upper bound on the tensor-to-scalar ratio [124]

$$r_{0.05} < 0.036 \quad (95\% \text{ C.L.}). \quad (4.44)$$

The Energy Scale of Inflation

Combining the upper limit on r with the measured scalar amplitude yields an upper bound on the Hubble scale during inflation,

$$H_{\text{inf}} = \pi M_{\text{Pl}} \sqrt{\frac{r \Delta_\zeta^2(k_*)}{2}} \lesssim 4.7 \times 10^{13} \text{ GeV}, \quad (4.45)$$

corresponding to an inflationary energy scale of $V_*^{1/4} \lesssim 10^{-2} M_{\text{Pl}}$. Thus, even a small value of r may probe physics near the grand-unified scale and provides a direct window into the energy scale of inflation. On the other hand, Big Bang Nucleosynthesis (BBN) requires the Universe to be thermalized before light-element formation, implying a minimum reheating temperature $T_{\text{reh}} \gtrsim 5 \text{ MeV}$. Assuming instantaneous reheating, this sets a lower bound on the inflationary Hubble scale

$$H_{\text{inf}} = \sigma_{\text{reh}} \sqrt{\frac{\pi^2 g_*}{90}} \frac{T_{\text{reh}}^2}{M_{\text{Pl}}} \gtrsim 1.1 \times 10^{-23} \text{ GeV}, \quad (4.46)$$

where g_* is the effective number of relativistic degrees of freedom, which at $T_{\text{reh}} \simeq 5 \text{ MeV}$ takes the value $g_* = 10.75$. The parameter σ_{reh} is a phenomenological factor that encodes the efficiency of the reheating process and equals unity in the case of instantaneous reheating (see Fig. 17).

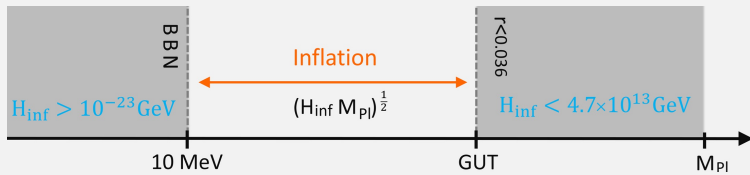


Figure 17: Current allowed window for the inflationary energy scale, $\sqrt{M_{\text{pl}} H_{\text{inf}}}$. The upper bound is determined by the observational limits on the tensor-to-scalar ratio, as given in Eq. (4.45), while the lower bound is set by the requirement that reheating occurs before Big Bang Nucleosynthesis (BBN), as shown in Eq. (4.46). This corresponds to an enormous uncertainty of about 18 orders of magnitude, spanning from the Grand Unified Theory (GUT) scale at 10^{16} GeV down to around 10 MeV.

4.3 IR Structure of Cosmological Perturbations

Here, we briefly review Weinberg’s adiabatic modes theorem and Maldacena’s inflationary consistency relations. The adiabatic mode theorem plays a central role in connecting the primordial perturbations generated in the very early Universe to the cosmological perturbations observed today, providing a bridge between inflationary initial conditions and late-time cosmological observables. Inflationary consistency relation, which fundamentally relies on the presence of these adiabatic modes, encapsulates the symmetry constraints that govern correlations between long-wavelength (soft) and short-wavelength perturbations in single-field inflation.

4.3.1 Adiabatic Modes in Cosmology

To extract information about inflation from observations, we must connect the primordial fluctuations produced during inflation to the structures observed in the later universe (see Fig. 15). This task is complicated by our limited understanding of the post-inflationary epoch—when the energy stored in scalar fields was converted into matter and radiation—and of any subsequent, poorly constrained eras. Although these stages occurred while the relevant fluctuations were stretched far beyond the horizon (see Fig. 14), they may still have affected their amplitude or scale dependence. Therefore, to relate the inflationary perturbations to those observed in the CMB or large-scale structure, we need a conservation law that remains valid on super-horizon scales and is independent of the detailed dynamics of the universe’s evolution. Establishing the existence of such a conserved quantity is precisely the goal of adiabatic mode theorem [95], which demonstrates that certain curvature perturbations remain constant outside the horizon, regardless of the details of the cosmic evolution. The need for a conserved, superhorizon quantity has motivated a long line of foundational work in cosmological perturbation theory. Early seminal studies established the gauge-invariant formulation of cosmological fluctuations and identified the conservation of adiabatic modes on superhorizon scales [125, 126] (see also [127]). Building on these key works, Weinberg demonstrated the full generality of such conservation laws by proving the existence of adiabatic modes under fairly general conditions [95].

We start with the construction of Weinberg's adiabatic modes in the Newtonian gauge which is essential for the derivation of the consistency relations. Fixing the gauge, uniquely specifies all the modes with finite momentum, $k \neq 0$. However, there are residual gauge symmetries for the very long-wavelength modes, which remain a symmetry of the gauge-fixed action. Starting with the flat FLRW metric as the unperturbed metric

$$ds^2 = -dt^2 + a^2 d\mathbf{x}^2. \quad (4.47)$$

Here we focus on the implications of the diffeomorphism invariance on the nature of the very long-wavelength modes with $k/a \ll H$. Therefore, only the homogeneous diffeomorphisms are relevant. The general spatially homogeneous perturbed metric in the Newtonian gauge is

$$ds^2 = -(1 + 2\Phi(t))dt^2 + a^2 \left((1 - 2\Psi(t))\delta_{ij} + \gamma_{ij}(t) \right) dx^i dx^j, \quad (4.48)$$

where Φ and Ψ are the Bardeen potentials and γ_{ij} is the traceless tensor perturbation, gravity wave.¹⁴ One can decompose the general spatially homogeneous perturbed energy-momentum in the Newtonian gauge as

$$T_{00} = -\bar{\rho}g_{00} + \delta\rho \quad \text{and} \quad T_{0i} = -(\bar{\rho} + \bar{P})\partial_i \delta u, \quad (4.49a)$$

$$T_{ij} = \bar{P}(t)g_{ij} + a^2 \left(\delta_{ij}\delta P + \partial_{ij}^2 \pi^S + \pi_{ij}^T \right), \quad (4.49b)$$

where a bar denotes an unperturbed quantity, $\delta\rho$, δP and δu are the perturbed density, pressure and velocity potential respectively. Moreover, π^S and π_{ij}^T are the scalar and tensor anisotropic inertia which characterize departures of $T_{\mu\nu}$ from the perfect fluid form.¹⁵ In the scalar sector, the perturbed energy conservation equation, $\nabla_\mu T^{\mu 0} = 0$, is

$$\delta\dot{\rho} + 3H(\delta\rho + \delta p) - 3(\bar{\rho} + \bar{P})\dot{\Psi} + \nabla^2 \left(\frac{1}{a^2}(\bar{\rho} + \bar{P})\delta u + H\pi^S \right) = 0. \quad (4.50)$$

In terms of the curvature perturbation on uniform-density slices

$$\zeta = -\Psi + \frac{\delta\rho}{3(\rho + p)}. \quad (4.51)$$

and the non-adiabatic pressure perturbation

$$\delta P_{\text{nad}} \equiv \delta P - \frac{\dot{\bar{P}}}{\bar{\rho}} \delta\rho, \quad (4.52)$$

we can write the continuity equation as

$$\dot{\zeta} = -\frac{H}{\bar{\rho} + \bar{P}} \delta P_{\text{nad}} + \frac{k^2}{3} \left(\frac{\delta u}{a^2} + \frac{H\pi^S}{\bar{\rho} + \bar{P}} \right). \quad (4.53)$$

¹⁴Here we neglect the vector perturbations due to their damping nature in most of the inflationary models including our axion-gauge field model.

¹⁵It is interesting to note that in the decomposition (4.49b), the effects of bulk viscosity are included in δp [95].

In the super-horizon limit, $k \ll aH$, the gradient term is suppressed as a^{-2} , and for adiabatic perturbations with $\delta P_{\text{nad}} = 0$, the curvature perturbation is conserved

$$\lim_{\frac{k}{aH} \rightarrow 0} \dot{\zeta} = 0. \quad (4.54)$$

Consequently, the long-wavelength dynamics of ζ admits two independent adiabatic modes:

$$\lim_{\frac{k}{aH} \rightarrow 0} \zeta_1(t) = \text{const}, \quad \lim_{\frac{k}{aH} \rightarrow 0} \zeta_2(t) = 0. \quad (4.55)$$

In the absence of anisotropic stress, $\pi^S = 0$, one has $\Phi = \Psi$, and these two adiabatic modes correspond to the following super-horizon behaviors of the Bardeen potential

$$\lim_{\frac{k}{aH} \rightarrow 0} \Psi_1(t) = \zeta_1 \left[-1 + \frac{H(t)}{a(t)} \int_{t_0}^t a(t') dt' \right], \quad \lim_{\frac{k}{aH} \rightarrow 0} \Psi_2(t) = C \frac{H(t)}{a(t)}, \quad (4.56)$$

where C is an integration constant.

For tensor perturbations, in the regime where the physical wavelength is much larger than the Hubble radius, $k/a \ll H$, we have

$$\ddot{\gamma} + 3H\dot{\gamma} = \mathcal{O}\left(\frac{k^2}{a^2 H^2}\right), \quad (4.57)$$

and the gravitational wave equation admits two independent super-horizon homogeneous solutions

$$\gamma_1(t) = \text{const}, \quad \gamma_2(t) = C \int_{t_0}^t \frac{dt'}{a^3(t')}. \quad (4.58)$$

The second solution decays with time for any expanding universe. Since tensor perturbations satisfy a second-order differential equation, these two modes exhaust the space of possible long-wavelength solutions. Consequently, for generic initial conditions, the tensor perturbations at late times are dominated by the constant mode γ_1 . These are precisely the tensor-sector adiabatic modes guaranteed by Weinberg's adiabatic mode theorem [122]. Note that in the presence of a non-vanishing π_{ij}^T , gravitational waves acquire inhomogeneous solutions sourced by this anisotropic stress, in addition to the adiabatic modes. For explicit examples, see [5, 128–132].

Having completed the derivation of adiabatic modes in cosmology, we now comment on the role of gauge transformations. In our analysis we worked in the Newtonian gauge and solved the Einstein equations in the infrared limit, $\frac{k}{aH} \ll 1$, where Weinberg's theorem guarantees the existence of two adiabatic solutions (a constant mode and a decaying one) for both the scalar perturbations and GWs. However, an important subtlety remains: even after fixing the local gauge completely to Newtonian gauge, there exist residual diffeomorphisms that preserve the Newtonian-gauge form of the metric. These transformations generate solutions that are physically adiabatic modes but arise purely from large coordinate transformations. Thus, adiabatic modes can be understood as originating from these residual large gauge symmetries, rather than from independent dynamical degrees of freedom. Under the action of diffeomorphism transformations

$$x^\mu \mapsto \tilde{x}^\mu = x^\mu + \epsilon^\mu(t, \mathbf{x}), \quad (4.59)$$

there is a ϵ^μ which generates spatially homogeneous transformations on the metric and preserve the Newtonian gauge [122]

$$\epsilon^0(t, \mathbf{x}) = -f(t) - \chi(\mathbf{x}), \quad (4.60a)$$

$$\epsilon^i(t, \mathbf{x}) = (\theta\delta_{ij} + \sigma_{ij})x^j - \partial_i\chi(\mathbf{x}) \int \frac{dt}{a^2(t)}. \quad (4.60b)$$

Here θ is a constant scalar and σ_{ij} is a constant, traceless and symmetric matrix¹⁶, $\text{tr}\sigma_{ij} = 0$. Although infinitesimal locally, these transformations become large as one approaches infinity and are therefore called large gauge transformations. The scalar functions $f(t)$, $\chi(t)$ and θ act only on the scalar perturbations

$$\Phi(t) \mapsto \Phi(t) + \dot{f}(t) \quad \text{and} \quad \Psi(t) \mapsto \Psi(t) + \theta - Hf(t), \quad (4.61)$$

while keep the tensor perturbations untouched. On the other hand, σ_{ij} acts only on the gravitational waves as

$$\gamma_{ij}(t) \mapsto \gamma_{ij}(t) - 2\sigma_{ij}. \quad (4.62)$$

If $\Phi(t)$, $\Psi(t)$, and $\gamma_{ij}(t)$ solve the spatially homogeneous Einstein equations, then any large gauge transformation acting on these quantities produces new, spatially homogeneous solutions as well. In particular, consider a redefinition of the background metric

$$\bar{g}_{\mu\nu}(t) \mapsto \bar{g}_{\mu\nu}(t) + \delta g_{\mu\nu}^A(t), \quad (4.63)$$

where the perturbation is generated by a diffeomorphism. For a scalar-type residual diffeomorphism the induced metric perturbations in Newtonian gauge are

$$\Phi_A(t) = \dot{f}(t), \quad \Psi_A(t) = \theta - Hf(t). \quad (4.64)$$

The corresponding transformations of the background energy–momentum tensor are

$$\delta\rho_A(t) = \dot{\rho}f(t), \quad \delta P_A(t) = \dot{P}f(t), \quad \delta u_A(t) = -f(t), \quad (4.65)$$

with a vanishing scalar anisotropic stress, $\pi_\Lambda^S(t) = 0$. This leads to a constant curvature perturbation,

$$\zeta_\Lambda(t) = \theta. \quad (4.66)$$

There is likewise a spatially homogeneous solution in the tensor sector,

$$\gamma_{ij}^A(t) = 2\sigma_{ij}, \quad (4.67)$$

with vanishing tensor anisotropic stress, $\pi_{ij}^{TA}(t) = 0$. At this stage it appears that the adiabatic modes we derived earlier are nothing more than gauge artifacts associated with the $k = 0$ limit.

¹⁶In general, $\epsilon^i(t, \mathbf{x})$ can have a constant term ϵ_0^i as well as a term like $\omega_{ij}x^j$ where $\omega_{ij} = -\omega_{ji}$. Here, however, we ignored them because (due to the spatial translational and rotational symmetry of the background metric) they do not have any effects on the linear perturbed metric.

This raises the question: how does Weinberg’s theorem elevate these seemingly pure-gauge solutions to physically meaningful modes? The essential step is the following. When both the anisotropic stress, $\pi_{ij}(t, \mathbf{k})$, and the non-adiabatic pressure perturbation, δP_{nad} , vanish on super-horizon scales, the spatially homogeneous ($k = 0$) solutions can be continuously extended to solutions with $k \neq 0$. Since modes with nonzero wavenumber possess no residual gauge freedom in Newtonian gauge, these extended solutions represent genuine physical perturbations. This seemingly simple observation has a profound physical consequence. During inflation, many Fourier modes exit the Hubble horizon and re-enter during the radiation or matter eras. Weinberg’s argument shows that once an adiabatic mode lies outside the horizon, it becomes conserved and remains constant, entirely insensitive to whatever complicated microphysics may operate on sub-horizon scales. This remarkable robustness allows us to relate the very early Universe to cosmological observables in the late Universe. Therefore, in the absence of super-horizon entropy and anisotropic-stress perturbations, inflation predicts that the primordial fluctuations are adiabatic. Note that these scalar modes satisfy $\delta\rho_\alpha/\dot{\rho}_\alpha$ equally for all individual constituents α of the universe, regardless of whether energy is separately conserved for each component. Perturbations with this property are referred to as adiabatic. Any solutions that do not satisfy this condition are correspondingly called entropic. Present cosmological data agree strikingly well with the adiabatic initial conditions implied by inflation and Weinberg’s theorem. CMB temperature and polarization anisotropies constrain the fractional entropy contribution to the primordial power spectrum,

$$\frac{P_{\text{iso}}(k_*)}{P_{\text{ad}}(k_*) + P_{\text{iso}}(k_*)} \lesssim 0.03, \quad (4.68)$$

with $k_* = 0.05 \text{ Mpc}^{-1}$ [133].

4.3.2 Maldacena’s Consistency Relation & Primordial Non-Gaussianity

Now, we turn to the consistency relations, which are a powerful probe of the early universe physics and hold under very general conditions, i.e., in the presence of a long-wavelength adiabatic mode. Maldacena’s consistency relation is, at its core, a statement about the structure of cosmological n -point functions and the pattern of primordial non-Gaussianity generated during inflation. At the level of linear approximation, vacuum inflationary fluctuations have a Gaussian probability.

Primordial Non-Gaussianity

Primordial non-Gaussianities are most generally characterized by the connected n -point correlation functions of the primordial scalar perturbation φ ,

$$\langle \varphi_{\mathbf{k}_1} \cdots \varphi_{\mathbf{k}_n} \rangle_c = (2\pi)^3 \delta^3 \left(\sum_{i=1}^n \mathbf{k}_i \right) F_n(\mathbf{k}_1, \dots, \mathbf{k}_n), \quad (4.69)$$

where statistical homogeneity enforces momentum conservation and the functions F_n encode deviations from Gaussian statistics. The statistical properties of an isotropic

Gaussian field are completely determined by the 2-point function while any odd N -point functions with $N \geq 3$ are exactly zero, and any even N -point functions with $N \geq 4$ are given in terms of the 2-point functions (called disconnected parts of N -point functions).

The leading contribution to primordial non-Gaussianity arises from the three-point function, or bispectrum. The deviation from Gaussianity can be formulated in terms of the bispectrum as

$$\langle \varphi_{\mathbf{k}_1} \varphi_{\mathbf{k}_2} \varphi_{\mathbf{k}_3} \rangle = (2\pi)^3 \delta^3(\mathbf{k}_1 + \mathbf{k}_2 + \mathbf{k}_3) B_\varphi(k_1, k_2, k_3). \quad (4.70)$$

If the power spectrum is scale invariant, dimensional analysis implies that the bispectrum can be expressed in terms of two independent ratios,

$$B_\varphi(k_1, k_2, k_3) = k_1^{-6} B_\varphi(1, x_2, x_3), \quad (4.71)$$

where $x_2 = k_2/k_1$ and $x_3 = k_3/k_1$. In Fig. 18, we present the possible momentum configurations of the bispectrum. Different inflationary scenarios produce bispectra that peak in different configurations [134]. The seminal work of Komatsu & Spergel [135] established the bispectrum as the standard tool for quantifying primordial non-Gaussianity in the CMB [136].

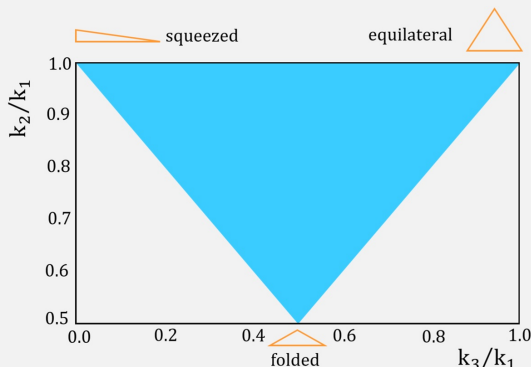


Figure 18: The shaded area shows the possible momentum configurations of the bispectrum. Taking k_1 to be the smallest of the three momenta, the relevant limiting configurations are: (i) the squeezed limit $k_1 \ll k_2 \simeq k_3$, (ii) the equilateral limit $k_1 = k_2 = k_3$, and (iii) the folded (or flattened) limit $k_2 = k_3 = k_1/2$.

While the non-Gaussianity must be computed separately for each specific inflationary model, an important universal result emerges: for all single-clock inflationary scenarios (where there is only one relevant degree of freedom during cosmic inflation), the bispectrum in the squeezed limit satisfies Maldacena’s consistency relation.

Since the tensor modes are the main focus of this work, here we present the consistency relation for the gravitational waves. The scalar consistency relation is the same, and one only needs to replace γ_{ij}^A with the (adiabatic) curvature perturbation ζ_A . The key physical

point behind the consistency relations is the observation that the adiabatic long-wavelength modes, $\delta g_{\mu\nu}^{\text{A}}(t)$, can be removed by large coordinate transformations, i.e.

$$\bar{g}_{\mu\nu}(t) + \delta g_{\mu\nu}^{\text{A}}(t) \mapsto \tilde{g}_{\mu\nu}(\tilde{t}) = \bar{g}_{\mu\nu}(t). \quad (4.72)$$

Hence, adiabatic long-wavelength modes act as a classical background for the short-wavelength modes, which freeze out much later than the long-wavelength modes. In particular, an n -point correlation function of the short modes can be written as

$$\langle \zeta(x_1)\zeta(x_2)\cdots\zeta(x_n) \rangle_{\gamma_{ij}^{\text{A}}(x)} = \langle \zeta(\tilde{x}_1)\zeta(\tilde{x}_2)\cdots\zeta(\tilde{x}_n) \rangle, \quad (4.73)$$

where x^i and \tilde{x}^i are related as

$$\tilde{x}^i = x^i + \frac{1}{2}\gamma_{ij}^{\text{A}}x^j. \quad (4.74)$$

Now, Taylor expanding RHS around x^i , we find the change of the short-distance n -point correlation function as

$$\delta\langle \zeta(\tilde{x}_1)\zeta(\tilde{x}_2)\cdots\zeta(\tilde{x}_n) \rangle = \sum_{\text{I}=1}^n \delta\mathbf{x}_{\text{I}} \cdot \vec{\nabla}_{\text{I}} \langle \zeta(x_1)\zeta(x_2)\cdots\zeta(x_n) \rangle + \cdots. \quad (4.75)$$

As a result, the $(n+1)$ -point correlation function including the long-wavelength mode is given as

$$\langle \gamma_{ij}^{\text{A}}(x)\zeta(x_1)\zeta(x_2)\cdots\zeta(x_n) \rangle \simeq \frac{1}{2} \left\langle \gamma_{ij}^{\text{A}}(x)\gamma_{kl}^{\text{A}}(x) \sum_{\text{I}=1}^n x_{\text{I}}^k \partial_{\text{I}} \langle \zeta(x_1)\zeta(x_2)\cdots\zeta(x_n) \rangle \right\rangle, \quad (4.76)$$

in which we only keep the dominant term that has the relevant contribution. The above equality is the consistency relation in real space. Going to the Fourier space, we arrive at Maldacena's consistency relation

$$\langle \gamma_{\lambda}(\mathbf{q})\zeta_{\mathbf{k}_1}\zeta_{\mathbf{k}_2}\cdots\zeta_{\mathbf{k}_n} \rangle' \simeq -\frac{1}{2}P_{\gamma}^{\text{vac}}(q) \sum_{\text{I}=1}^n \mathbf{e}_{ij}^{\lambda}(\hat{q})k_{\text{I}i}\partial_{k_{\text{I}j}} \langle \zeta_{\mathbf{k}_1}\zeta_{\mathbf{k}_2}\cdots\zeta_{\mathbf{k}_n} \rangle' \quad \text{for } q \rightarrow 0, \quad (4.77)$$

where the prime in $\langle \cdots \rangle$ indicates that we extracted the prefactor $(2\pi)^3\delta^{(3)}(\mathbf{q} + \sum_{\text{I}}^n \mathbf{k}_{\text{I}})$ associated to momentum conservation. Note that the above result follows directly from the fact that adiabatic long-wavelength gravitational waves are equivalent to a change of coordinate for the short-wavelength mode, regardless of the super-horizon behavior of the short modes. Therefore, as far as our inflationary system generates adiabatic tensor perturbations, the above consistency relation holds. It is important to stress that Maldacena's squeezed-limit non-Gaussianity is not a directly observable quantity. As shown rigorously in [137], the primordial squeezed bispectrum predicted by single-field inflation does not imprint an observable modulation of small-scale power in late-time cosmological data. Maldacena's original relation was elevated to a conformal consistency relation in [138] and to an infinite hierarchy of Ward identities in [139].

Cosmological Collider Physics

In inflationary settings, heavy particles can be spontaneously produced by the expansion of the Universe [140–142]. Their interactions with curvature perturbations generate characteristic signatures which encode the masses, spins, and interaction structures of particles. Cosmological collider physics views the inflationary universe as a natural high-energy probe in which massive fields present during inflation imprint characteristic oscillatory and angular structures in primordial non-Gaussianity. Building on early studies of inflationary correlators and quasi-single-field models by Chen & Wang [143, 144], as well as subsequent developments by Noumi, Yamaguchi, & Yokoyama [145], the idea was formulated explicitly by Arkani-Hamed & Maldacena [146]. In this picture, heavy particles act as virtual states, encoding their masses, spins, chemical potential in specific shapes of correlation functions accessible to observation, thereby probing physics far beyond the reach of terrestrial accelerators [147–153], among many others in a rapidly developing literature. Motivated by these theoretical developments, there have been important observational searches for cosmological collider signals in both CMB [154] and Large Scale Structure (LSS) [155]. This program is naturally linked to the cosmological bootstrap, which seeks to determine primordial correlation functions from symmetry, analyticity, and consistency conditions alone [156]. Bootstrap methods classify all allowed inflationary signatures, while the cosmological collider provides their physical interpretation in terms of massive spinning particles in the early universe.

4.4 Inflationary Gravitational Waves at Late Times

The primordial gravitational waves produced during inflation leave observable imprints only after going through the universe’s subsequent expansion history. Following our derivation of the inflationary tensor spectrum and its infrared structure, we now translate these primordial fluctuations into their present-day form. We begin this part by deriving the spectrum of primordial gravitational waves sourced by vacuum fluctuations during inflation. This spectrum spans an enormous range of frequencies—from as low as 10^{-17} Hz, corresponding to wavelengths comparable to the size of the observable Universe, to as high as 10^8 Hz, associated with microscopic scales near the end of inflation and the reheating epoch. We then explore the contribution of gravitational waves to the integrated Sachs–Wolfe effect in the cosmic microwave background.

4.4.1 The Present-Day Spectrum of Gravitational Waves from Inflation

Earlier in Sec. 4.1, we introduced the concept of horizon crossing and re-entry, and outlined the major cosmological epochs. Next we discussed in Sec. 4.2, gravitational waves generated during inflation arise from the amplification of quantum fluctuations in the space-time itself. These tensor perturbations are nearly scale-invariant at horizon exit, with a power spectrum

$$\mathcal{P}_h(k) \simeq \frac{2}{\pi^2} \frac{H_{\text{inf}}^2}{M_{\text{Pl}}^2}, \quad (4.78)$$

where H_{inf} is the Hubble parameter during inflation, and M_{Pl} is the reduced Planck mass. We are now ready to explore how the primordial GWs generated during inflation evolve across these eras, and how they shape the gravitational waves spectrum today. The field equation of vacuum $\gamma_\lambda(\tau, \mathbf{k})$ in the expanding background (regardless of the cosmological era) is

$$\gamma_\lambda''(\tau, \mathbf{k}) + 2\mathcal{H}\gamma_\lambda'(\tau, \mathbf{k}) + k^2\gamma_\lambda(\tau, \mathbf{k}) = 0, \quad (4.79)$$

where again $\lambda = +, \times$, a prime denotes a derivative with respect to the conformal time and $\mathcal{H} = aH$. We can extract analytically some general features of the solution by using the field redefinition

$$h(\tau, \mathbf{k}) \equiv a\gamma_\lambda(\tau, \mathbf{k}). \quad (4.80)$$

In the vacuum case the two polarization states evolve identically and the redefinition above applies uniformly to both polarization modes. The field equation takes the simple form

$$h''(\tau, \mathbf{k}) + (k^2 - \frac{a''}{a})h(\tau, \mathbf{k}) = 0, \quad (4.81)$$

where $'$ means derivative with respect to the conformal time and the effective mass term $\frac{a''}{a} = \frac{1}{2}(aH)^2(1 - 3w)$ is

$$\frac{a''}{a} = \begin{cases} 2\mathcal{H}^2(1 - \epsilon) \simeq \frac{2}{\tau^2}(1 - \epsilon) & \text{inflation} \\ 0 & \text{radiation-era} \\ \frac{1}{2}\mathcal{H}^2 \simeq \frac{2}{\tau^2} & \text{matter-era} \end{cases} \quad (4.82)$$

When the mode functions are outside the horizon ($\frac{k}{a} > 1$), the gravitational wave is a constant while when it is well inside the horizon ($\frac{k}{a} \gg 1$), it is a simple oscillating function scales like $1/a$

$$\gamma(\tau, \mathbf{k}) \propto \begin{cases} \gamma_0 & (\frac{k}{a} \ll H) \\ \frac{1}{a} \sin(\frac{k}{a} + \alpha) & (\frac{k}{a} \gg H) \end{cases}, \quad (4.83)$$

where γ_0 and α (a phase) are both given by the initial conditions; see Fig. 19. The energy density of the gravitational waves is given as

$$\rho_{\text{GW}} = \frac{1}{32\pi G} \sum_{\lambda=+, \times} \langle \dot{\gamma}_\lambda^2 \rangle, \quad (4.84)$$

where the expectation value denotes the statistical averages. For gravitational waves inside the horizon, we have $\dot{\gamma} \propto k \cos(\frac{k}{a} + \alpha)/a^2$ which gives

$$\rho_{\text{GW}} \propto a^{-4},$$

as it is expected from any form of radiation.

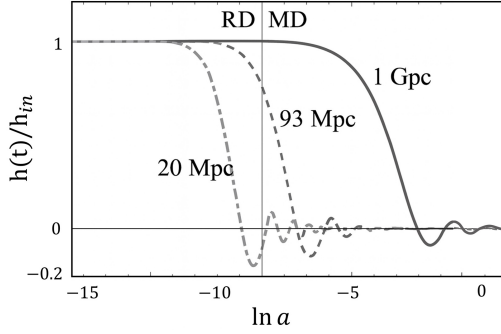


Figure 19: The time evolution of $\gamma_{+,\times}(\tau, k)$, normalized to its initial value as a function of $\ln a$, for three different values of the wavelengths. Image credit: Gravitational Waves. Vol. 2: Astrophysics and Cosmology [157].

After inflation, each mode re-enters the horizon at different times, and the energy density in GWs evolves as radiation, redshifting as a^{-4} . The present-day gravitational waves energy density per logarithmic interval in wavenumber is given by

$$\Omega_{\text{GW}}(k) = \frac{1}{\rho_c} \frac{d\rho_{\text{GW}}}{d \ln k} \propto k^2 \mathcal{P}_h(k) T^2(k), \quad (4.85)$$

where $T(k)$ is the transfer function encoding the evolution of each mode through the radiation- and matter-dominated eras. The late-time gravitational-wave spectrum depends on the horizon re-entry history of inflationary tensor modes as follows.

- Modes re-entering during the radiation era: the transfer function is nearly constant, so the spectrum remains approximately scale-invariant $\Omega_{\text{GW}}(k) \propto \text{const}$.
- Modes re-entering during the matter era: the energy density is less suppressed, scaling as $\Omega_{\text{GW}}(k) \propto k^{-2}$.
- Modes never left the horizon: At very high frequencies, the gravitational wave spectrum exhibits an exponential cutoff. These modes never exited the horizon during inflation and therefore were not stretched or amplified. This sets a natural upper bound on the frequency of primordial GWs, $k_{\text{max}} = a_{\text{end}} H_{\text{end}}$, where a_{end} and H_{end} denotes these quantities at the end of inflation. Assuming instantaneous reheating, the highest frequency of primordial gravitational waves is given by

$$k_{\text{max}} \sim 10^8 \left(\frac{r}{0.01} \right)^{\frac{1}{4}} \text{ Hz}. \quad (4.86)$$

Modes re-entering during radiation domination start oscillating (and redshifting) earlier, leading to greater suppression in Ω_{GW} . Modes that re-enter after matter domination experience less redshift and thus appear less suppressed today. The spectrum of gravitational waves today is typically expressed in terms of frequency (in Hz), which is related

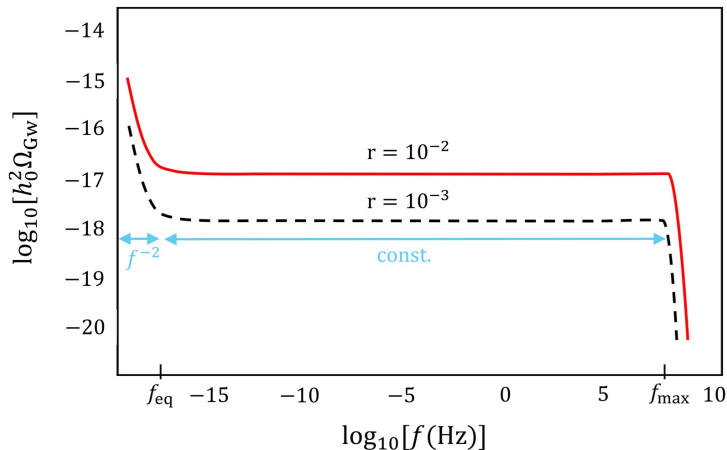


Figure 20: The primordial GW spectrum predicted by inflation (from quantum fluctuations) for $r = 10^{-2}$ (solid red line) and $r = 10^{-3}$ (dashed blue line).

to the comoving wavenumber $k = 2\pi f$. Hence, the overall shape of the primordial GW spectrum today in terms of r and f is a broken power law:

$$\Omega_{\text{GW}}(f) \propto \begin{cases} r f^{-2}, & \text{for } f < f_{\text{eq}}, \\ r, & \text{for } f_{\text{eq}} < f < f_{\text{max}}, \\ \text{exponential cut-off} & \text{for } f > f_{\text{max}}, \end{cases} \quad (4.87)$$

where $f_{\text{eq}} \approx 3 \times 10^{-17}$ Hz corresponds to the mode that re-entered the horizon at the time of matter-radiation equality. This spectral break encodes important information about the thermal history of the Universe and is shown in Fig. 20. Note that the primordial gravitational wave spectrum from inflation can exhibit a richer structure than discussed here once thermalization effects in the early universe are taken into account. In particular, interactions with the thermal plasma and free-streaming SM particles can induce additional damping features and smooth transitions in the spectrum at high frequencies, as shown in Refs. [158, 159].

BBN Bound on the Cosmological GW Background

Big Bang Nucleosynthesis provides a robust upper bound on the total energy density stored in a stochastic background of cosmological gravitational waves. An excess radiation component increases the Hubble expansion rate during nucleosynthesis, thereby altering the neutron-proton freeze-out ratio and the primordial abundances of light elements. This requirement can be expressed as a constraint on the present-day gravitational wave energy density fraction [157]

$$\int_{f_{\text{CMB}}}^{\infty} d \ln q \Omega_{\text{GW},0}(q) \lesssim 3.5 \times 10^{-6}, \quad (4.88)$$

where $\Omega_{\text{GW},0}(q)$ denotes the spectral GW energy density today and $f_{\text{CMB}} \simeq 3 \times 10^{-17}$ Hz is the frequency associated with the comoving Hubble radius at the time of photon decoupling. This bound limits the total gravitational wave radiation present prior to BBN and constrains a wide range of cosmological GW sources, including high-frequency backgrounds inaccessible to current detectors.

4.4.2 Integrated Sachs–Wolfe effect and Primordial GWs

After decoupling, the photon mean free path becomes comparable to the size of the observable Universe, allowing photons to reach our detectors without further scattering (Fig. 15). Along their journey, photon geodesics are subtly perturbed by spacetime inhomogeneities (see Fig. 21). These perturbations give rise to temperature fluctuations, an effect known as the Sachs–Wolfe effect, which arises from scalar and tensor modes of the underlying geometry. In general, the total Sachs-Wolfe effect consists of two components: the original Sachs-Wolfe effect, which arises at the surface of last scattering τ_{dec} by scalar perturbation, and the integrated Sachs-Wolfe (ISW) effect, which accumulates along the photon’s trajectory, $\tau \in (\tau_{\text{dec}}, \tau_0)$, due to the time variation of metric perturbations (both scalar perturbations and GWs).¹⁷ In the following, we only focus on GWs and neglect the contribution of scalar perturbations in the above discussion.

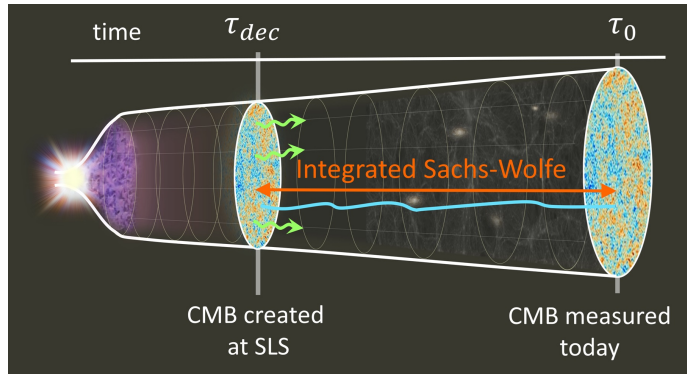


Figure 21: The photon geodesics are perturbed by gravitational fields, e.g., cosmic perturbations. That affects both the direction and energy of photons, contributing to the Integrated Sachs-Wolfe effect. The CMB anisotropies imprinted at the scattering of last surface (SLS) are subsequently altered by cosmic perturbations and large-scale structures encountered along their path from the decoupling time τ_{dec} to the present epoch τ_0 , giving rise to the anisotropies we observe today.

¹⁷Note that τ_{rec} denotes the epoch of recombination, when protons and electrons form neutral hydrogen ($z \sim 1100\text{--}1400$, $T_\gamma \sim 3000$ K). On the other hand, τ_{dec} refers to the epoch of photon decoupling, when the Thomson scattering rate falls below the Hubble expansion rate and CMB photons begin to free-stream; this occurs slightly later, at $z \simeq 1050$ and $T_\gamma \simeq 2800$ K, and defines the true last-scattering surface relevant for primary anisotropies. For the Integrated Sachs–Wolfe (ISW) effect, the line-of-sight integral extends from τ_{dec} to today, since the ISW contribution arises from the evolution of gravitational potentials after decoupling.

The observed anisotropies in the CMB are related to how photons are seen from the cosmic fluid rest frame, i.e., baryon–photon fluid. The photon’s energy measured with respect to the rest frame of the baryon-photon fluid is

$$E(x^\nu) \equiv -P^\mu(x^\nu)u_\mu(x^\nu), \quad (4.89)$$

where $P^\mu = \frac{dx^\mu}{d\lambda}$ is the photon’s 4-momentum and u^μ is the baryon-photon fluid bulk velocity. The photon’s four-momentum, $P^\mu P_\mu = 0$, can be expressed as

$$P^\mu = E\left(1, \frac{1}{a}\hat{n}\right), \quad (4.90)$$

where \hat{n} denotes the unit vector along its direction of propagation. Note that $\hat{n} = -\hat{r}$ where \hat{r} is a radial direction in the celestial sphere (line-of-sight direction), as illustrated in the left panel of Fig. 6. Suppose that a photon emitted with energy E_E at a point, x_E^μ , and is observed at x_O^μ with E_O . Then, the temperature at x_E^μ and at x_O^μ in a rest frame of baryon-photon fluid are given as

$$\frac{E_O}{E_E} = \frac{T_O}{T_E}. \quad (4.91)$$

To understand how evolving gravitational potentials leave imprints on the CMB temperature through the Integrated Sachs–Wolfe (ISW) effect, we must examine how these perturbations influence the propagation of photons. For that purpose, we need to compute the effect of the perturbations on the photon trajectories

$$\frac{dP^\mu}{d\eta} + \Gamma_{\nu\sigma}^\mu(x^\alpha(\eta))P^\nu P^\sigma = 0, \quad (4.92)$$

where $\Gamma_{\nu\sigma}^\mu(x^\alpha(\eta))$ is the Christoffel symbols up to the first order of perturbations. Since our focus is on temperature perturbations, we are particularly interested in the projection of the above equation along the four-velocity u^μ . For the perturbed metric Eq. (4.48), we find the first order perturbed u^μ as $u^\mu = (1 - \Phi, 0, 0, 0)$.

Here, we only consider the contribution of the GWs to the perturbed geodesic trajectory. The perturbed geodesic is

$$\frac{dP^0}{dt} \frac{dt}{d\eta} + \Gamma_{ij}^0(x^\alpha(\eta))P^i P^j = 0, \quad (4.93)$$

in which $\frac{dt}{d\eta} = P^0$ and $\Gamma_{\mu\nu}^0 = a^2\delta_\nu^j\delta_\mu^i(\frac{\dot{a}}{a}\delta_{ij} + \frac{1}{2}\dot{\gamma}_{ij})$. At leading order, we find $a(t)\bar{T}(t) = a_0T_0$ where $\bar{T}(t)$ is the mean CMB temperature at time t . At first order in perturbation, we

arrive at ¹⁸

$$\frac{1}{\bar{T}(t)} \frac{d\delta T(t, \hat{n})}{dt} = -\frac{1}{2} \dot{\gamma}_{ij}(t, \mathbf{x}) \hat{n}^i \hat{n}^j, \quad (4.96)$$

where $\delta T(t, \hat{n})$ denote the perturbed CMB temperature at time t . Integrating the above equation, we find the temperature perturbation today in terms of the perturbations at the time of the photon decoupling, τ_{dec} , as (see Fig. 21)

$$\frac{\Delta T(\hat{n})}{T} = -\frac{1}{2} \left[\int_{\tau_{\text{dec}}}^{\tau_0} d\tau n^i n^j h'_{ij}(\tau, (\tau_0 - \tau)\hat{n}) \right], \quad (4.97)$$

where $r_L = \tau_0 - \tau_{\text{dec}}$. For an intuitive and detailed explanation of the gravitational effects on temperature anisotropy, see [here](#). This discussion is taken up again in Sec. 5.1, where we analyze the role of inflationary gravitational waves in shaping the cosmic microwave background and their manifestation in temperature and polarization anisotropies.

5 Detection Techniques and Observational Frontiers

Gravitational waves span an enormous range of frequencies, the gravitational rainbow illustrated in Fig. 1, from wavelengths comparable to the size of the observable Universe to frequencies of order 10 kHz and beyond, where both compact astrophysical systems and early-Universe cosmology can act as sources. Each portion of this spectrum demands a distinct observational strategy, and taken together these complementary approaches enable a coherent, multi-band view of the gravitational-wave Universe. In this section, we begin by examining how cosmic microwave background polarization, particularly the search for primordial B -modes, provides access to gravitational waves on the largest observable scales, opening a unique window onto the physics of the earliest moments of cosmic history. We then turn to pulsar timing arrays, which exploit the remarkable rotational stability of millisecond pulsars to probe gravitational waves in the nanohertz regime. We summarize both the current observational status and the prospects for next-generation PTA experiments. Next, we outline the physical principles underlying laser interferometric detection of spacetime strain and introduce the current global network of ground-based and space-based interferometers. Finally, we discuss resonant and cavity-based detectors as potential probes of gravitational waves at much higher frequencies.

¹⁸The change in photon energy along its trajectory, including the effects of scalar perturbations, is given by

$$\frac{1}{P^0} \frac{dP^0}{dt} = -\frac{\dot{a}}{a} - \frac{d\Phi}{dt} + \dot{\Psi} + \dot{\Phi} - \frac{1}{2} \dot{\gamma}_{ij} \hat{n}^i \hat{n}^j, \quad (4.94)$$

in which we used $\frac{1}{a} \hat{n} \cdot \nabla \Phi = \frac{d\Phi}{dt} - \dot{\Phi}$ [160]. The full Sachs-Wolfe effect assuming adiabatic initial conditions, is

$$\frac{\delta T}{T} = \frac{1}{3} \Psi(\tau_{\text{dec}}) + \int_{\tau_{\text{dec}}}^{\tau_0} d\tau (\dot{\Phi} + \dot{\Psi} - \frac{1}{2} \dot{\gamma}_{ij} \hat{n}^i \hat{n}^j), \quad (4.95)$$

where the first term is the Sachs-Wolfe effect and the last three terms are the ISW effect.

5.1 CMB Polarization: Imprints of Primordial Gravitational Waves

In addition to the temperature anisotropies, there is more information to be gained by measuring CMB. More precisely, CMB photons are expected to be polarized due to the Thomson scattering by free electrons before decoupling. The polarization of CMB photons provides the cleanest and a promising method to detect primordial gravitational waves. Before turning to CMB polarization, let us briefly pause to introduce the systematic description of light polarization in optics.

The polarization of an electromagnetic wave is described in terms of the Stokes parameters. Consider a monochromatic electromagnetic plane wave that propagates along the direction \hat{x}_3 . Its electric field can be written as the following complex 2-component vector

$$\mathbf{E} = e^{-i(\omega t - \mathbf{k} \cdot \mathbf{x})} \begin{pmatrix} E_1 e^{i\theta_1} \\ E_1 e^{i\theta_2} \\ 0 \end{pmatrix}. \quad (5.1)$$

The coherency matrix is defined as a 2×2 Hermitian operator

$$C = \langle \mathbf{E} \mathbf{E}^\dagger \rangle = \begin{pmatrix} \langle |E_x|^2 \rangle & \langle E_x E_y^* \rangle \\ \langle E_x^* E_y \rangle & \langle |E_y|^2 \rangle \end{pmatrix}, \quad (5.2)$$

where the $\langle \dots \rangle$ denotes the ensemble average. The coherency matrix can be expanded in the basis of Pauli matrices¹⁹ as

$$C = \frac{1}{2} (I \sigma_0 + Q \sigma_3 + U \sigma_1 + V \sigma_2) = \frac{1}{2} \begin{pmatrix} I + Q & U - iV \\ U + iV & I - Q \end{pmatrix}. \quad (5.3)$$

Here, I, Q, U , and V are the Stocks parameters, i.e.,

$$I \equiv \langle E_1^2 \rangle + \langle E_2^2 \rangle, \quad (5.4)$$

$$Q \equiv \langle E_1^2 \rangle - \langle E_2^2 \rangle, \quad (5.5)$$

$$U \equiv 2 \langle E_1 E_2 \cos(\theta_1 - \theta_2) \rangle, \quad (5.6)$$

$$V \equiv 2 \langle E_1 E_2 \sin(\theta_1 - \theta_2) \rangle. \quad (5.7)$$

See Fig. 22 for the polarization corresponding to each of the Stokes parameters.

- The quantity I is the total intensity of the wave, here the temperature anisotropy.
- Q describes the difference between the linear polarization in \hat{e}_1 and \hat{e}_2 directions.
- The U and V parameters give information on the phases. In particular, expanding the wave in the ± 1 helicity polarization states, $\hat{e}_i^{R,L} = 1/\sqrt{2}(\hat{e}_1 \pm i\hat{e}_2)_i$, we have

$$V = \langle E_R^2 \rangle - \langle E_L^2 \rangle, \quad (5.8)$$

¹⁹The Pauli matrices σ_μ are $\sigma_0 = \begin{pmatrix} 1 & 0 \\ 0 & 1 \end{pmatrix}$, $\sigma_1 = \begin{pmatrix} 0 & 1 \\ 1 & 0 \end{pmatrix}$, $\sigma_2 = \begin{pmatrix} 0 & -i \\ i & 0 \end{pmatrix}$, and $\sigma_3 = \begin{pmatrix} 1 & 0 \\ 0 & -1 \end{pmatrix}$.

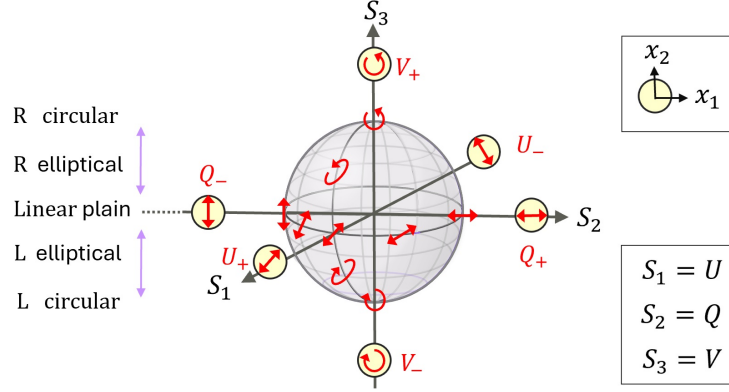


Figure 22: The Poincaré sphere representation of the polarization state of light. Each point on the sphere corresponds to a unique polarization state. The three axes represent the Stokes parameters S_1, S_2, S_3 . Specifically, $S_1 = U$ characterizes linear polarization at $\pm 45^\circ$, $S_2 = Q$ corresponds to linear polarization along horizontal and vertical directions, and S_3 describes circular polarization, distinguishing between right- and left-handed helicities. The radial vector from the center to a point on the sphere represents the full polarization state, and its length gives I_{pol} .

which represents the difference between the positive and negative helicity intensities. The U can be written as

$$U = 2\langle E_R E_L \sin(\theta_R - \theta_L) \rangle. \quad (5.9)$$

- Here Q and U describe the linear polarization, while V quantifies the circular polarization.
- The square of the total polarized intensity of light is

$$I_{\text{pol}}^2 = Q^2 + U^2 + V^2, \quad (5.10)$$

which quantifies how much of the light is polarized, regardless of whether it is linearly or circularly polarized. From that, we can define the degree of polarization as

$$P = \frac{I_{\text{pol}}}{I}, \quad (5.11)$$

which is a quantity equal to or less than one. This leads to the constraint

$$I^2 \geq Q^2 + U^2 + V^2, \quad (5.12)$$

with equality satisfied in the case of fully polarized light.

- The most generic shape of a polarized light is elliptical, which is described by two parameters; polarization angle θ

$$\theta = \frac{1}{2} \tan^{-1}\left(\frac{U}{Q}\right), \quad (5.13)$$

and the ellipticity angle χ

$$\sin(2\chi) = \frac{V}{I_{\text{pol}}}. \quad (5.14)$$

These two parameters fully describe the shape of the ellipse.

Spin-Weight of the Stokes parameters

A spin- s function on the sphere under a rotation of angle φ around the \hat{n} transforms as

$${}_s f(\hat{n}) \rightarrow e^{-is\varphi} {}_s f(\hat{n}). \quad (5.15)$$

Analogous to ordinary spherical harmonics $Y_{\ell m}(\theta, \phi)$ (basis for $s = 0$), there exist spin-weighted spherical harmonics ${}_s Y_{\ell m}(\theta, \phi)$ which form a complete orthonormal basis for spin- s functions

$${}_s f(\hat{n}) = \sum_{\ell=|s|}^{\infty} \sum_{m=-\ell}^{\ell} a_{\ell m}^{(s)} {}_s Y_{\ell m}(\theta, \phi). \quad (5.16)$$

For $s \neq 0$, they are obtained by acting with the spin-raising $\bar{\partial}^+$ and spin-lowering $\bar{\partial}^-$ operators on the ordinary $Y_{\ell m}$. The operators $\bar{\partial}^{\pm}$ has the explicit forms

$$\bar{\partial}^{\pm} = -(\sin \theta)^{\pm s} \left(\frac{\partial}{\partial \theta} \pm \frac{i}{\sin \theta} \frac{\partial}{\partial \phi} \right) [(\sin \theta)^{\mp s}], \quad (5.17)$$

which shift the spin weight as follows

$$\bar{\partial}^{\pm} {}_s f(\hat{n}) \rightarrow {}_{s \pm 1} f(\hat{n}). \quad (5.18)$$

The spin-weighted spherical harmonics are related to the scalar (spin-0) spherical harmonics as

$${}_s Y_{\ell m}(\hat{n}) \equiv \sqrt{\frac{(\ell-s)!}{(\ell+s)!}} (\partial^+)^s Y_{\ell m}(\hat{n}) \quad \text{for } 0 \leq s \leq \ell \quad (5.19)$$

$${}_s Y_{\ell m}(\hat{n}) \equiv \sqrt{\frac{(\ell+s)!}{(\ell-s)!}} (-1)^s (\partial^-)^{-s} Y_{\ell m}(\hat{n}) \quad \text{for } -\ell \leq s \leq 0. \quad (5.20)$$

This implies that only the spherical harmonics with $\ell \geq |s|$ can give rise to ${}_s Y_{\ell m}$. Under the action of parity, $\hat{n} \rightarrow -\hat{n}$, the spin-weighted harmonics transform as

$${}_s Y_{\ell m}(-\hat{n}) = (-1)^{\ell-s} Y_{\ell m}(\hat{n}). \quad (5.21)$$

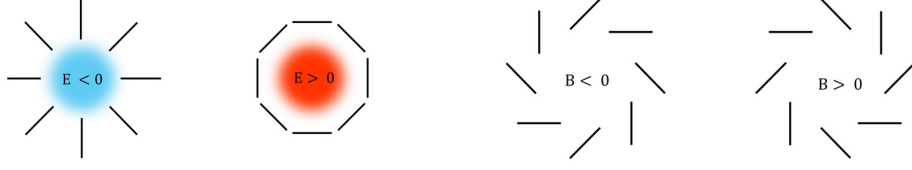


Figure 23: E-mode and B-mode patterns of polarization. The cold and hot spots are shown in blue and red, respectively.

Let us now take a second look at the Stokes parameter. Under a rotation of the polarization basis in the transverse plane by angle ϕ , the Pauli matrices transform as

$$R(\phi) \sigma_0 R^{-1}(\phi) = \sigma_0, \quad R(\phi) \sigma_2 R^{-1}(\phi) = \sigma_2, \quad (5.22)$$

and

$$R(\phi) (\sigma_3 \pm i\sigma_1) R^{-1}(\phi) = e^{\mp 2i\phi} (\sigma_3 \pm i\sigma_1). \quad (5.23)$$

The coherency matrix can be written as

$$C = \frac{1}{2} \left(I\sigma_0 + V\sigma_2 + \frac{1}{2}(Q + iU)(\sigma_3 - i\sigma_1) + \frac{1}{2}(Q - iU)(\sigma_3 + i\sigma_1) \right). \quad (5.24)$$

As a result, the intensity, I , and the helical (circular) polarization, V , remain invariant under rotation, i.e. spin-0. However, the linear polarizations, Q , and U , transforms like spin-2 fields $(Q \pm iU) \rightarrow e^{\mp 2i\phi} (Q \pm iU)$, which implies

$$(Q \pm iU)(\hat{n}) = \sum_{\ell m} a_{\ell m}^{\pm 2} {}_{\pm 2}Y_{\ell m}(\hat{n}). \quad (5.25)$$

From these, we define a scalar quantity (E) and a pseudo-scalar quantity (B) (see Fig. 23), i.e.

$$(Q \pm iU)(\hat{n}) = - \sum_{\ell m} (a_{\ell m}^E \pm i a_{\ell m}^B) {}_{+2}Y_{\ell m}(\hat{n}). \quad (5.26)$$

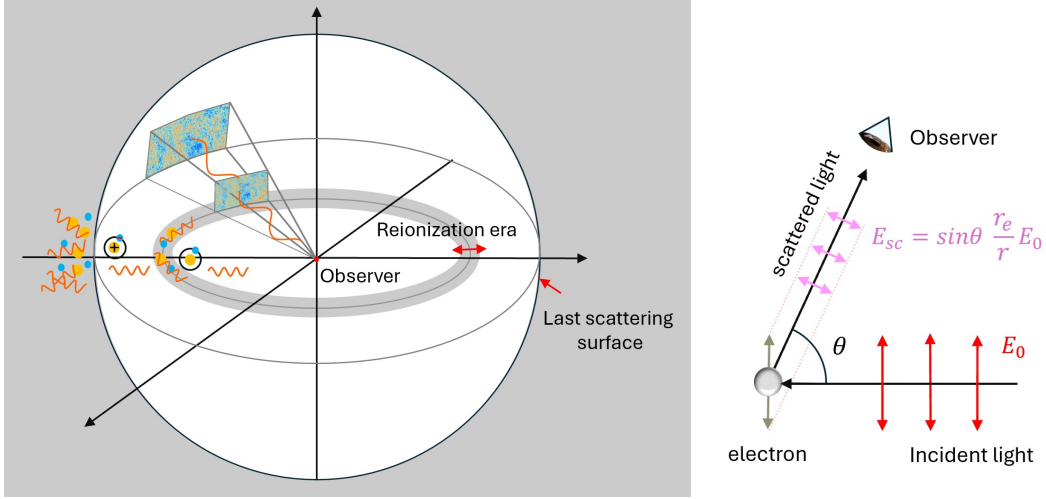


Figure 24: Left panel: Schematic of the celestial sphere showing the observable Universe, where the radial coordinate r corresponds to cosmological redshift, ranging from the surface of last scattering ($z \approx 1100$) to the observer today ($z = 0$), with the reionization era marked in the interval $6 \lesssim z \lesssim 10$. The shaded regions in gray denote the redshifts at which the Universe was ionized. Right panel: Thomson scattering of an electromagnetic wave by a free electron. The incident photon with wavevector \mathbf{k} is scattered into direction \mathbf{k}' at polar angle θ .

Thomson Scattering in an Anisotropic Background

After decoupling at the surface of last scattering ($z \simeq 1100$), CMB photons free-stream toward us. Along the way, mainly during reionization, they can rescatter off free charges via Thomson scattering. In the Thomson limit ($h\nu \ll mc^2$), the differential cross section is

$$\frac{d\sigma_T}{d\Omega} = \frac{r_q^2}{2} (1 + \cos^2 \theta), \quad r_q \equiv \frac{q^2}{4\pi\epsilon_0 mc^2}. \quad (5.27)$$

Here θ is the scattering angle, given by $\cos \theta = \boldsymbol{\epsilon}_{\text{out}} \cdot \boldsymbol{\epsilon}$, and q , m , and r_q are the particle's charge, mass, and classical radius. Given that $(m_e/m_p)^2 \approx 10^{-7}$ and $\sigma_T \propto 1/m^2$, electrons are far more efficient scatterers than protons.

A single Thomson scattering converts a local quadrupole anisotropy of the incident radiation into linear polarization of the CMB, producing the observed large-scale E -mode signal. In the nonrelativistic limit, the electron's equation of motion is

$$m_e \ddot{\mathbf{x}}(t) = -e \mathbf{E}_{\text{inc}}(t), \quad \mathbf{a}(t) = -(e/m_e) \mathbf{E}_{\text{inc}}(t),$$

so the acceleration is parallel to $\hat{\boldsymbol{\epsilon}}$. The far-zone (radiation) electric field from an accelerating charge is

$$\mathbf{E}_{\text{sc}}(\mathbf{r}, t) = \frac{e}{4\pi\epsilon_0 c^2 r} \hat{\mathbf{n}} \times (\hat{\mathbf{n}} \times \mathbf{a}(t_r)) = \frac{r_e}{r} E_0 \sin \theta, \quad (5.28)$$

where $\hat{\mathbf{n}}$ points from the electron to the observer and t_r is the retarded time (see Fig. 24).

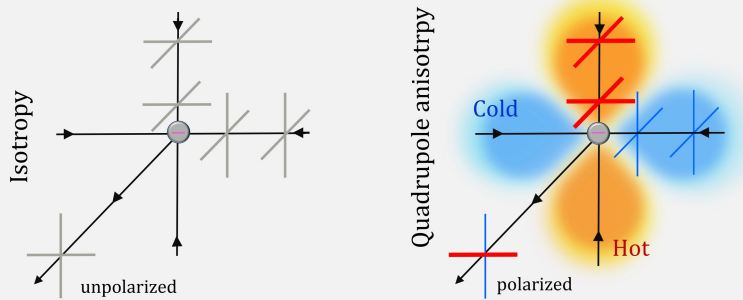


Figure 25: Illustration of Thomson scattering of initially unpolarized CMB photons. For an isotropic radiation field or one with only dipole anisotropy, the scattered radiation remains unpolarized. Polarization arises only when a quadrupole anisotropy is present, making the quadrupole the lowest-order multipole that generates CMB polarization.

In the last equality, we used $\mathbf{a} \parallel \hat{\mathbf{e}}$, while θ is the angle between $\hat{\mathbf{e}}$ (the acceleration direction) and $\hat{\mathbf{n}}$, and r_e is the classical electron radius. For fixed incident polarization, the corresponding intensity is $I_{\text{sc}}(\theta) \propto |E_{\text{sc}}|^2 \propto \sin^2 \theta$, the characteristic dipole radiation pattern. Now, let $\hat{\mathbf{n}}$ be the observed line of sight and (θ, ϕ) the angles of the incident direction $\hat{\mathbf{n}}'$ in the scattering frame. For a generic unpolarized incident intensity $I(\hat{\mathbf{n}}')$, the scattered linear polarization is

$$(Q \pm iU)(\hat{\mathbf{n}}, \tau) = \frac{3\sigma_T}{16\pi} n_e(\tau) \int d\Omega' \sin^2 \theta e^{\pm 2i\phi} I(\hat{\mathbf{n}}', \tau), \quad (5.29)$$

where $e^{\pm 2i\phi}$ is the spin- ± 2 phase from the scattering geometry, σ_T is the Thomson cross section, and $n_e(\tau)$ is the electron number density at time. Expanding the incident field in spherical harmonics, $I(\hat{\mathbf{n}}') = \sum_{\ell m} a_{\ell m} Y_{\ell m}(\hat{\mathbf{n}}')$, and using Eq. (5.25), the angular integral in Eq. (5.29) picks out $l \geq 2$. More precisely, the linear polarization, $Q \pm iU$, transforms as a spin- ± 2 field on S^2 , so it admits an expansion in ${}_{\pm 2}Y_{\ell m}$ and therefore vanishes unless $\ell \geq |s| = 2$. Thus, neither the monopole ($l = 0$) nor the dipole ($l = 1$) components of the incident radiation generate linear polarization. The leading contribution arises from a nonzero quadrupole anisotropy, as illustrated in Fig. 25. In other words, Thomson scattering converts a quadrupole intensity anisotropy of the incident radiation into linear polarization on the sky.

Along the line of sight from last scattering to today, polarization is sourced wherever free electrons see a local temperature quadrupole. In essence, the observed polarization anisotropies can be expressed as an integral over conformal time

$$(Q \pm iU)(\hat{\mathbf{n}}) = \int_{\tau_{\text{SLS}}}^{\tau_0} d\tau g(\tau) \mathcal{S}_{\pm 2}(\tau, \hat{\mathbf{n}}), \quad (5.30)$$

where $g(\tau) = a(\tau)n_e(\tau)\sigma_T e^{-\tau_e(\tau)}$ is the visibility function and $\mathcal{S}_{\pm 2}(\tau, \hat{\mathbf{n}})$ is the polarization source term. Given that the polarization is related to the electron number density in the Universe, there are two key epochs: (i) recombination, when the mean free path grows rapidly and a finite quadrupole develops, creating the acoustic E -mode pattern; and (ii) late reionization (see left panel of Fig. 24). To compute C_ℓ^{EE} and C_ℓ^{BB} , cosmologists first solve the linear cosmic perturbation equations to obtain the polarization source from primordial anisotropies. This source feeds into the line-of-sight integral, which is then projected onto spin-2 spherical harmonics to extract E- and B-mode components. Tools like CAMB and CLASS perform this numerically [161]. A detailed computation is beyond the scope of the current review, and the final result of these impressive calculations is shown in Fig. 26, where the TT , EE , and BB spectra (both lensing and primordial) are presented. In the following, we summarize the main features of the CMB polarization spectra.

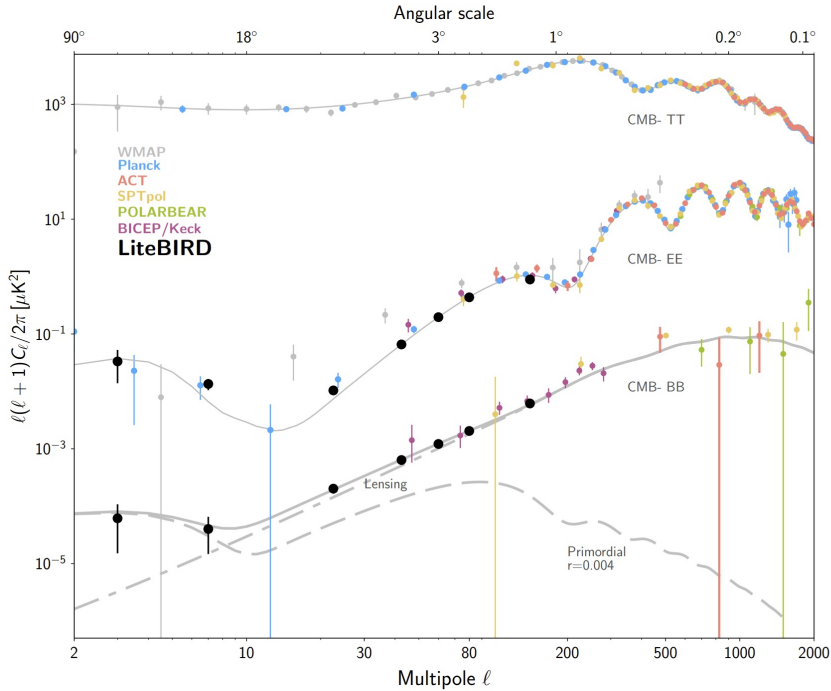


Figure 26: CMB power spectra for temperature anisotropy (CMB-TT), E-mode polarization (CMB-EE), and B-mode polarization (CMB-BB) are shown. The solid curves represent the predictions of the best-fit Λ CDM model, including a scale-invariant tensor perturbation with a tensor-to-scalar ratio $r = 0.004$. For comparison, the thin dashed line indicates the contribution of tensor modes to the B-mode spectrum alone. Also displayed are current measurements of the CMB power spectra (colored points) and the projected polarization sensitivity of LiteBIRD (black points). Image credit: LiteBIRD mission [50].

- The scalar quantities E and B , completely determine the linear polarization fields.
- The E -mode is curl-free and even under the action of parity. Its polarization vectors

are radial around cold spots (under dense) and tangential around hot spots (over dense).

- The B -mode is the divergence-free field and odd under parity. Its polarization vectors have vorticity around the under- and over-dense areas.
- The angular power spectra are defined as

$$C_l^{XY} \equiv \frac{1}{2l+1} \sum_m \langle a_{lm}^X a_{lm}^Y \rangle \quad \text{where } X, Y = T, E, B. \quad (5.31)$$

The autocorrelations of E - and B -modes, denoted by EE and BB , are presented in Fig. 26.

- At linear order, scalar (density) perturbations source only E -modes, while tensor perturbations (gravitational waves) generate both E - and B -modes.
- At nonlinear order, gravitational lensing by large-scale structure distorts E -modes into B -modes, producing a lensing-induced B -mode signal at small angular scales.

Primordial gravitational waves and B -modes have not yet been detected. Recalling that scalar perturbations do not generate B -modes, while tensor (gravitational wave) perturbations do, a detection of primordial B -modes would be a distinctive fingerprint of primordial gravitational waves and thus a powerful confirmation of inflation. This is the ambitious goal of the upcoming LiteBIRD satellite mission: to measure the CMB polarization with unprecedented sensitivity and probe tensor-to-scalar ratios as low as $r = 10^{-3}$, pushing the frontier of our understanding of the early Universe. For additional information on LiteBIRD, see [50]. CMB B -modes also offer a unique window into a broad range of new physics including parity violation, relic particle species. We refer the interested reader to the recent reviews article [5] for a comprehensive overview. Finally, CMB spectral distortions act as an intermediate probe of primordial gravitational waves, bridging B -mode polarization measurements and pulsar timing array observations [162].

5.2 Pulsar Timing Arrays: Precision Cosmic Clocks for GW Detection

A population of exceptionally stable millisecond pulsars, timed with precisions approaching 100 ns over many years, acts as an array of cosmic clocks. Their remarkably regular pulses are subtly and coherently disturbed by gravitational waves propagating along the Earth–pulsar line of sight: the passing waves perturb the null geodesics along the photon’s path to Earth. A global collaboration now monitors dozens of these pulsars with ever-increasing precision, effectively transforming the Milky Way into a galaxy-scale detector for nanohertz gravitational waves through pulsar timing arrays (PTAs).

By tracking the arrival times of pulses from a network of pulsars, PTAs are sensitive to GWs in the nanohertz band. Crucially, PTAs are sensitive not only to individual deterministic sources, but also to stochastic gravitational wave backgrounds (SGWBs). Indeed, the strongest existing bounds on the primordial nanohertz background arise from

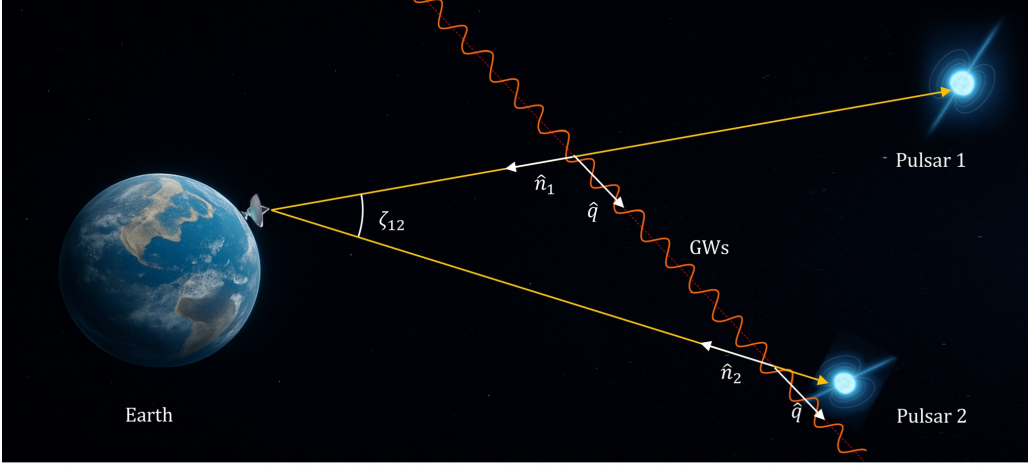


Figure 27: Pulsar timing arrays detect nanohertz gravitational waves by measuring timing residuals across widely separated millisecond pulsars.

PTA measurements, providing leading constraints on the gravitational wave energy density in this frequency band.

Pulsar timing arrays operate by monitoring the times of arrival (TOAs) of radio pulses from their ensemble of millisecond pulsars, whose exceptional rotational stability makes them superb astrophysical clocks [163, 164]. A passing GW propagating in direction \hat{q} perturbs the spacetime metric along the photon trajectory, inducing a small but coherent shift in the observed pulse frequency. The measured fractional frequency shift at Earth can be expressed as

$$\frac{\delta\nu(t)}{\nu} = \frac{1}{2} \frac{\hat{n}^i \hat{n}^j}{1 - \hat{q} \cdot \hat{n}} [\gamma_{ij}(t_e, \mathbf{x}_e) - \gamma_{ij}(t_p, \mathbf{x}_p)], \quad (5.32)$$

where \hat{n} points from the pulsar to Earth, t_e is the reception time at Earth, and $t_p = t_e - L(1 + \hat{q} \cdot \hat{n})$ is the retarded emission time at the pulsar, with L the pulsar distance. Here $\gamma_{ij}(t_e, \mathbf{x}_e)$ denotes the gravitational wave metric perturbation evaluated at the Earth when the pulse is received, the Earth term, while $\gamma_{ij}(t_p, \mathbf{x}_p)$ denotes the perturbation at the pulsar at the time of emission, constituting the pulsar term. The corresponding timing residual is obtained by integrating the frequency shift as

$$R(t) = \int^t dt' \frac{\delta\nu(t')}{\nu}. \quad (5.33)$$

Gravitational waves in the nanohertz band ($f \sim 10^{-9}$ – 10^{-7} Hz) induce correlated timing residuals across the pulsars in a PTA. The essential observable for a stochastic background is the two-point function

$$C_{ab} \equiv \langle R_a(t) R_b(t) \rangle, \quad (5.34)$$

which captures the GW-induced covariance between pulsars a and b . This geometry is illustrated schematically in Fig. 27. The pulsar-pair angular separation ζ_{ab} is defined as

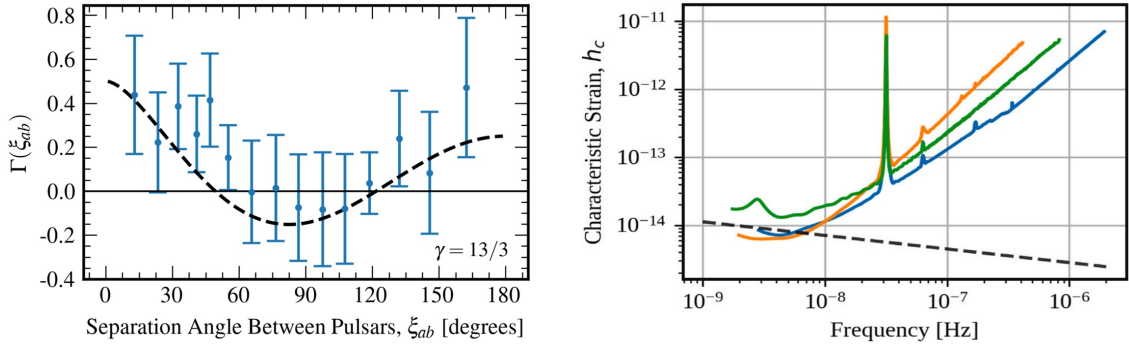


Figure 28: Left panel: Angular correlation of pulsar timing residuals measured by NANOGrav (blue points with uncertainties) [24], shown as a function of the separation angle between pulsar pairs. The dashed black curve is the Hellings–Downs prediction for an isotropic GWB with spectral index $\gamma = 13/3$. The data exhibit the characteristic quadrupolar trend expected from gravitational waves, whereas the absence of a signal would yield correlations consistent with zero across all angles. Image credit: The NANOGrav Collaboration [24]. Right panel: Characteristic strain sensitivity curves for current pulsar timing array (PTA) collaborations. The blue, orange, and green curves show the sensitivities of EPTA+InPTA, NANOGrav, and PPTA, respectively. The dashed black line indicates the joint-median sensitivity obtained by combining information from all PTA datasets. Image credit: [165].

the angle between the sky directions of pulsars a and b

$$\cos \zeta_{ab} = \hat{\mathbf{n}}_a \cdot \hat{\mathbf{n}}_b. \quad (5.35)$$

For an isotropic and stationary gravitational wave background, this covariance depends only on the angular separation between the pulsars, and may be written as

$$C_{ab} = \Gamma_{ab}(\zeta_{ab}) \sigma_{\text{GW}}^2, \quad (5.36)$$

where σ_{GW}^2 encodes the overall amplitude of the background and $\Gamma_{ab}(\zeta_{ab})$ is the geometrical overlap reduction function which depends only on the angular separation between the pulsars when the background is isotropic. In general relativity, only the two transverse–traceless tensor modes are present. In this special case, ξ_{ab} reduces to a single, characteristic quadrupolar correlation function,

$$\Gamma_{ab}^{\text{HD}} = \frac{3}{2} \left[\frac{1 - \cos \zeta_{ab}}{2} \right] \ln \left(\frac{1 - \cos \zeta_{ab}}{2} \right) - \frac{1}{4} \left[\frac{1 - \cos \zeta_{ab}}{2} \right] + \frac{1}{2} \delta_{ab}, \quad (5.37)$$

known as the Hellings–Downs (HD) curve. Notice that the term Hellings–Downs correlation therefore refers specifically to the ORF produced by an isotropic background of tensor gravitational waves in general relativity, and does not generally apply when additional polarizations or modified propagation effects appear in modified–gravity theories.

Recent PTA measurements provide compelling evidence for a nanohertz gravitational wave background (see left panel of Fig. 28). The NANOGrav 15-year data set [24] identifies a common-spectrum process exhibiting the expected Hellings–Downs correlations [24].



Figure 29: The International Pulsar Timing Array (IPTA), a worldwide network of radio telescopes that times an ensemble of millisecond pulsars to search for nanohertz gravitational waves. Image credit: H Thankful Cromartie.

Independent analyses by the European Pulsar Timing Array (EPTA) together with the Indian Pulsar Timing Array (InPTA) [166–168], the Parkes Pulsar Timing Array (PPTA) [169, 170], and the Chinese Pulsar Timing Array (CPTA) [171] report consistent signals. Together, these regional collaborations form the International Pulsar Timing Array (IPTA), and collectively these results mark the emergence of gravitational-wave astronomy in the nanohertz regime (see Fig. 29), likely dominated by the cosmic population of slowly inspiraling supermassive black-hole binaries. The characteristic strain sensitivity curves of current PTA collaborations are shown in the right panel of Fig. 28. Future observations with the Square Kilometre Array (SKA) are expected to significantly improve timing precision and greatly enhance PTA sensitivity [172, 173]. Astrometric observations provide an alternative to pulsar timing arrays for probing the stochastic GWB and its angular properties [27, 28]. Together with LISA and ground-based interferometers, PTAs anchor a coordinated multi-band gravitational wave network spanning nearly nine orders of magnitude in frequency, enabling a unified and comprehensive view of compact-object populations and their evolution across cosmic time.

5.3 Laser Interferometry: Earth- and Space-Based GW Observatories

The idea of detecting gravitational waves using laser interferometry dates back to the early 1960s, ultimately culminating in the construction of the LIGO and Virgo observatories, whose landmark detections opened an entirely new observational window onto the Universe [4] (see Fig. 30). These achievements established laser interferometers as the premier tools for probing gravitational waves in the audio-band and demonstrated, for the first time, the direct measurability of spacetime dynamics. To set the stage for the methods reviewed in this section, let us begin with a brief overview of Michelson interferometers and the physical principles that govern their response to passing gravitational waves. This foundational framework will allow us to understand how modern detectors extract minute strain signals

from noise and how their design has evolved into the sophisticated global network operating today.

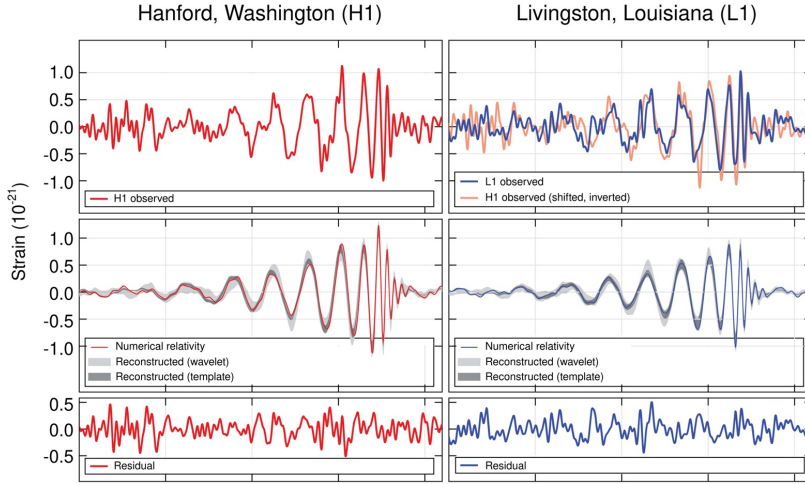


Figure 30: Time-domain strain data for the first directly detected gravitational wave event, GW150914, as measured by the LIGO Hanford (H1) and Livingston (L1) detectors. The top panels show the observed detector strains, with the Livingston trace time-shifted and inverted to account for the light-travel delay and detector orientation. The middle panels compare the data with numerical-relativity waveforms and reconstructed signals obtained via wavelet and template methods, demonstrating the consistency of the inspiral–merger–ringdown signal with a binary black-hole coalescence. The bottom panels show the residuals after subtraction of the best-fit waveform. Image credit: LIGO Scientific Collaboration and Virgo Collaboration [4].

Michelson Interferometer

Consider a laser emitting monochromatic light in direction \hat{x} with an electric field

$$\vec{E}_{\text{in},1}(t, \mathbf{x}) = \begin{pmatrix} E_{\text{in},1} \\ 0 \end{pmatrix} \quad \text{with} \quad E_{\text{in},1} = E_0 e^{-i(\omega_L t - \mathbf{k}_L \cdot \mathbf{x})}, \quad (5.38)$$

where ω_L is the laser frequency, \mathbf{k}_L its wavevector, and E_0 the amplitude. The laser beam is directed onto a beam splitter, which divides it into two components of equal probability amplitude: one propagating along the \hat{x} -axis and the other along the orthogonal \hat{y} -axis. A lossless 50:50 beam splitter (half-reflecting, half-transmitting mirror) can be described by a 2×2 unitary matrix, beam-splitter transfer matrix, as

$$\mathbf{U} = \frac{1}{\sqrt{2}} \begin{pmatrix} 1 & i \\ i & 1 \end{pmatrix}. \quad (5.39)$$

The factor of i corresponds to a relative $\pi/2$ phase shift for the reflected beams. This convention ensures unitarity, i.e. total intensity is conserved, and the beams interfere correctly. It thus splits the initial laser electric field into $\mathbf{E}_{\text{spl},1}$ as

$$\mathbf{E}_{\text{spl},1} = \mathbf{U} \mathbf{E}_{\text{in},1}. \quad (5.40)$$

Next, each beam travels down its respective arm, reflects off a mirror at the far end, and returns to the beam splitter. We place the origin of the coordinate system at the beam splitter. The mirror terminating arm 1 is located at $(L_x, 0)$, while the mirror at the end of arm 2 is positioned at $(0, L_y)$. At this point we have

$$E_{\text{ref},1} = -\frac{E_0}{\sqrt{2}} e^{-i(\omega_L t - 2k_L L_x)}, \quad E_{\text{ref},2} = -i \frac{E_0}{\sqrt{2}} e^{-i(\omega_L t - 2k_L L_y)}. \quad (5.41)$$

The beam splitter then recombine and re-split the two lights. In the recombination stage, the returning beams impinge on opposite faces of the beam splitter compared to the forward pass. This geometric reversal flips the sign of the reflection coefficient for one arm, represented compactly by the diagonal surface matrix

$$\mathbf{S} = \boldsymbol{\sigma}_3 = \begin{pmatrix} 1 & 0 \\ 0 & -1 \end{pmatrix}. \quad (5.42)$$

Hence, the total transformation for the returning fields is given by $\mathbf{U} \mathbf{S}$, i.e.

$$\mathbf{E}_{\text{out}} = \mathbf{U} \mathbf{S} \mathbf{E}_{\text{ref}} = -\frac{E_0}{2} e^{-i\omega_L t} \begin{pmatrix} e^{2ik_L L_y} + e^{2ik_L L_x} \\ i(e^{2ik_L L_x} - e^{2ik_L L_y}) \end{pmatrix}. \quad (5.43)$$

Consequently, when the arm lengths are equal ($L_x = L_y$), one output port remains dark while the other is bright. We put the photodetector at the dark port. The total power recorded at the photodetector is proportional to

$$|E_{\text{det}}|^2 = E_0^2 \sin^2(k_L(L_x - L_y)). \quad (5.44)$$

Thus, any variation in the relative arm lengths induces a corresponding modulation in the detected power (see Fig. 31).

Interaction of Interferometer with Gravitational Waves

We now turn to how this fundamental principle enables the detection of GWs. For clarity, let us consider a wave with only the plus polarization propagating along the z -axis, i.e.

$$ds^2 = -c^2 dt^2 + [1 + h_+(t, z)] dx^2 + [1 - h_+(t, z)] dy^2 + dz^2, \quad (5.45)$$

where $h_+(t, z) = h_0 \cos(\omega_{gw} t - k_{gw} z)$. In the $z = 0$ plane of the interferometer, we therefore have

$$h_+(t) = h_0 \cos \omega_{gw} t. \quad (5.46)$$

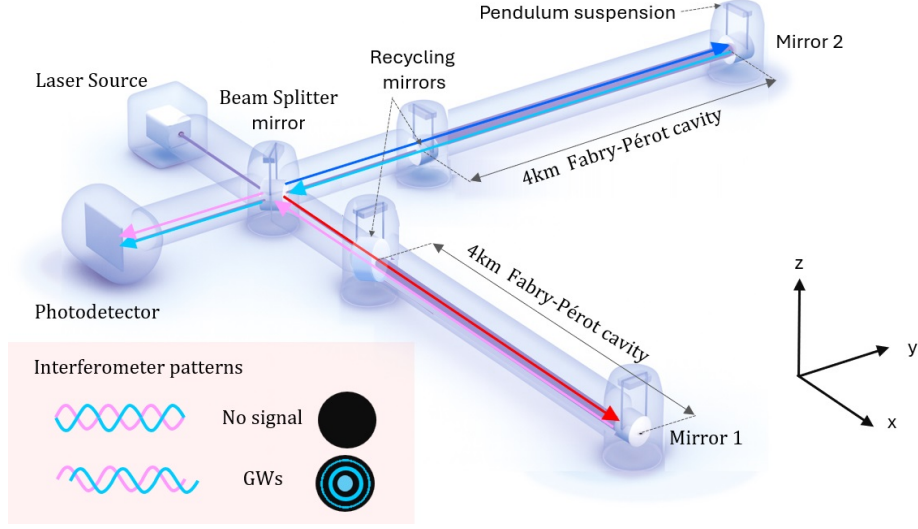


Figure 31: The LIGO detector operates as a Michelson interferometer: passing gravitational waves alternately stretch one arm and compress the other, inducing a phase shift in the light at the beam splitter that produces an interference pattern at the output.

Photons propagate along null geodesics, $ds^2 = 0$. For light traveling in arm 1, the path is, to first order in h_0 ,

$$dx = \pm c dt \left(1 - \frac{1}{2} h_+(t)\right), \quad (5.47)$$

where the plus sign corresponds to propagation from the beam splitter to the mirror, and the minus sign to the return trip.

In the TT gauge description, the coordinates of the mirrors and of the beam-splitter are not affected by the passage of the wave and the physical effect of the GW is manifested in the fact that it affects the propagation of light between these fixed points. Consider a photon that leaves the beam-splitter at a time $t_{\text{spl},1}$. It reaches the mirror, at the fixed coordinate $x = L_x$, at a time $t_{\text{ref},1}$ obtained

$$L_x = c \int_{t_{\text{spl},1}}^{t_{\text{ref},1}} dt \left[1 - \frac{1}{2} h_+(t)\right] = c(t_{\text{ref},1} - t_{\text{spl},1}) - \frac{c}{2} \int_{t_{\text{spl},1}}^{t_{\text{ref},1}} h_+(t) dt. \quad (5.48)$$

Then the photon is reflected and reaches again the beam-splitter at a time $t_{\text{out},1}$ obtained integrating with the minus sign

$$L_x = c(t_{\text{out},1} - t_{\text{ref},1}) - \frac{c}{2} \int_{t_{\text{ref},1}}^{t_{\text{out},1}} h_+(t) dt. \quad (5.49)$$

As a result, the arrival time $t_{\text{out},1}$ after a round trip in the arm-1 is

$$t_{\text{out},1} - t_{\text{spl},1} = \frac{1}{2} \int_{t_{\text{spl},1}}^{t_{\text{out},1}} h_+(t) dt + \frac{2L_x}{c}. \quad (5.50)$$

Given that the GWs is small, we can solve it perturbative for $t_{\text{out},1}$ as

$$t_{\text{out},1} - t_{\text{spl},1} \simeq \frac{1}{2} \int_{t_{\text{spl},1}}^{t_{\text{spl},1} + \frac{2L_x}{c}} h_+(t) dt + \frac{2L_x}{c}, \quad (5.51)$$

which gives

$$t_{\text{out},1} - t_{\text{spl},1} \simeq \frac{L_x}{2c} \frac{\sin(\omega_{\text{gw}} L_x / c)}{\omega_{\text{gw}} L_x / c} h_0 \cos(t_{\text{spl},1} + L_x / c) + \frac{2L_x}{c}. \quad (5.52)$$

Since LIGO is fundamentally a time-delay interferometer, it is necessary to determine the corresponding travel time for the second arm. Doing the same analysis for arm-2, we find

$$t_{\text{out},2} - t_{\text{spl},2} \simeq -\frac{L_y}{2c} \frac{\sin(\omega_{\text{gw}} L_y / c)}{\omega_{\text{gw}} L_y / c} h_0 \cos(t_{\text{spl},1} + L_y / c) + \frac{2L_y}{c}. \quad (5.53)$$

Now, we set

$$L = L_x = L_y, \quad t = t_{\text{out},1} = t_{\text{out},2}, \quad (5.54)$$

and find the total phase difference induced by GWs in the Michelson interferometer as

$$\Delta\phi = \frac{\omega_L L}{c} \frac{\sin(\omega_{\text{gw}} L / c)}{\omega_{\text{gw}} L / c} h(t - L / c). \quad (5.55)$$

Therefore, the total power observed at the photodetector, $P \sim |E_{\text{det}}|^2$, is modulated by the GW signal.

For a simple Michelson interferometer with arm length $L = 4$ km the GW-induced single-pass response contains $\sin(\omega_{\text{gw}} L / c)$; the condition for maximal response, $\sin(\omega_{\text{gw}} L / c) = 1$, occurs at $\omega_{\text{gw}} L / c = \pi / 2$, i.e.

$$\omega_{\text{gw}} = \frac{\pi c}{2L}, \quad f_{\text{gw}} = \frac{c}{4L} \simeq 1.9 \times 10^4 \text{ Hz}. \quad (5.56)$$

In contrast, LIGO is designed to detect signals at frequencies that are orders of magnitude lower, down to ~ 10 Hz, which would correspond to an optimal arm length

$$L_{\text{opt}} = \frac{c}{4f_{\text{gw}}} \simeq 7500 \text{ km}, \quad (5.57)$$

far exceeding any feasible terrestrial baseline. LIGO instead operates in the long-wavelength regime ($\omega_{\text{gw}} L / c \ll 1$), where the interferometer response is nearly flat, and achieves high sensitivity through Fabry–Pérot arm cavities, which increase the photon storage time by a factor of $\mathcal{O}(10^2)$ (see Fig. 32). The effective optical path length is thus enhanced to $\sim 10^3$ km while keeping the physical arms at 4 km, allowing the detector to probe frequencies across the 10–10³ Hz observational band [4, 174].

Advanced LIGO can detect compact binaries with total masses up to $\mathcal{O}(10^2) M_{\odot}$; however, more massive systems, such as supermassive black hole binaries, radiate at lower frequencies, beyond the reach of ground-based detectors. To extend sensitivity, next-generation observatories will employ advanced technologies to form a global network of

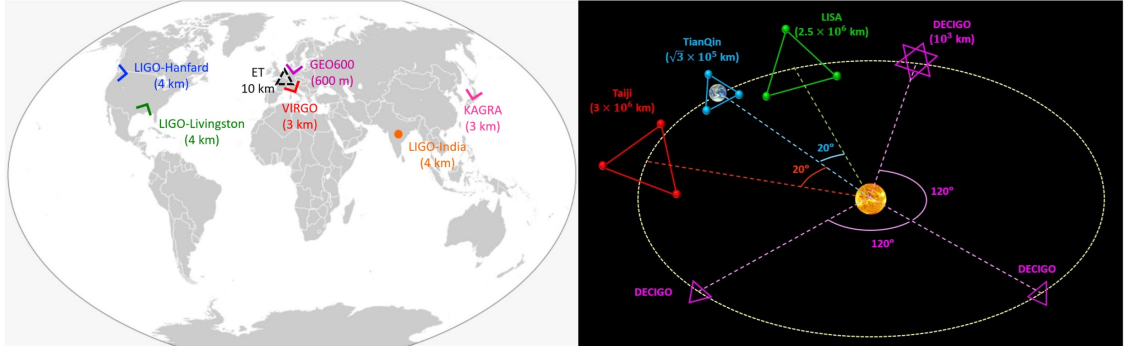


Figure 32: Network of laser interferometer gravitational wave detectors on Earth (left) and in space (right). The terrestrial detectors are L-shaped Michelson interferometers with kilometre-scale arms, including LIGO, which began its first observing run in 2015, Virgo, which joined in 2017 [4], and KAGRA, operational since 2020 [30], together establishing the first global ground-based gravitational wave network. Forthcoming facilities, LIGO–India, expected to begin observations in the early 2030s [31], and the Einstein Telescope, planned for the mid-2030s to 2040s [32], will further extend this network’s reach. In contrast, proposed space-based interferometers will form triangular constellations with arm lengths a million times larger, of order 10^6 km, dramatically enhancing sensitivity to low-frequency gravitational waves. The LISA mission is scheduled for launch around 2030 [29], while several complementary proposals, Taiji [175, 176], TianQin [177], and DECIGO [178], aim to explore similar frequency bands with distinct orbital configurations and designs. Image credit: CERN Courier Feature (Aug 2023) [179].

terrestrial interferometers, probing gravitational waves across the ground-accessible frequency band (~ 1 Hz–10 kHz). At still lower frequencies, they will be complemented by space-based missions and completing a multi-band gravitational wave detection network spanning from 10^{-4} Hz to the kilohertz regime. Fig. 32 illustrates the global network of ground-based laser-interferometer detectors, while their corresponding sky sensitivities are shown in Fig. 33. Atom interferometry offers a complementary route to established laser-interferometric techniques for GW detection [33–35]. On Earth, several long-baseline cold-atom experiments are under construction or commissioning [36–38], while large-scale facilities such as ELGAR [39] and AION [40] are being developed. In space, ambitious mission concepts such as AEDGE [41], STE-QUEST [42], and CAL/MAIUS [43] aim to extend atom-interferometric sensitivity toward even lower GW frequencies. Together, these terrestrial and orbital instruments target the mid-frequency GW band, approximately 10^{-2} to 1 Hz.

5.4 Photonic Qumodes: a Cutting-Edge Quantum Platform for GW Detection

Gravitational waves have opened an unprecedented observational window onto the universe, yet this window currently extends only up to frequencies of order 10 kHz. The detection of higher-frequency gravitational waves (HFGWs) remains an open frontier and

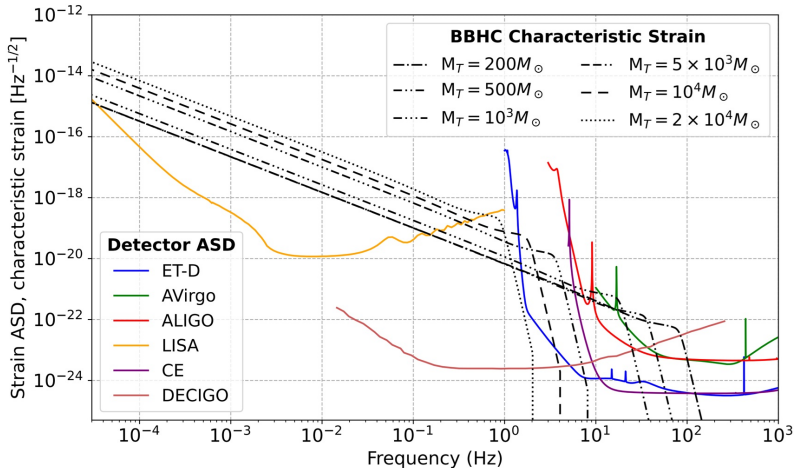


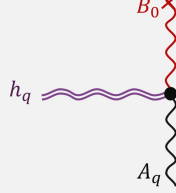
Figure 33: Sensitivity curves of current and future laser-interferometer gravitational wave detectors (solid colored lines), including ET-D, Advanced Virgo, Advanced LIGO, LISA, Cosmic Explorer (CE), and DECIGO. The dashed black curves correspond to the characteristic strain amplitude and associated frequencies of intermediate-mass black-hole binaries with total masses between 2×10^2 to $2 \times 10^4 M_\odot$, assuming a luminosity distance of $d_L = 1$ Gpc. These trajectories illustrate how binaries of different masses sweep through the sensitivity bands of detectors across multiple frequency decades. Image credit: The Science of the Einstein Telescope [32].

an area of active research and development. Such HFGWs may originate from a wide range of cosmological and astrophysical processes, and could even be generated in laboratory settings through the conversion of high-intensity laser fields (see [180] and the references therein). Their observation would provide access to rich new information about the early universe, particle physics, and potentially the quantum nature of gravity itself. Detecting gravitational waves at frequencies above that regime, however, requires experimental strategies fundamentally different from those employed by large-scale laser interferometers. As the GW frequency increases, the corresponding wavelength becomes much shorter than any practical detector baseline, leading to a rapid degradation of the strain sensitivity of conventional interferometric techniques. This limitation has motivated the exploration of alternative detection concepts that rely not on large spatial separations, but on resonant enhancement, electromagnetic interactions, and quantum-coherent effects.

Joseph Weber pioneered the first experimental searches for gravitational waves using resonant bar detectors operating in the kilohertz regime [181], thereby initiating the exploration of gravitational waves at the highest frequencies accessible at the time and laying the conceptual foundations for modern high-frequency GW detection. The main experimental approaches currently pursued for HFGW detection include high-frequency extensions of laser interferometers [182, 183], resonant mass detectors [184], modern resonant mechanical sensors [48, 185, 186], electromagnetic oscillators such as microwave cavities [187, 188], pho-

ton (re-)generation experiments [49, 189–194], and other electromagnetic conversion–based schemes. Comprehensive reviews, sensitivity estimates, and discussions of experimental implementations can be found in Ref. [180] and the references therein. In the following, we focus on a brief overview of photon (re-)generation experiments and highlight recent advances in this direction.

Graviton–Photon Transitions: The Gertsenshtein Effect



Graviton + Magnetic field \rightarrow Photon

In a seminal 1962 paper, Gertsenshtein pointed out that electromagnetic and gravitational waves can interconvert in the presence of a static magnetic field, i.e. the Gertsenshtein effect [195]. This observation provides an early and concrete example of the coupling between electromagnetism and gravity at the level of field theory and forms the basis of many modern proposals for high-frequency gravitational wave detection. This effect can be understood from the Maxwell–Einstein action by considering electromagnetic fields propagating in a weakly curved spacetime. We write the spacetime metric as a small perturbation around flat space,

$$g_{\mu\nu} = \eta_{\mu\nu} + \gamma_{\mu\nu}, \quad |\gamma_{\mu\nu}| \ll 1,$$

where $\gamma_{\mu\nu}$ represents the gravitational perturbation. To leading order in $\gamma_{\mu\nu}$, the interaction between the gravitational field and any field in nature is

$$\mathcal{H}_{\text{int}} = \frac{1}{2} \gamma_{\mu\nu} T^{\mu\nu}, \quad (5.58)$$

where $T^{\mu\nu}$ is the energy–momentum tensor of a generic field. For the electromagnetic field, this interaction Hamiltonian density can be written explicitly as

$$\mathcal{H}_{\text{int}} = -\frac{1}{2} \eta^{\lambda\sigma} \left(\gamma^{\mu\nu} - \frac{1}{2} \gamma \eta^{\mu\nu} \right) F_{\mu\lambda} F_{\nu\sigma}, \quad (5.59)$$

where $F_{\mu\nu}$ is the electromagnetic field-strength tensor and $\gamma \equiv \gamma^\mu{}_\mu$ is the trace of the metric perturbation. Note here we adopt natural units and set $c = \hbar = \epsilon_0 = 1$. The gravitational interaction Eq. (5.59) reveals how spacetime perturbations directly influence electromagnetic dynamics, opening a channel for graviton–photon conversion in a background field. The transition amplitude from an initial state $|i\rangle$ to a different final state $|f\rangle$ is given by the S-matrix element

$$\mathcal{A}_{fi} = \langle f | T \exp \left[-i \int d^4x \mathcal{H}_{\text{int}} \right] | i \rangle, \quad (5.60)$$

where T is the time-ordering operator.

Photon regeneration is a leading approach to probe HFGWs, which is based on this mechanism [196]. In such experiments, GWs traverse a photon-shielded cavity permeated by a strong magnetic field, allowing for resonant graviton-to-photon conversion. Consider a cylindrical electromagnetic cavity of length L and cross-sectional area A . We assume that the cavity walls are made of a perfect conductor. A uniform, static magnetic field is turned on inside the cavity, oriented along the \hat{z} direction, i.e.

$$\mathbf{B}(t, \mathbf{x}) = B_0 \hat{z}. \quad (5.61)$$

At this stage, it is necessary to fix the gauge. The electromagnetic fields measured in the laboratory are most naturally described in the Detector Proper (DP) frame, i.e., the local inertial frame in which the detector is in free fall. By contrast, theoretical descriptions of gravitational waves often employ the TT gauge, in which freely falling test masses remain at fixed coordinate positions while the effect of the gravitational wave is entirely encoded in oscillations of the metric. In this work, we adopt the TT gauge, defined by $h_{00} = h_{0i} = \partial_i h_{ij} = 0$, where $i, j = 1, 2, 3$. We further assume that the background magnetic field \mathbf{B}_0 is static in the TT frame. Although, in general, the transformation between the DP and TT frames in the presence of gravitational waves requires careful treatment, this approximation is well justified in the high-frequency regime $\omega L \gg v_s$ [197]. Here v_s denotes the sound velocity in the detector material, which is typically small, $v_s \lesssim 10^{-4}$.

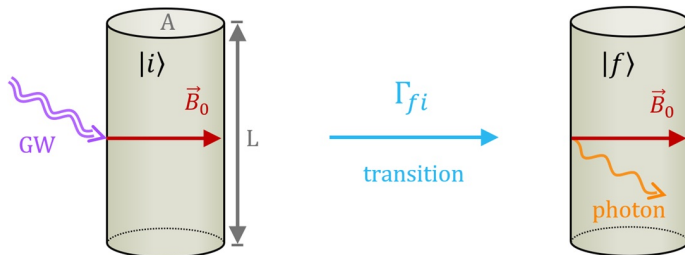


Figure 34: Illustration of a resonant cavity prepared in the electromagnetic state $|i\rangle$, which transitions to $|f\rangle$ as a passing gravitational wave induces graviton–photon conversion in a strong magnetic field.

We begin by considering the interaction of the cavity with an unpolarized, monochromatic gravitational wave of frequency ω , propagating in the direction $\hat{\mathbf{q}}$ (with $\mathbf{q} = \omega \hat{\mathbf{q}}$) as

$$h_{ij}(t, \mathbf{x}) = \sum_{\sigma} e_{ij}^{\sigma}(\hat{\mathbf{q}}) \hat{h}_{\omega} e^{iqx} + h.c., \quad (5.62)$$

the interaction Hamiltonian density can be written as

$$\hat{\mathcal{H}}_{\text{int}} = -B_0 \sin \theta_{\mathbf{q}} \sum_{\sigma} \delta \hat{B}_i(x) e_i^{\sigma}(\hat{\mathbf{q}}) \hat{h}_{\omega} e^{iqx}, \quad (5.63)$$

where $\delta\hat{B}_i(x)$ denotes the magnetic-field operator associated with fluctuations of the electromagnetic field, and

$$e_j^\pm(\hat{\mathbf{q}}) = \frac{1}{\sqrt{2}}(\cos\theta_{\mathbf{q}}\cos\phi_{\mathbf{q}} \mp i\sin\phi_{\mathbf{q}}, \cos\theta_{\mathbf{q}}\sin\phi_{\mathbf{q}} \pm i\cos\phi_{\mathbf{q}}, -\sin\theta_{\mathbf{q}}), \quad (5.64)$$

in cartesian coordinate. A cosmological stochastic background of unpolarized gravitational waves can be modeled as a superposition of plane waves with different frequencies and propagation directions as

$$h_{ij}(x) = \sum_{\sigma=\pm} \int d\ln\omega e_{ij}^\sigma(\hat{\mathbf{q}}) \int \frac{d^2\hat{\mathbf{q}}}{2\pi} \hat{h}_\omega e^{i\mathbf{q}\mathbf{x}} + h.c., \quad (5.65)$$

where $\mathbf{q} = \omega\hat{\mathbf{q}}$, h_ω is the mode function, and $\langle h_{ij}(t, \mathbf{x})h_{ij}(t, \mathbf{x}) \rangle = 2 \int d\ln\omega |h_\omega|^2$. In this stochastic setting, the interaction Hamiltonian is obtained by superposing the monochromatic contributions Eq. (5.63) over all frequencies and directions, with the cavity response effectively integrating over the accessible bandwidth.

Let us focus on electromagnetic transitions occurring inside the cavity, of the form

$$|i\rangle \longmapsto |f\rangle = \hat{b}_\omega^\dagger |i\rangle. \quad (5.66)$$

where \hat{b}_ω^\dagger denotes the creation operator of a photon with frequency ω . More precisely, we consider transitions in which a single photon is created within the cavity, thereby increasing the occupation number of the mode at frequency ω by one. The transition rate for the process $|i\rangle \rightarrow |f\rangle$, evaluated to first order in perturbation theory with respect to the GW amplitude h_ω , is given by

$$\Gamma_{fi} = \lim_{T \rightarrow \infty} \frac{1}{T} \left| \int d^4x \langle i | \hat{b}_\omega \mathcal{H}_{\text{int}}(x) | i \rangle \right|^2. \quad (5.67)$$

To proceed further and evaluate this expression explicitly, it is now necessary to specify the form of the initial state $|i\rangle$. The current active Photon regeneration experiments are OSQAR [189] and ALPS [190] at optical frequencies, and CAST [191] at X-ray frequencies. In addition, BabyIAXO and IAXO [192, 193] are under development, and JURA [194] proposed. All of these experiments are based on assuming initial vacuum state inside the cavity, i.e. $|i\rangle = |0\rangle$. Recently, a qualitatively new approach has been put forward under the name QuGrav [49]. This proposal exploits highly occupied n -photon states (qumodes) inside the cavity, allowing the graviton-induced transition rate to be parametrically enhanced by Bose–Einstein statistics. By coherently populating the cavity with a large number of photons, the conversion process benefits from stimulated emission, leading to a substantial enhancement relative to vacuum-based schemes. These experiments detect the photon count rate Γ within an energy band $\Delta f = (f_f - f_i)$, with a single photon detection efficiency ε , and over a cross-sectional area A . The background noise is quantified in terms of the dark count rate in that frequency bin, i.e., $\Gamma_D(f)$. It is the rate at which the detector falsely registers a photon even when no real photon is present. In Table 5 we summarized these experiments and proposals.

	f [Hz]	B_0 [T]	L [m]	A [m ²]	Γ_D [mHz]	ε	Cavity state	Ref.
OSQAR II	10^{15}	9	14.3	5×10^{-4}	1.14	0.9	vacuum $ 0\rangle$	[189]
ALPS II	10^{15}	5.3	106	10^{-3}	10^{-3}	0.75		[190]
<i>JURA</i>	10^{15}	13	960	8×10^{-3}	10^{-6}	1		[194]
CAST	10^{18}	9	9.26	2.9×10^{-3}	0.15	0.7		[191]
IAXO	10^{18}	2.5	20	3.08	0.1	1		[192, 193]
<i>QuGrav</i>	10^{10}	10	1	1	10^{-3}	1	Qumode $ n\rangle$	[49]

Table 5: Experimental parameters of photon-regeneration setups. All experiments assume a vacuum cavity state $|0\rangle$ except *QuGrav*, which considers a general Fock state $|n\rangle$. Here $\Gamma_D(f)$ is the dark count rate in a frequency bin of width Δf , and ε is the single-photon detection efficiency. Italicized entries indicate proposals.

From Qumodes to QuGrav



In the context of quantum information science, qubits constitute the canonical building blocks for storing and processing quantum information, encoding logical states in arbitrary superpositions of the basis states $|0\rangle$ and $|1\rangle$. While this abstraction underlies much of quantum computation, many advanced applications benefit from moving beyond strictly two-level systems. Within this broader framework, quantum harmonic oscillators, commonly referred to as qumodes, provide a natural extension of the qubit paradigm. By replacing or supplementing qubits with bosonic modes, qumodes offer a countably infinite-dimensional Hilbert space spanned by Fock states $|n\rangle$, with $n = 0, 1, 2, \dots$ [198–200]. This expanded state space enables richer encoding strategies and greater flexibility in the manipulation of quantum information, positioning qumodes as a powerful platform for continuous-variable quantum computation and cavity-based quantum technologies.

Recent technological breakthroughs have significantly expanded our ability to manipulate and measure complex quantum states of light. In particular, experimental platforms have begun to realize true n -photon qumodes with high fidelity and control [201, 202], enabling exploration of rich, high-dimensional Hilbert spaces beyond the qubit paradigm. A key milestone in this direction is the demonstration of photon-number-resolving measurements capable of distinguishing photon counts up to $n = 100$ [203], far exceeding the few-photon regime of traditional detectors.

Building on these developments, Kharzeev, Shalamberidze, and the present author

highlighted the transformative potential of this major advance in quantum measurement capability for the detection of HFGWs [49]. In particular, they proposed initializing the cavity in an n -photon Fock state rather than the vacuum, demonstrating that for large occupation numbers, $n \sim 10^2$, the sensitivity of photon-regeneration cavities can be enhanced by up to two orders of magnitude. More precisely, given that $|\langle n+1 | b^\dagger | n \rangle|^2 \propto (n+1)$, we have $\Gamma_{fi} \propto (n+1)$. This ambitious proposal was termed QuGrav, reflecting its quantum-enhanced approach to gravitational wave detection.

Following the QuGrav proposal, we consider an n -photon Fock state as the initial state of the cavity in order to explore genuine Bose enhancements associated with finite photon occupation. The formalism, however, remains completely general: by setting $n = 0$, one straightforwardly recovers the standard results corresponding to vacuum-initialized cavities. As an initial configuration, we consider an n -photon state at a single resonant frequency ω ,

$$|i\rangle = |Q_n\rangle = |n(\omega)\rangle_\gamma, \quad (5.68)$$

where $|n(\omega)\rangle_\gamma = (b_\omega^\dagger)^n |0\rangle_\gamma$. Now using the above initial state in Eq. (5.67), and considering a monochromatic gravitational wave with the same frequency in Eq. (5.63), we find the transition rate to $|f\rangle = |Q_{n+1}\rangle$ as

$$\Gamma_{fi} = 2(n+1) Q V B_0^2 h_{\omega_g}^2 \sin^2 \theta_q, \quad (5.69)$$

where Q is the quality factor of the cavity. Remarkably, due to Bose–Einstein statistics, once the frequency of the GW matches the frequency of the n -photon mode inside the cavity, the probability of graviton-to-photon conversion is enhanced by a factor of $n+1$. This process is the EM analogue to the stimulated absorption of gravitons in the massive quantum acoustic resonators, with the process being most effective at frequencies that match the resonator’s natural frequency [48].

To complement this minimal setup and to enhance sensitivity to the more challenging gravitational wave background, we now introduce a more elaborate qumode configuration that illustrates the theoretical reach and long-term potential of this approach for broadband detection. Specifically, we consider a multimode qumode state in which each resonant cavity mode is prepared in an n -photon Fock state, with mode frequencies given by $\omega_l = \pi l/L$, namely

$$\overline{|Q_n\rangle} = \bigotimes_{l=1}^{\lfloor 2\Delta f L/c \rfloor} |n(\omega_l)\rangle_\gamma. \quad (5.70)$$

Here $|n(\omega_l)\rangle_\gamma = (b_{\omega_l}^\dagger)^n |0\rangle_\gamma$, and $\lfloor 2\Delta f L/c \rfloor$ denotes the number of resonant modes supported by the cavity within the finite frequency bandwidth Δf (with $f = \omega/2\pi$).

Considering the stochastic gravitational wave background described in Eq. (5.65), and assuming for simplicity that the spectrum is approximately flat across this frequency interval, the total transition rate is obtained by summing the contributions from all resonant

modes, as

$$\Gamma_{\text{tot}} = 2(n+1)\Delta f L V B_0^2 h_\omega^2 \sin^2 \theta_{\mathbf{q}}. \quad (5.71)$$

Here Δf characterizes the effective detection bandwidth of the cavity. While a bright coherent drive also enhances the generation rate by the factor $n+1$, it simultaneously introduces amplitude and phase noise. For a quantitative comparison see [49].

For completeness, let us also consider a single graviton propagating in direction $\hat{\mathbf{q}}$ with frequency ω_g , i.e. $|1_{\omega_g}\rangle_g$, as

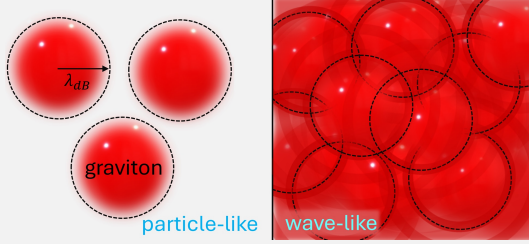
$$h_{ij}(t, \mathbf{x}) = \sum_{\sigma=\pm} e_{ij}^\sigma(\hat{\mathbf{q}}) h_{\omega_g}^\sigma \hat{a}_{\omega_g, \sigma} e^{-i\omega_g t + i\mathbf{q}\cdot\mathbf{x}} + h.c., \quad (5.72)$$

where $\hat{a}_{\omega, \sigma}^\dagger$ and $\hat{a}_{\omega, \sigma}$ are the graviton creation and annihilation operators, $[\hat{a}_{\omega, \sigma}, \hat{a}_{\omega', \sigma'}^\dagger] = \delta_{\sigma\sigma'}\delta(\omega - \omega')$. In this case, we set the initial and final states as

$$|i\rangle = |Q_n\rangle |1_\omega\rangle_g, \quad |f\rangle = \hat{b}_\omega^\dagger |Q_n\rangle |0\rangle_g, \quad (5.73)$$

which is the conversion of a single graviton to a new photon inside cavity. The transition rate in this case is equal to Eq. (5.69).

Single Gravitons



Modern detector architectures can detect single photons and even count them up to $n = 100$ [201, 202], but building a detector sensitive to single gravitons remains an extraordinary challenge. In fact, Dyson [204], and independently Rothman & Boughn [205], have argued that such detection is fundamentally impossible within certain experimental architectures, while remaining feasible in others. Recently, this question has been revisited in light of recent technological advances [48, 206].

If gravity is quantized in the same manner as the other fundamental interactions, the number of gravitons contained within a single de Broglie volume is

$$N_{\text{grav}} = n_{\text{grav}} \lambda_{\text{dB}}^3 = \frac{\pi h_\omega^2 M_{\text{Pl}}^2}{2f^2}, \quad (5.74)$$

where $\lambda_{\text{dB}} = f^{-1}$. As an example, a signal of LIGO detection with $h_\omega \sim 10^{-25}$ at $f \sim 10^2$ Hz, includes $N_{\text{grav}} \sim 10^{29}$ gravitons. Requiring less than a graviton per de Broglie volume, we arrive at

$$h_\omega \leq 2 \times 10^{-31} \left(\frac{f}{10^3 \text{ GHz}} \right), \quad (5.75)$$

where below that limit, the gravitational field is more accurately described as a highly dilute graviton gas rather than a classical gravitational wave.

Naively, one might expect that observing a gravitational wave with an amplitude below this particle-like threshold would amount to the detection of a single graviton. However, establishing the genuinely quantum nature of gravitational radiation requires measurements that are far more demanding than the mere detection of individual gravitons. In QED, the photoelectric effect alone does not suffice to establish the photon as a quantum particle, since it probes only discrete energy exchange. Definitive evidence requires a scattering process, such as Compton scattering, that demonstrates momentum transfer and particle, like kinematics. By analogy, proposals for single-graviton detection must go beyond quantized energy absorption and instead identify processes that reveal graviton-mediated exchange or quantum gravitational states. To obtain a measurement that unambiguously discriminates between classical and quantum descriptions, two major challenges must be addressed: the generation of genuinely nonclassical gravitational radiation, such as squeezed or entangled states, and its subsequent detection with a gravitational sensor operating at high efficiency [206].

We are now in a position to derive upper limits on the dimensionless gravitational wave characteristic strain, $h(f)$, using the parameters of current cavity experiments and proposed setups employing Qumode technology. For each configuration, the sensitivity can be quantified through the signal-to-noise ratio (SNR), obtained by requiring that the effective gravitationally induced transition rate satisfy

$$\varepsilon \Gamma_{fi} > \Gamma_D. \quad (5.76)$$

More precisely, for a gravitational wave signal to be detectable, the rate of real photon production via gravitational transitions must exceed the detector's dark count rate, which accounts for false detection events. For resonant detectors with narrow bandwidth sensitivity, a monochromatic gravitational field, or a GW background with a sharply peaked spectrum, we find

$$h_{\text{noise}}(f) \approx \frac{1.4 \times 10^{-27}}{\sqrt{n+1}} \left(\frac{1 \text{ m}}{L} \right) \left(\frac{10 \text{ T}}{B_0} \right) \sqrt{\left(\frac{1 \text{ m}^2}{A} \right) \left(\frac{10^5}{\mathcal{F}} \right)} \sqrt{\frac{1}{\varepsilon} \left(\frac{\Gamma_D}{1 \mu\text{Hz}} \right) \left(\frac{1 \text{ GHz}}{f} \right)}. \quad (5.77)$$

For the broadband case, using the theoretical benchmark Qumode state Eq. (5.70) with Eq. (5.71) for detectors, we have

$$h_{\text{noise}}(f) \approx \frac{4.5 \times 10^{-25}}{\sqrt{(n+1)}} \left(\frac{1 \text{ m}}{L} \right) \left(\frac{10 \text{ T}}{B_0} \right) \sqrt{\left(\frac{1 \text{ GHz}}{\Delta f} \right)} \sqrt{\frac{1}{\varepsilon} \left(\frac{\Gamma_D}{1 \mu\text{Hz}} \right) \left(\frac{1 \text{ m}^2}{A} \right)}. \quad (5.78)$$

The performance of a given detector operating in the Qumode configuration can be directly contrasted with that of its standard single-photon counterpart. In this case, the noise-

equivalent gravitational wave strains satisfy

$$\frac{h_{\text{noise}}^{\text{single}}}{h_{\text{noise}}^{\text{Qu}}} = (n + 1)^{-\frac{1}{2}}, \quad (5.79)$$

which demonstrates that the Qumode implementation achieves a parametric reduction in the effective strain noise as the photon occupation number n increases.

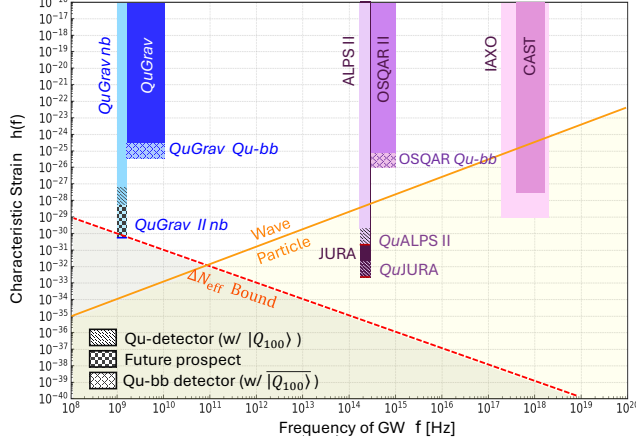


Figure 35: Strain sensitivity of photon-regeneration-based HFGW detectors. The region below the orange curve corresponds to gravitational fields that exhibit particle-like behavior, i.e., are describable in terms of gravitons. The dashed gray curve indicates the cosmological constraint from ΔN_{eff} . Hatched regions show the projected sensitivity gains of existing experiments and proposed setups employing a 100-photon Qumode ($|Q_{100}\rangle$, see Eq. (5.68)) within the cavity. The checkered (black–blue) region represents additional improvements achievable through near-term advances in cavity technology. Finally, the crossed regions illustrate the enhanced broadband sensitivity attainable with the futuristic broadband 100-photon Qumode $|Q_{100}\rangle$ introduced in Eq. (5.70). Image credit: [49].

In Fig. 35, we present the strain sensitivity of photon-regeneration-based HFGW detectors, both in their conventional configuration and with enhancements provided by qumode technology. Remarkably, at optical frequencies, the implementation of a 100-photon qumode enables ALPS II to probe well below the single-graviton threshold, crossing the wave–particle boundary. At microwave frequencies, the same approach has the potential to reach sensitivities surpassing the Big Bang Nucleosynthesis (BBN) bound, opening a new window on cosmologically motivated high-frequency gravitational wave signals.

6 Physical Mechanisms Driving Gravitational Radiation

As discussed earlier, gravitational waves arise as tensor perturbations of the spacetime metric, satisfying the linearized Einstein equation in the TT gauge. Their evolution is governed by

$$\square \gamma_{ij} = 16\pi G \Pi_{ij}^{\text{TT}}, \quad (6.1)$$

where Π_{ij}^{TT} denotes the transverse–traceless component of the anisotropic stress tensor.²⁰ In Secs. 2 and 3, we examined the propagation of gravitational waves in asymptotically flat spacetimes, in which local astrophysical systems provide the anisotropic stresses appearing on the right-hand side of the equation above. As shown in Eq. (2.28), the transverse–traceless stress Π_{ij}^{TT} is directly related to the second time derivative of the mass quadrupole moment, establishing the familiar connection between gravitational wave generation and the non-spherical, accelerated motion of matter within such sources, schematically \ddot{Q}_{ij}/r . In contrast, in Sec. 4 we turned to cosmological backgrounds and focused on vacuum fluctuations for which the source term vanishes, $\Pi_{ij}^{\text{TT}} = 0$. The present section focuses on the various physical mechanisms capable of generating a nonzero Π_{ij}^{TT} and thus sourcing gravitational wave emission in both astrophysical and cosmological settings.

6.1 Astrophysical Sources

A wide variety of astrophysical objects and dynamical phenomena can generate gravitational waves, each imprinting characteristic spectral features and signal morphologies. These sources span an enormous range of masses, environments, and timescales—from compact binaries to supernovae, isolated neutron stars, and stochastic backgrounds. The main classes of gravitational wave sources are naturally grouped by the duration of the signals they produce. Short-duration events include compact binary inspirals, mergers, and burst-like transients, whereas long-duration signals arise from continuous-wave emitters and the stochastic gravitational wave background. Together, these categories capture the broad spectrum of astrophysical processes capable of radiating gravitational waves across cosmic time. Fig. 36 illustrates the main categories of gravitational wave sources and their characteristic signal durations. In the following, we provide a brief summary of each.

6.1.1 Compact binary coalescences

Compact binary coalescences (CBCs) are the most mature and well-understood astrophysical sources of gravitational waves. Binary neutron stars ($M \sim 1\text{--}2M_\odot$), stellar-mass black holes ($M \sim 10\text{--}100M_\odot$), and mixed neutron-star–black-hole systems lose orbital energy through quadrupole emission and ultimately merge in the strong-field regime. Their signals follow the characteristic inspiral–merger–ringdown sequence and populate the $\sim 10\text{--}10^3\text{Hz}$ band of ground-based interferometers. Neutron-star mergers peak at a few hundred hertz, while stellar-mass black-hole binaries radiate at tens to hundreds of hertz depending on total mass. The first LIGO–Virgo detections [4, 213] firmly established CBCs as the dominant sources (see Fig. 30), enabling detailed population studies and stringent tests of general relativity [214].

At lower frequencies, supermassive black-hole (SMBH) binaries represent the most luminous gravitational wave emitters known. Formed through hierarchical galaxy merg-

²⁰Beyond Einstein general relativity, a wide class of modified-gravity theories can alter the propagation of tensor modes as $\ddot{\gamma}_{ij} + (3H + \delta_1)\dot{\gamma}_{ij} + \left(c_T^2 \frac{k^2}{a^2} + m_T^2 + \delta_2\right)\gamma_{ij} = 16\pi G_{\text{eff}} \Pi_{ij}^{\text{TT}}$, where c_T is the tensor propagation speed, m_T an effective graviton mass, and δ_1, δ_2 encode possible modifications to friction and dispersion arising in modified gravity (e.g., [51, 53, 207–211]). These modified-gravity frameworks, however, lies beyond the scope of the present review and we refer the interested reader to [212].

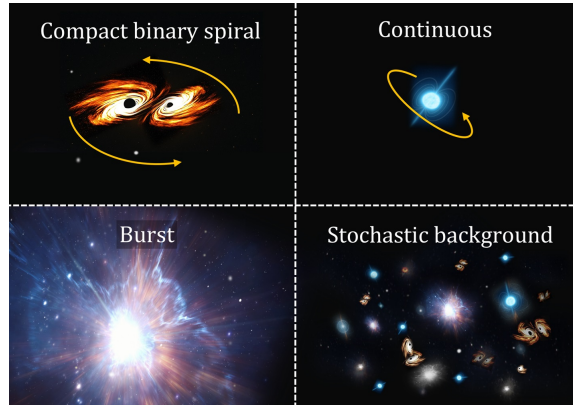


Figure 36: Illustration of the main astrophysical classes of gravitational wave sources, grouped by the duration of the signals they produce. Short-duration events (left) include compact binary inspirals and burst-like transients, while long-duration signals (right) arise from continuous-wave emitters and the stochastic gravitational wave background, together representing the broad range of astrophysical processes that generate gravitational waves.

ers [215, 216], they radiate across the millihertz to nanohertz spectrum. Their mergers fall within the 10^{-4} – 10^{-1} Hz band accessible to LISA [217], providing a prime target for space-based detectors. LISA will also observe extreme mass-ratio inspirals (EMRIs), the gradual inspiral of a stellar-mass compact object into a 10^5 – $10^7 M_{\odot}$ SMBH. EMRIs emit in the 10^{-4} –1 Hz range and encode high-fidelity information about the spacetime geometry near massive black holes, offering precision tests of the Kerr hypothesis [218, 219]. In addition, LISA will detect ultra-compact Galactic binaries, early inspirals of stellar-mass black-hole binaries, and potentially signals of primordial or exotic origin [220]. The earliest inspiral stages of massive binaries produce nanohertz gravitational waves (10^{-9} – 10^{-7} Hz), which lie in the domain of pulsar timing arrays (PTAs) [221]. These systems are expected to dominate the low-frequency gravitational wave sky and offer insight into galaxy growth, nuclear stellar dynamics, and black-hole coevolution [222]. As a window to fundamental physics, gravitational wave signals from compact binary coalescences may provide an ideal testing ground for potential deviations from classical horizon dynamics. In this context, J. Abedi, H. Dykaar, and N. Afshordi proposed that GW echoes could serve as observational signatures of new physics near black-hole horizons. In their framework, a partially reflective quantum structure replacing the classical horizon would generate a sequence of delayed post-merger echoes potentially detectable by LIGO/Virgo [223–225].

6.1.2 Isolated neutron stars

Isolated neutron stars furnish an additional class of promising sources through long-lived, nearly monochromatic continuous-wave emission [226, 227]. Such radiation, typically in the $\sim 10^2$ – 10^3 Hz range and set by the stellar rotation rate and deformation, remains undetected but is actively sought by all-sky searches and targeted pulsar analyses. Achieving astrophysically significant sensitivities would provide valuable constraints on neutron-star

microphysics, crustal rigidity, and internal magnetic-field structure. Neutron stars can serve as natural astrophysical laboratories to search for new physics [228–233].

6.1.3 Transient burst sources

Highly dynamical and asymmetric stellar explosions also contribute to the gravitational wave landscape. Core-collapse supernovae produce short-duration, broadband bursts through turbulent convection, proto–neutron-star oscillations, rotation-driven instabilities, and standing accretion shock instabilities. Their gravitational wave spectra typically span $\sim 10^2$ – 10^3 Hz, reflecting the characteristic dynamical timescales of proto–neutron-star cores. Although modeling remains challenging due to the nonlinear interplay of multidimensional hydrodynamics, neutrino transport, and magnetic fields, simulations indicate that next-generation detectors could observe signals from supernovae in the Milky Way or nearby galaxies [234, 235]. Additional transient phenomena, such as magnetar flares and gamma-ray-burst engines, may likewise produce gravitational radiation through violent magnetic or accretion-driven processes [236].

6.1.4 Astrophysical Contributions to the Stochastic GW Background

Astrophysical sources, most notably compact-object mergers, give rise to the individually resolved GW events detected by current observatories. Taken collectively, these same populations also generate a stochastic gravitational wave background, produced by the superposition of numerous weak or distant events across cosmic history, each individually undetectable yet together forming a persistent, measurable signal. PTAs uniquely access the nanohertz band, where the background from the cosmic population of slowly inspiraling SMBH binaries is expected to dominate [237]. Recent observations by NANOGrav, the EPTA, the PPTA, and the IPTA provide compelling evidence for a spatially correlated common-spectrum process consistent with the emergence of this background [24, 238, 239] (see Fig. 28).

At higher frequencies, space-based laser interferometers such as LISA [29] will probe the millihertz band, where the astrophysical stochastic background is expected to be dominated by compact binaries in early inspiral, including galactic white-dwarf binaries and massive black-hole systems. At still higher frequencies, next-generation ground-based detectors such as the Einstein Telescope [240] will access the audio band with unprecedented sensitivity, enabling precise measurements of both individually resolved mergers and the astrophysical stochastic background generated by stellar-mass compact binaries across cosmological distances. Together, PTAs, LISA, and the Einstein Telescope provide complementary coverage of the gravitational-wave spectrum, enabling a truly multi-band characterization of the astrophysical gravitational-wave background.

6.2 Cosmological Sources

A rich variety of processes in the early Universe can generate stochastic backgrounds of gravitational waves, offering a unique window into physics far beyond the reach of terrestrial experiments. Among the most extensively studied cosmological sources are inflation/reheating, first-order phase transitions, topological defects, primordial black holes,

scalar-induced tensor modes, and magnetohydrodynamical phenomena in the radiation-era plasma. Each mechanism imprints characteristic spectral features that encode fundamental information about high-energy symmetries, inflationary dynamics, or hidden sectors. For comprehensive overviews, see for example the recent Einstein telescope Science Books [32, 240], as well as the LISA Cosmology Reports [6, 29]. In the following, we discuss the main classes of cosmological GW sources and the physics that underlies their distinctive signatures.

6.2.1 Inflation and Reheating

In addition to the standard vacuum tensor modes from slow-roll inflation discussed in Sec. 4.4, signals associated with spectator fields, i.e. additional scalar or gauge fields present during inflation but not driving it, may source a stochastic gravitational wave background with distinctive spectral features. For a recent comprehensive review of inflationary scenarios capable of enhancing the stochastic GWB to amplitudes observable by LISA, see [241]. Following inflation, similar dynamics can occur during reheating. In scenarios of gauge preheating, the coherent oscillations of the inflaton transfer energy efficiently into Abelian or non-Abelian gauge sectors, sourcing gravitational waves through highly non-linear, anisotropic field configurations [242–245]. The resulting GW backgrounds can be sufficiently large that the requirement of avoiding excess radiation energy density at BBN imposes important constraints on the viable parameter space of such models [246–248].

Inflation also sources gravitational waves indirectly through scalar fluctuations. Large or resonantly enhanced curvature perturbations can generate second-order tensor modes already during inflation or shortly after horizon re-entry, producing scalar-induced contributions with sharply peaked spectra. The underlying mechanism was first established in the seminal second-order calculations of [249, 250], and later applied to scenarios featuring large small-scale scalar enhancements, such as those associated with primordial black-hole production [251, 252]. Resonant or non-adiabatic dynamics during inflation can further amplify scalar fluctuations and source tensor modes directly, as shown in models of particle production and inflationary resonance e.g. [253, 254]. Together, these mechanisms highlight inflation and reheating as fertile grounds for generating non-vacuum gravitational waves with characteristic signatures—sharp spectral features, non-Gaussianity, and potential chirality—not shared by the standard slow-roll vacuum tensor background. For comprehensive reviews of scalar-induced gravitational waves, see [5, 255, 256].

Gauge Fields in Inflation and GWs

Gauge fields are a foundational component of the SM and of nearly all well-motivated extensions of high-energy physics. Because cosmic inflation probes energy scales far beyond those accessible to terrestrial experiments, it is natural to view the early Universe as a particle collider capable of revealing new interactions—an idea formalized in the framework of the Cosmological Collider [143, 146]. This perspective motivates the question of whether gauge fields played a dynamical role during inflation and, if so, whether they left observable imprints in primordial correlators. Axion-like fields, protected by an approximate shift symmetry, provide compelling inflaton candidates and couple universally to gauge sectors

through the CP-violating interaction $\phi F_{\mu\nu} \tilde{F}^{\mu\nu}$. Originally introduced in the context of the Peccei–Quinn mechanism [257–260] and later explored in cosmology [261, 262] and inflation [263–266], this coupling naturally mediates interactions between inflaton dynamics and gauge degrees of freedom. In addition, axions may be realized as composite states originating from confining gauge dynamics [267, 268]. Axions and axion-like particles play a central role in both cosmology and particle physics, and their theoretical foundations and detection prospects have been thoroughly reviewed in [269–275]. During inflation, the axion-gauge field interaction can lead to the exponential amplification of Abelian gauge-field fluctuations [276, 277]. Inflationary scenarios involving gauge fields therefore provide some of the earliest and most well-developed mechanisms for producing non-vacuum gravitational waves. These effects offer a rich arena for probing gauge sectors through primordial non-Gaussianity and gravitational-wave signatures [5, 278].

In 2011 it was shown in [279, 280] that non-Abelian gauge fields can contribute nontrivially to the dynamics of inflation while—unlike Abelian $U(1)$ background fields—preserving the observed cosmological isotropy within an $SU(2)$ subsector. In particular, the background gauge field can consistently acquire a homogeneous and isotropic vacuum expectation value of the form

$$\bar{A}_\mu(t) \equiv \bar{A}_\mu^a(t) T_a = \begin{cases} 0, & \mu = 0, \\ a(t) \psi(t) \delta_i^a T_a, & \mu = i, \end{cases} \quad (6.2)$$

where $\{T_a\}$ are the generators of the $SU(2)$ gauge algebra. This homogeneous and isotropic field configuration is possible due to the isomorphism between the $SU(2)$ gauge algebra and the spatial rotation algebra $SO(3)$, which allows gauge and spatial indices to be aligned (see Fig. 37). Perturbations of the gauge fields around this isotropic background contain an induced spin-2 mode that couples linearly to gravitational waves [279, 280]. In particular,

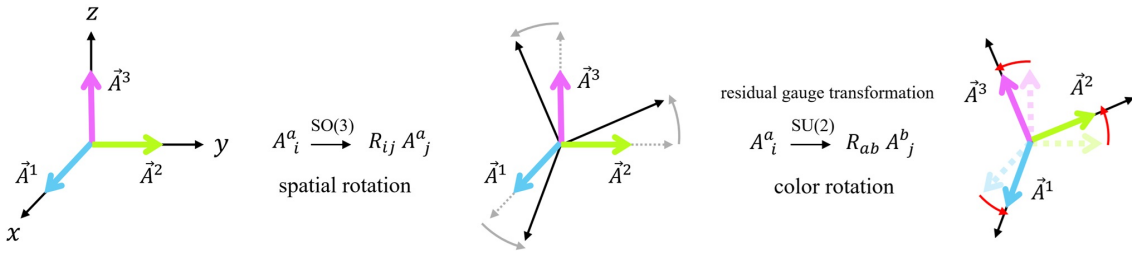


Figure 37: Coherent homogeneous $SU(2)$ background gauge field and the restoration of spatial isotropy. A homogeneous $SU(2)$ gauge-field configuration transforms as a vector under spatial rotations. At the same time, the $SU(2)$ gauge symmetry contains residual transformations with the same algebraic structure, reflecting the Lie-algebra isomorphism $\mathfrak{su}(2) \cong \mathfrak{so}(3)$. Thus, any spatial rotation can be compensated by an appropriate $SU(2)$ gauge transformation, corresponding to the diagonal subgroup of $SO(3)_{\text{rot}} \times SU(2)_{\text{gauge}}$. Since physical observables are gauge invariant, they depend only on this diagonal action and therefore remain fully rotationally symmetric.

the spatial gauge-field perturbations include a tensorial component of the form

$$\delta A_i^a, \ni, t_{ij}, \delta^{aj}, \quad (6.3)$$

which transforms as a spin-2 degree of freedom. A rigorous mathematical proof of the spin-2 nature of this induced tensor mode can be found in Appendix B.1 of [132]. This mode undergoes a brief phase of tachyonic instability near horizon crossing, leading to the formation of a chiral cloud of gauge-field tensor fluctuations localized around the cosmic horizon. Owing to its linear coupling to the metric tensor perturbations, this induced spin-2 mode acts as a chiral source for gravitational waves, corresponding to a nonvanishing transverse–traceless anisotropic stress, $\Pi_{ij}^{\text{TT}} \neq 0$. As a result, this coupling enables the efficient production of chiral, blue-tilted gravitational waves [128, 130–132, 281–284], accompanied by characteristic non-Gaussian tensor perturbations [285, 286] (see Fig. 38). Consequently, inflation in this class of models is intrinsically parity violating (see Fig. 39), with a pronounced asymmetry between left- and right-handed gravitational-wave modes imprinted at the level of primordial correlations.

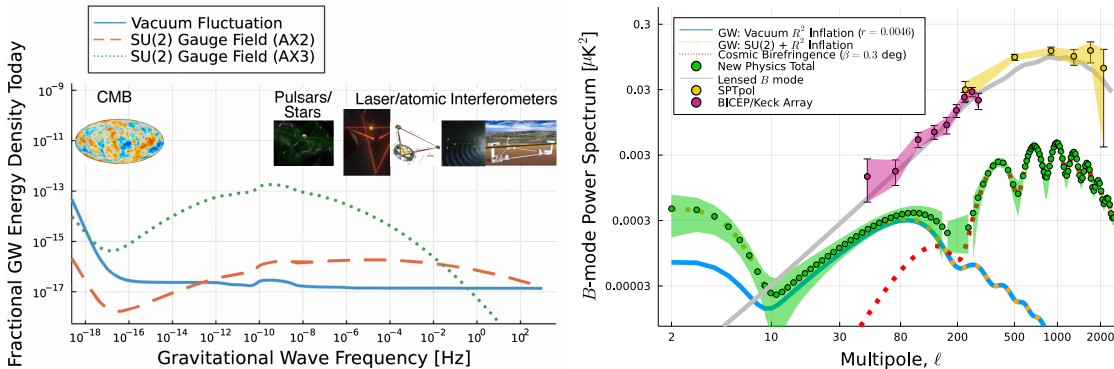


Figure 38: Characteristic imprints of SU(2)–axion inflation on the gravitational wave background and CMB B-mode polarization. Image credit: [5].

This framework admits several distinct realizations within inflationary model building, which have been explored extensively in the literature [14, 131, 280–282, 284, 287–295]. In most cases, the isotropic configuration corresponds to an attractor solution [296–299], except in scenarios involving Higgsed non-Abelian gauge fields with unequal masses for at least two gauge components [300]. Variants of this setup have also been applied in the context of warm inflation [301, 302] and have found further applications in dark-energy model building [303–307]. Beyond their distinctive tensor signatures, these models exhibit a rich phenomenology extending beyond standard scalar inflation, including the Schwinger effect during inflation [308–311], as well as mechanisms for baryogenesis and leptogenesis mediated by the chiral anomaly [293, 312, 313]. For broader context and a systematic classification of Abelian and non-Abelian mechanisms, we refer the reader to the comprehensive review [128], together with the recent perspectives presented in [5] and [241].

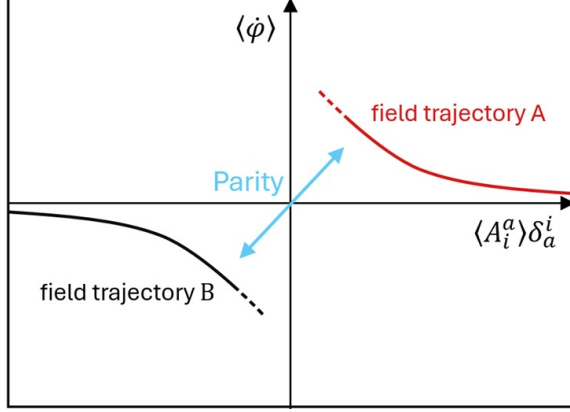


Figure 39: Schematic illustration of slow-roll field trajectories related by parity. In the axion–SU(2) gauge-field model, slow-roll solutions satisfy $\text{sign}(\dot{\phi}) = \text{sign}(A_i^a \delta_a^i)$, selecting one of the two parity-related branches.

Cosmic Chirality: Signatures of Broken Fundamental Symmetry in CMB, LSS, and GWs

Parity (P), defined as invariance under spatial inversion ($\mathbf{x} \rightarrow -\mathbf{x}$), is one of the fundamental discrete symmetries of nature. While parity is conserved by gravitational, electromagnetic, and strong interactions in the Standard Model of particle physics, it is known to be maximally violated by weak interactions, establishing P violation as a fundamental feature of particle physics. This fact motivates the possibility that new physics beyond the SM, may also violate parity. An open and profound question is therefore whether parity was ever an exact symmetry of the Universe at earlier stages of its evolution, or whether parity-violating interactions played a role throughout cosmic history. Cosmology provides a unique laboratory to address this question, offering observational access to physical processes across vastly different epochs. Parity violation in cosmology has consequently been explored across multiple epochs using CMB observations and LSS measurements, and more recently through proposed searches for stochastic GWBs.

Parity violation in the CMB can manifest as cosmic birefringence, a rotation of the linear polarization that induces nonvanishing TB and EB correlations. For decades, this effect was thought to be unobservable because it is degenerate with instrumental polarization angle miscalibration and is therefore removed by standard self-calibration procedures. A recent breakthrough realization by Minami & Komatsu [314] showed how this degeneracy can be broken using correlations with Galactic foreground emission, leading to the first statistically significant hint of a nonzero cosmic birefringence signal in *Planck* data. This result has revitalized efforts to probe fundamental parity-violating physics using the polarized sky. Subsequent studies using polarization data from *WMAP*, *Planck* (2018 and DR4), and the Atacama Cosmol-

ogy Telescope have progressively tightened constraints on cosmic birefringence, with some reporting evidence for a nonzero uniform rotation angle while emphasizing the critical role of instrumental systematics [314–317]. Parity violation may also originate during inflation, where chiral gravitational waves sourced by parity-violating interactions generate intrinsically parity-odd signatures in CMB polarization, most prominently at large angular scales in the B -mode spectrum through nonzero TB and EB correlations [318–321]. These low- ℓ B modes provide a unique probe of primordial parity violation, complementary to post-recombination birefringence. See [5] for a clear and comprehensive recent review.

In addition, parity-violating physics during inflation or phase transitions can produce circular polarization of gravitational waves, which can be detected by gravitational wave detector networks, providing an independent and complementary probe of parity violation beyond electromagnetic observations [321–326].

At late times, parity violation has further been investigated in LSS through parity-odd components of higher-order galaxy correlation functions. Recent work has proposed galaxy intrinsic alignment as an additional probe [327]. Measurements from BOSS and SDSS find yet no statistically significant evidence for such signals [328–330], while early results from DESI extend these tests with improved sensitivity [331]. Together, low- ℓ CMB B modes, birefringence measurements, gravitational wave backgrounds, and LSS correlations form a complementary framework for testing parity-violating physics across cosmic history.

6.2.2 Cosmological Phase Transitions and Hydrodynamical Sources

First-order cosmological phase transitions can act as powerful factories of gravitational waves: as bubbles of the true vacuum nucleate, expand, and collide, they generate tensor perturbations through the violent dynamics of bubble walls [332, 333]. In realistic transitions, however, most of the released vacuum energy is transferred to the surrounding plasma, making hydrodynamical processes—the acoustic waves generated by expanding bubbles and subsequent magnetohydrodynamic (MHD) turbulence—the dominant and longest-lasting GW sources [334–336]. The resulting spectra are typically broad and peaked, with characteristic frequencies set by the bubble size and transition temperature, making electroweak-scale transitions a prime target for space-based interferometers such as LISA [6] (see Fig. 40). Importantly, within the Standard Model the electroweak phase transition is a smooth crossover rather than first order, and therefore does not generate significant GW production. Therefore, detectable signals require extensions of the Standard Model capable of strengthening the transition. Many extensions involving additional scalar degrees of freedom, hidden sectors, or supersymmetric frameworks predict strongly first-order transitions capable of producing observable gravitational waves. Consequently, cosmological phase transitions offer a unique observational window into BSM physics at energy scales ranging from the electroweak regime up to grand-unified theories [337–341].

Primordial magnetic fields provide an additional MHD source of gravitational waves: their anisotropic stresses, together with the MHD turbulence and Alfvén waves they induce

in the radiation-era plasma, generate a stochastic background whose amplitude and spectral shape depend on the field strength, coherence scale, and helicity [342–344]. Such magnetic fields may themselves originate from early-Universe phase transitions or other high-energy processes, making them a natural complement to hydrodynamical GW sources. Modern quantitative treatments combine bubble dynamics, plasma interactions, and numerical simulations to model these signals more reliably [345, 346]. Comprehensive recent reviews of phase-transition and MHD-sourced gravitational waves, and their implications for particle physics and cosmology, can be found in Refs. [248, 347, 348].

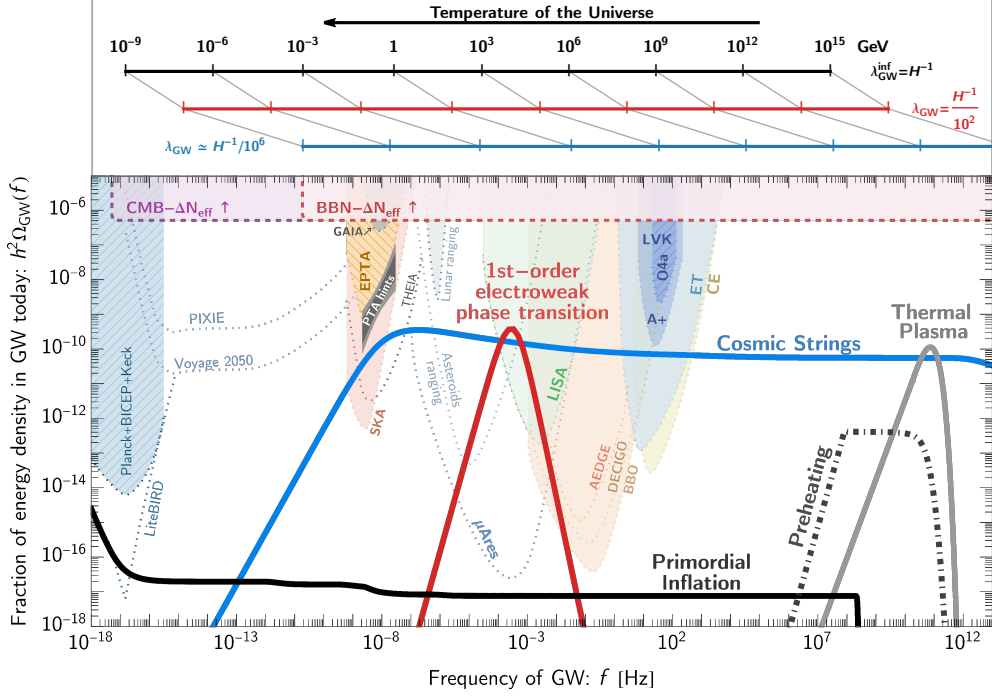


Figure 40: Sensitivity curves of current and future gravitational wave observatories across a broad frequency range, shown together with representative cosmological GW sources. The thick black curve denotes the nearly scale-invariant (vacuum) GW spectrum from inflation, while the blue and red curves represent GW backgrounds from cosmic strings and a first-order electroweak phase transition, respectively. The GAIA and THEIA curves are based on [27] assuming SNR = 10 with observation times of 10 and 20 years, respectively. The colored lines at the top of the figure indicate the present-day GW frequencies corresponding to the production time for different source sizes λ_{GW} (colors match those of the spectra). For illustration, the cosmic string spectrum is shown for $G\mu = 10^{-11}$ (μ is the energy per unit length of a string and G is Newton’s constant), and the first-order phase transition signal for $T_* = 150, \text{ GeV}$, $\beta/H_* = 20$, and $\alpha = 0.5$. Image credit: Peera Simakachorn and [349].

6.2.3 Topological Defects

Topological defects arise when a system with gauge (or global) symmetry undergoes spontaneous symmetry breaking during a phase transition. Let a theory have symmetry group G , acting on scalar fields Φ , with a symmetry-breaking potential $V(\Phi)$. When the vacuum expectation value $\langle\Phi\rangle$ selects a ground state, the symmetry is broken to a subgroup $H \subset G$. The degenerate vacua form the vacuum manifold $\mathcal{M} = G/H$, which is a coset space whose global topology determines the allowed defect structures. The topological defects correspond to topologically non-trivial mappings $\Phi : S^n \rightarrow \mathcal{M}$, where S^n is an n -sphere enclosing the defect in physical space. If this map is non-contractible, the configuration cannot be continuously deformed to the vacuum. The relevant homotopy group $\pi_n(\mathcal{M})$ therefore classifies the defect. As shown by Tom Kibble [350], causality in an expanding universe implies that regions separated by more than the horizon scale at a phase transition choose vacua independently. Mismatches between these choices generically produce defects whenever the topology of \mathcal{M} is nontrivial [351].

Defect type	Vacuum topology	Homotopy	Cosmology
Domain walls	Disconnected vacua	$\pi_0(\mathcal{M})$	Broken discrete symmetry
Strings	Loops in vacuum manifold S^1	$\pi_1(\mathcal{M})$	Cosmic strings
Monopoles	Non-contractible spheres S^2	$\pi_2(\mathcal{M})$	GUT magnetic monopoles
Textures	Higher-order winding S^3	$\pi_3(\mathcal{M})$	Global textures

Table 6: Cosmologically relevant topological defects from gauge symmetry breaking. Defects are classified by the homotopy groups of the vacuum manifold $\mathcal{M} = G/H$, a coset space determined by the symmetry-breaking pattern.

Topological defects can naturally arise during symmetry-breaking phase transitions in the early Universe, taking the form of domain walls, monopoles, cosmic strings, or textures depending on the topology of the vacuum manifold. Among these, cosmic strings are by far the most robust and observationally relevant gravitational wave sources. They may be produced in field-theoretic transitions or in a variety of beyond-the-Standard-Model scenarios. Early work by Vilenkin [352] and Brandenberger, Albrecht & Turok [353], together with later reviews of defect cosmology [354], place cosmic strings within the wider context of early-Universe physics. Once formed, cosmic strings rapidly organize into a long-lived scaling network that continuously produces string loops [350, 351]. These loops oscillate relativistically under their tension and lose energy predominantly through GW emission, as established in the foundational works of Vachaspati and Vilenkin [355] and Allen and Shellard [356].

GW production is enhanced at relativistic features on the loop—cusps, where segments briefly approach the speed of light, and kinks, which arise from intercommutation events. These features generate strong bursts whose superposition over cosmic history leads to a nearly scale-invariant stochastic background (see Fig. 40), with characteristic spectral breaks encoding the expansion history and loop-size distribution [357, 358]. Extensions such

as superconducting or current-carrying cosmic strings, originally proposed by Witten [359], further enrich the GW phenomenology by introducing current-induced energy-loss channels and modified loop dynamics, with detailed modern treatments presented in [360]. Several recent comprehensive reviews specifically address the gravitational wave phenomenology of cosmic-string networks [9, 94, 361–363]. Other topological defects can also source GWs. Global textures generate smooth, nearly scale-invariant tensor spectra, while monopole–string composite systems radiate during annihilation or collapse [364–367]. Domain walls, when present, undergo dynamical evolution that can drive powerful defect-induced phase transitions and corresponding GW signals [368]. Although typically more model-dependent than cosmic strings, such defects provide complementary probes of high-energy symmetry breaking.

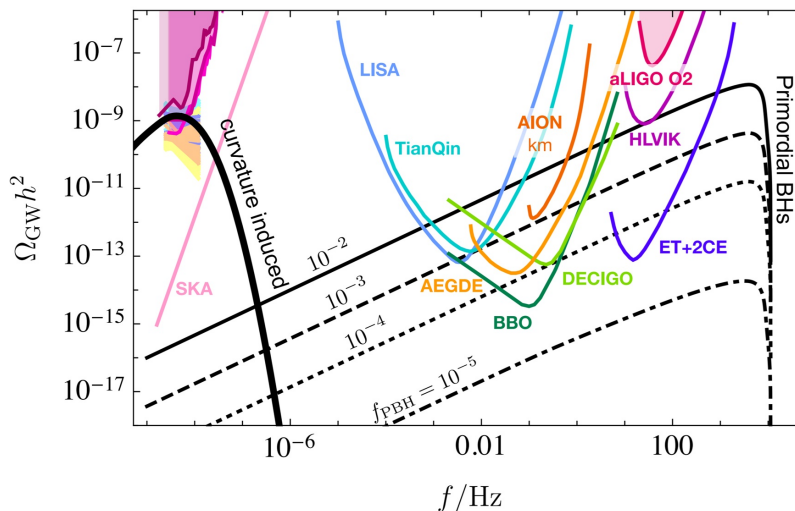


Figure 41: Comparison of detector sensitivities with GW spectra associated with primordial black hole PBH scenarios and scalar induced tensor modes. The thick black curve on the left shows the second-order curvature-induced GWs generated during PBH formation, while the thick black curve on the right shows the stochastic GW background from PBH binaries. Dashed black curves correspond to predicted backgrounds for different PBH abundance fractions. Image credit: Adapted from [369].

6.2.4 Primordial Black Holes and scalar-induced gravitational waves

Primordial black holes (PBHs) are black holes formed in the early Universe, typically from the collapse of large overdensities shortly after horizon re-entry, rather than from stellar evolution [370]. Their formation is most naturally described in terms of enhanced primordial curvature perturbations, which collapse if they exceed a critical threshold. The associated GW signatures arise through two main channels. First, PBHs can form binary systems whose inspirals and mergers generate a population of resolvable GW events and a stochastic background, potentially contributing to the binary black-hole signals observed by ground-based interferometers [371]. Second, the large scalar perturbations re-

quired for PBH formation inevitably source tensor perturbations at second order, leading to scalar-induced GWs with peaked spectra that can fall in the PTA, LISA or ground-based frequency bands [251]. This connects PBH dark-matter scenarios directly with GW observations. Scalar-induced gravitational waves (SIGWs) arise at second order in cosmological perturbation theory: large primordial curvature fluctuations, though not sourcing tensor modes at linear order, inevitably generate gravitational waves as they re-enter the horizon in the radiation era. This mechanism was first established in [249, 250] and later applied to scenarios with enhanced small-scale perturbations, such as those leading to primordial black-hole formation [251]. For the gravitational wave features in relation to the sensitivities of current probes, see Fig. 41. The resulting GW spectra are typically sharply peaked, with frequencies determined by the horizon scale at re-entry, making SIGWs a powerful probe of inflationary physics on scales far smaller than those constrained by the CMB. For comprehensive discussions of PBHs and their GW signatures, including end-to-end treatments of inflationary production, binary formation, and induced backgrounds, see recent reviews [255, 372, 373].

7 Summary

In this review, we present a pedagogical study of gravitational waves, integrating theory, phenomenology, and observation. Gravitational waves offer a powerful probe of high-energy BSM physics and a unique window into the unexplored frontiers of gravity and the early Universe. Unlike photons, which could only free-stream after the formation of the cosmic microwave background ($T = 1$ eV), and neutrinos, which decoupled at $T = 1$ MeV, gravitational waves have always propagated freely across cosmic history. As a result, once detected, they carry valuable and unique information about the Universe at energy scales far beyond those accessible by terrestrial particle colliders (see Fig. 15).

Spanning a gravitational wave rainbow with wavelengths ranging from the size of the observable Universe down to kilometer scales (10^{-17} - 10^4 Hz), these signals enable a truly multi-scale exploration of fundamental physics, providing insights impossible to obtain from any other messenger. Gravitational waves provide a unique probe of fundamental physics, connecting gravity and high-energy phenomena across multiple scales. We develop a coherent framework linking the mathematical foundations of gravitational radiation with the signals accessible to current and future detectors, aiming to bridge the gap between theoretical predictions and experimental measurements. Since gravitational waves are both generated and propagate through the Universe’s gravitational backgrounds, their description depends on the relevant spacetime geometry. On small scales (up to 100 Mpc), the expansion of the Universe is negligible, and asymptotically flat spacetimes accurately describe gravitational dynamics. On larger, cosmological scales, expansion becomes significant, and the FLRW geometry must be used. This distinction also reflects the nature of gravitational wave sources: deterministic astrophysical events produce coherent signals, whereas cosmological processes generate stochastic backgrounds, requiring a statistical treatment (see Fig. 3).

The review begins with the linearized theory of general relativity, deriving gravitational waves as solutions to the Einstein equations and analyzing their physical properties. Next,

we provide a more mathematically rigorous definition of gravitational waves by examining their geometrical nature through the Weyl tensor, including its principal null directions and Petrov classification. Within the Bondi–Sachs framework, this approach clarifies how gravitational waves propagate as true distortions of spacetime, demonstrating that they are genuine carriers of energy and angular momentum. By combining algebraic and geometrical perspectives, this framework establishes a solid theoretical foundation for interpreting observational data and connecting theory with experiment.

We then explore cosmological gravitational waves, tracing their evolution across different cosmic epochs and their generation during inflation, phase transitions, and other early-Universe processes. Building on this foundation, we survey the principal detection strategies across a broad range of frequencies, including cosmic microwave background measurements, pulsar timing arrays, ground- and space-based laser interferometers, and resonant cavity experiments. We also highlight several ongoing developments and proposed concepts that, in the near future, are expected to substantially enhance both the sensitivity and frequency reach of gravitational-wave observations. We then examine the physical mechanisms responsible for generating gravitational radiation, clearly distinguishing between astrophysical sources and cosmological origins.

The study of gravitational waves is a vibrant and rapidly advancing frontier, marked by open theoretical, numerical, and observational challenges and by rapid progress on multiple fronts. By integrating theory, phenomenology, and observation, this review emphasizes the extraordinary power of gravitational waves to probe the Universe across all scales, granting access to energy regimes and physical processes far beyond the reach of conventional experiments. We hope this work will guide and inspire both newcomers and experienced researchers as gravitational-wave physics continues to open a transformative window onto the cosmos.

Acknowledgments

First, I would like to express my gratitude to the Astronomy and Astrophysics Review for the invitation to write this article. I owe particular thanks to Eiichiro Komatsu, whose encouragement and intellectual guidance not only sparked my enduring interest in the subject, but also greatly deepened my understanding of it. I am also grateful to Robert Brandenberger, Sadra Jazayeri, Eiichiro Komatsu, and Geraldine Servant for their valuable feedback and thoughtful suggestions, which significantly improved the clarity of this work. I thank Peera Simakachorn for helpful discussion and also providing the plot shown in Fig. 40. I would further like to thank Dionysios Anninos, Daniel Baumann, Dmitri Kharzeev, Joachim Kopp, Nicholas Rodd, Andrew Strominger, and Alexander Zhiboedov, whose insights and discussions over the years have profoundly shaped my perspective on many aspects of this broad and evolving field. I am grateful to the Max Planck Institutes for Physics and for Astrophysics in Garching, and to Johannes Henn and Eiichiro Komatsu, for their kind hospitality during the initial stage of this work, as well as to DESY and Geraldine Servant for their warm hospitality during its final stage; both institutes provided an excellent environment for the completion of this manuscript. This work was supported by

the Royal Society through a University Research Fellowship (Grant No. RE22432) and by the Deutsche Forschungsgemeinschaft under Germany's Excellence Strategy (EXC 2121 Quantum Universe – 390833306).

References

- [1] A. Einstein, *Approximative Integration of the Field Equations of Gravitation*, *Sitzungsber. Preuss. Akad. Wiss. Berlin (Math. Phys.)* **1916** (1916) 688.
- [2] H. Bondi, *Plane gravitational waves in general relativity*, *Nature* **179** (1957) 1072.
- [3] R.A. Hulse and J.H. Taylor, *Discovery of a pulsar in a binary system*, *Astrophysical Journal Letters* **195** (1975) L51.
- [4] LIGO SCIENTIFIC AND VIRGO collaboration, *Observation of gravitational waves from a binary black hole merger*, *Phys. Rev. Lett.* **116** (2016) 061102 [1602.03837].
- [5] E. Komatsu, *New physics from the polarized light of the cosmic microwave background*, *Nature Rev. Phys.* **4** (2022) 452 [2202.13919].
- [6] LISA COSMOLOGY WORKING GROUP collaboration, *Cosmology with the Laser Interferometer Space Antenna*, *Living Rev. Rel.* **26** (2023) 5 [2204.05434].
- [7] C. Caprini and D.G. Figueroa, *Cosmological backgrounds of gravitational waves*, *Class. Quant. Grav.* **35** (2018) 163001 [1801.04268].
- [8] M. Hindmarsh, S.J. Huber, K. Rummukainen and D.J. Weir, *Gravitational waves from the sound of a first order phase transition*, *Phys. Rev. Lett.* **112** (2014) 041301 [1304.2433].
- [9] A. Dimitriou, D.G. Figueroa, P. Simakachorn and B. Zaldivar, *Cosmic string gravitational wave backgrounds at LISA: I. Signal survey, template reconstruction, and model comparison*, **2508.05395**.
- [10] S.H.-S. Alexander, M.E. Peskin and M.M. Sheikh-Jabbari, *Leptogenesis from gravity waves in models of inflation*, *Phys. Rev. Lett.* **96** (2006) 081301 [hep-th/0403069].
- [11] A. Maleknejad, *Chiral Gravity Waves and Leptogenesis in Inflationary Models with non-Abelian Gauge Fields*, *Phys. Rev. D* **90** (2014) 023542 [1401.7628].
- [12] M. Garny, M. Sandora and M.S. Sloth, *Planckian Interacting Massive Particles as Dark Matter*, *Phys. Rev. Lett.* **116** (2016) 101302 [1511.03278].
- [13] A. Maleknejad, *Gravitational leptogenesis in axion inflation with $SU(2)$ gauge field*, *JCAP* **1612** (2016) 027 [1604.06520].
- [14] R.R. Caldwell and C. Devulder, *Axion Gauge Field Inflation and Gravitational Leptogenesis: A Lower Bound on B Modes from the Matter-Antimatter Asymmetry of the Universe*, *Phys. Rev.* **D97** (2018) 023532 [1706.03765].
- [15] S. Alexander, E. McDonough and D.N. Spergel, *Chiral Gravitational Waves and Baryon Superfluid Dark Matter*, *JCAP* **05** (2018) 003 [1801.07255].
- [16] N. Bernal, M. Dutra, Y. Mambrini, K. Olive, M. Peloso and M. Pierre, *Spin-2 Portal Dark Matter*, *Phys. Rev. D* **97** (2018) 115020 [1803.01866].
- [17] S. Clery, Y. Mambrini, K.A. Olive and S. Verner, *Gravitational portals in the early Universe*, *Phys. Rev. D* **105** (2022) 075005 [2112.15214].

- [18] A. Maleknejad and J. Kopp, *Weyl fermion creation by cosmological gravitational wave background at 1-loop*, *JHEP* **01** (2025) 023 [[2406.01534](#)].
- [19] A. Maleknejad and J. Kopp, *Gravitational Wave-Induced Freeze-In of Fermionic Dark Matter*, [2405.09723](#).
- [20] R. Garani, M. Redi and A. Tesi, *Particle production from inhomogeneities: general metric perturbations*, *JHEP* **08** (2025) 037 [[2502.12249](#)].
- [21] A. Maleknejad, *Gravitational ABJ Anomaly, Stochastic Matter Production, and Leptogenesis*, [2412.09490](#).
- [22] P. Campeti and others (LiteBIRD Collaboration), *LiteBIRD Science Goals and Forecasts: A Case Study of the Origin of Primordial Gravitational Waves using Large-Scale CMB Polarization*, *Journal of Cosmology and Astroparticle Physics* (2024) [[2312.00717](#)].
- [23] CMB-S4 Collaboration, *CMB-S4 Science Book: Probing Fundamental Physics with Next-Generation CMB Polarization Measurements*, *Proceedings of the National Academy of Sciences* (2019) [[20190032159](#)].
- [24] NANOGrav Collaboration, *The NANOGrav 15-year Data Set: Evidence for a Gravitational-Wave Background*, *Astrophys. J. Lett.* **951** (2023) L8 [[2306.16213](#)].
- [25] J. Antoniadis and others (EPTA Collaboration), *The second data release from the European Pulsar Timing Array III. Search for gravitational wave signals*, *Astron. Astrophys.* **678** (2023) A50 [[2306.16214](#)].
- [26] D.J. Reardon and others (PPTA Collaboration), *Search for an isotropic gravitational-wave background with the Parkes Pulsar Timing Array*, *Astrophys. J. Lett.* **951** (2023) L6 [[2306.16215](#)].
- [27] M. Çalışkan, Y. Chen, L. Dai, N. Anil Kumar, I. Stomberg and X. Xue, *Dissecting the stochastic gravitational wave background with astrometry*, *JCAP* **05** (2024) 030 [[2312.03069](#)].
- [28] J. Garcia-Bellido, H. Murayama and G. White, *Exploring the early Universe with Gaia and Theia*, *JCAP* **12** (2021) 023 [[2104.04778](#)].
- [29] M. Colpi and et al., *LISA Definition Study Report (Red Book)*, [2402.07571](#).
- [30] T. Akutsu and others (KAGRA Collaboration), *KAGRA: 2.5 generation interferometric gravitational wave detector*, *Nature Astron.* **3** (2019) 35 [[1811.08079](#)].
- [31] S. Priyadarshini, *India to begin construction of gravitational wave project*, *Nature* **632** (2025) 85.
- [32] C.F. Sintes et al., *The Science of the Einstein Telescope*, [2503.12263](#).
- [33] P.W. Graham, J.M. Hogan, M.A. Kasevich and S. Rajendran, *New method for gravitational wave detection with atomic sensors*, *Physical Review Letters* **110** (2013) 171102.
- [34] S. Dimopoulos, P.W. Graham, J.M. Hogan, M.A. Kasevich and S. Rajendran, *Atomic gravitational wave interferometric sensor*, *Physical Review D* **78** (2008) 122002.
- [35] J.M. Hogan, D.M.S. Johnson, S. Dickerson, T. Kovachy, A. Sugarbaker, S.-w. Chiow et al., *An atomic gravitational wave interferometric sensor in low earth orbit (agis-leo)*, *General Relativity and Gravitation* **43** (2011) 1953.
- [36] B. Canuel et al., *Exploring gravity with the miga large scale atom interferometer*, *Nature Communications* **8** (2017) 1572.

- [37] M. Zhan et al., *ZAIGA: Zhaoshan long-baseline atom interferometer gravitation antenna*, *International Journal of Modern Physics D* **29** (2020) 1940005.
- [38] P.W. Graham et al., *Mid-band gravitational wave detection with precision atomic sensors*, *arXiv e-prints* (2017) [[1711.02225](#)].
- [39] B. Canuel et al., *ELGAR: A european laboratory for gravitation and atom-interferometric research*, *Classical and Quantum Gravity* **37** (2020) 225017.
- [40] L. Badurina et al., *AION: An atom interferometer observatory and network*, *Journal of Cosmology and Astroparticle Physics* **05** (2020) 011.
- [41] Y.A. El-Neaj et al., *AEDGE: Atomic experiment for dark matter and gravity exploration*, *EPJ Quantum Technology* **7** (2020) 6.
- [42] S. Schiller et al., *The space-time explorer and quantum test of the equivalence principle (ste-quest)*, *arXiv e-prints* (2015) [[1501.03989](#)].
- [43] F. Dückel et al., *The maius-1 mission: Space atom interferometry on a sounding rocket*, *npj Microgravity* **4** (2018) 16.
- [44] I. Alonso et al., *Cold atoms in space: community workshop summary and proposed road-map*, *EPJ Quant. Technol.* **9** (2022) 30 [[2201.07789](#)].
- [45] S. Abend et al., *Terrestrial Very-Long-Baseline Atom Interferometry: Workshop Summary*, *AVS Quantum Sci.* **6** (2024) 024701 [[2310.08183](#)].
- [46] A. Abdalla et al., *Terrestrial Very-Long-Baseline Atom Interferometry: summary of the second workshop*, *EPJ Quant. Technol.* **12** (2025) 42 [[2412.14960](#)].
- [47] N. Aggarwal et al., *Challenges and Opportunities of Gravitational Wave Searches at Frequencies Above the LIGO/Virgo Band*, [2501.11723](#).
- [48] G. Tobar, S.K. Manikandan, T. Beitel and I. Pikovski, *Detecting single gravitons with quantum sensing*, *Nature Commun.* **15** (2024) 7229 [[2308.15440](#)].
- [49] D.E. Kharzeev, A. Maleknejad and S. Shalamberidze, *QuGrav: Bringing gravitational waves to light with Qumodes*, [2506.09459](#).
- [50] LITEBIRD collaboration, *Probing Cosmic Inflation with the LiteBIRD Cosmic Microwave Background Polarization Survey*, *PTEP* **2023** (2023) 042F01 [[2202.02773](#)].
- [51] C. de Rham, *Massive Gravity*, *Living Rev. Rel.* **17** (2014) 7 [[1401.4173](#)].
- [52] C.M. Will, *The Confrontation between General Relativity and Experiment*, *Living Rev. Rel.* **17** (2014) 4 [[1403.7377](#)].
- [53] J.M. Ezquiaga and M. Zumalacárregui, *Dark Energy After GW170817: Dead Ends and the Road Ahead*, *Phys. Rev. Lett.* **119** (2017) 251304 [[1710.05901](#)].
- [54] N.T. Bishop and L. Rezzolla, *Extraction of Gravitational Waves in Numerical Relativity*, *Living Rev. Rel.* **19** (2016) 2 [[1606.02532](#)].
- [55] Y.B. Zel'dovich and A.G. Polnarev, *Radiation of gravitational waves by a cluster of superdense stars*, *Sov. Astron.* **18** (1974) 17.
- [56] V.B. Braginsky and L.P. Grishchuk, *Kinematic Resonance and Memory Effect in Free Mass Gravitational Antennas*, *Sov. Phys. JETP* **62** (1985) 427.
- [57] D. Christodoulou, *Nonlinear nature of gravitation and gravitational-wave experiments*, *Phys. Rev. Lett.* **67** (1991) 1486–1489.

- [58] M.G.J.v.d.B. H. Bondi and A.W.K. Metzner, *Gravitational waves in general relativity. vii. waves from axi-symmetric isolated systems*, *Proc. Roy. Soc. Lond. A* **269** (1962) 21.
- [59] R.K. Sachs, *Gravitational waves in general relativity. viii. waves in asymptotically flat space-times*, *Proc. Roy. Soc. Lond. A* **270** (1962) 103.
- [60] P.D. Lasky, E. Thrane, Y. Levin, J. Blackman and Y. Chen, *Detecting gravitational-wave memory with LIGO: implications of GW150914*, *Phys. Rev. Lett.* **117** (2016) 061102 [[1605.01415](#)].
- [61] H. Inchauspé, S. Gasparotto, D. Blas, L. Heisenberg, J. Zosso and S. Tiwari, *Measuring gravitational wave memory with LISA*, *Phys. Rev. D* **111** (2025) 044044 [[2406.09228](#)].
- [62] J.B. Wang et al., *Searching for gravitational wave memory bursts with the Parkes Pulsar Timing Array*, *Mon. Not. Roy. Astron. Soc.* **446** (2015) 1657 [[1410.3323](#)].
- [63] F.A.E. Pirani, *Invariant formulation of gravitational radiation theory*, *Phys. Rev.* **105** (1957) 1089.
- [64] E.T. Newman and R. Penrose, *An approach to gravitational radiation by a method of spin coefficients*, *Journal of Mathematical Physics* **3** (1962) 566.
- [65] A.Z. Petrov, *Klassifikatsiya prostranstv, opredelyayushchikh polya tyagotenia*, *Uchenye Zapiski Kazanskogo Gosudarstvennogo Universiteta im. V. I. Ulyanova-Lenina* **114** (1954) 55.
- [66] R.M. Wald, *General Relativity*, Chicago Univ. Pr., Chicago, USA (1984), [10.7208/chicago/9780226870373.001.0001](#).
- [67] J.N. Goldberg and R.K. Sachs, *A theorem on Petrov types*, *Acta Physica Polonica* **22** (1962) 13.
- [68] H. Stephani, D. Kramer, M.A.H. MacCallum, C. Hoenselaers and E. Herlt, *Exact Solutions of Einstein's Field Equations*, Cambridge University Press, 2 ed. (2003).
- [69] R.K. Sachs, *Gravitational waves in general relativity. vi. the outgoing radiation condition*, *Proceedings of the Royal Society of London. Series A, Mathematical and Physical Sciences* **264** (1961) 309.
- [70] H. Bondi, F.A.E. Pirani and I. Robinson, *Gravitational waves in general relativity. 3. Exact plane waves*, *Proc. Roy. Soc. Lond.* **A251** (1959) 519.
- [71] T. Mädler and J. Winicour, *Bondi-Sachs Formalism*, *Scholarpedia* **11** (2016) 33528 [[1609.01731](#)].
- [72] J. Winicour, *Characteristic Evolution and Matching*, *Living Rev. Rel.* **12** (2009) 3 [[0810.1903](#)].
- [73] A. Strominger, *Lectures on the Infrared Structure of Gravity and Gauge Theory*, [1703.05448](#).
- [74] J. Lense and H. Thirring, *Ueber den Einfluss der Eigenrotation der Zentralkörper auf die Bewegung der Planeten und Monde nach der Einsteinschen Gravitationstheorie*, *Phys. Z.* **19** (1918) 156.
- [75] R.M. Wald, *Asymptotic behavior of homogeneous cosmological models in the presence of a positive cosmological constant*, *Phys. Rev.* **D28** (1983) 2118.
- [76] L. Bieri and P.T. Chruściel, *Future-complete null hypersurfaces, interior gluings, and the Trautman-Bondi mass*, [1612.04359](#).

- [77] V.-L. Saw, *Mass-loss of an isolated gravitating system due to energy carried away by gravitational waves with a cosmological constant*, *Phys. Rev. D* **94** (2016) 104004 [[1605.05151](#)].
- [78] R. Sachs, *Asymptotic symmetries in gravitational theory*, *Phys. Rev.* **128** (1962) 2851.
- [79] A. Strominger and A. Zhiboedov, *Gravitational Memory, BMS Supertranslations and Soft Theorems*, *JHEP* **01** (2016) 086 [[1411.5745](#)].
- [80] T. Mädler and J. Winicour, *Bondi-Sachs Formalism*, *Scholarpedia* **11** (2016) 33528 [[1609.01731](#)].
- [81] S. Weinberg, *Infrared photons and gravitons*, *Phys. Rev.* **140** (1965) B516.
- [82] A. Strominger, *On BMS Invariance of Gravitational Scattering*, *JHEP* **07** (2014) 152 [[1312.2229](#)].
- [83] K.S. Thorne, *Gravitational-wave bursts with memory: The Christodoulou effect*, *Phys. Rev. D* **45** (1992) 520.
- [84] A. Strominger and A. Zhiboedov, *Gravitational memory, bms supertranslations and soft theorems*, *JHEP* (2016) [[1411.5745](#)].
- [85] L. Bieri and D. Garfinkle, *An electromagnetic analogue of gravitational wave memory*, *Classical and Quantum Gravity* **30** (2013) 195009 [[1307.5098](#)].
- [86] A. Strominger, *Asymptotic Symmetries of Yang-Mills Theory*, *JHEP* **07** (2014) 151 [[1308.0589](#)].
- [87] T. He, P. Mitra, A.P. Porfyriadis and A. Strominger, *New Symmetries of Massless QED*, *JHEP* **10** (2014) 112 [[1407.3789](#)].
- [88] D. Kapec, M. Pate and A. Strominger, *New Symmetries of QED*, *Adv. Theor. Math. Phys.* **21** (2017) 1769 [[1506.02906](#)].
- [89] A. Maleknejad, *Chiral photon memory effect and parity violation in electromagnetic radiation*, *Journal of High Energy Physics* **07** (2020) 154 [[2003.05396](#)].
- [90] PLANCK collaboration, *Planck 2018 results. VI. Cosmological parameters*, *Astron. Astrophys.* **641** (2020) A6 [[1807.06209](#)].
- [91] B. Spokoiny, *Deflationary universe scenario*, *Phys. Lett. B* **315** (1993) 40 [[gr-qc/9306008](#)].
- [92] M. Joyce, *Electroweak baryogenesis and the expansion rate of the universe*, *Phys. Rev. D* **55** (1997) 1875 [[hep-ph/9606223](#)].
- [93] P.G. Ferreira and M. Joyce, *Cosmology with a primordial scaling field*, *Phys. Rev. D* **58** (1998) 023503 [[astro-ph/9711102](#)].
- [94] Y. Gouttenoire, G. Servant and P. Simakachorn, *Kination cosmology from scalar fields and gravitational-wave signatures*, [2111.01150](#).
- [95] S. Weinberg, *Adiabatic modes in cosmology*, *Phys. Rev.* **D67** (2003) 123504 [[astro-ph/0302326](#)].
- [96] A.A. Starobinsky, *A new type of isotropic cosmological models without singularity*, *Physics Letters B* **91** (1980) 99.
- [97] K. Sato, *First-order phase transition of a vacuum and the expansion of the universe*, *Monthly Notices of the Royal Astronomical Society* **195** (1981) 467.

- [98] A.H. Guth, *Inflationary universe: A possible solution to the horizon and flatness problems*, *Physical Review D* **23** (1981) 347.
- [99] A.D. Linde, *A new inflationary universe scenario: A possible solution of the horizon, flatness, homogeneity, isotropy and primordial monopole problems*, *Physics Letters B* **108** (1982) 389.
- [100] G.W. Gibbons and S.W. Hawking, *Cosmological Event Horizons, Thermodynamics, and Particle Creation*, *Phys. Rev. D* **15** (1977) 2738.
- [101] S.W. Hawking and I.G. Moss, *Supercooled Phase Transitions in the Very Early Universe*, *Phys. Lett. B* **110** (1982) 35.
- [102] A. Maleknejad and M.M. Sheikh-Jabbari, *Revisiting Cosmic No-Hair Theorem for Inflationary Settings*, *Phys. Rev. D* **85** (2012) 123508 [1203.0219].
- [103] M.-a. Watanabe, S. Kanno and J. Soda, *Inflationary Universe with Anisotropic Hair*, *Phys. Rev. Lett.* **102** (2009) 191302 [0902.2833].
- [104] W.E. East, M. Kleban, A. Linde and L. Senatore, *Beginning inflation in an inhomogeneous universe*, *JCAP* **09** (2016) 010 [1511.05143].
- [105] V.F. Mukhanov and G.V. Chibisov, *Quantum fluctuations and a nonsingular universe*, *JETP Lett.* **33** (1981) 532.
- [106] S.W. Hawking, *The development of irregularities in a single bubble inflationary universe*, *Phys. Lett. B* **115** (1982) 295.
- [107] A.A. Starobinsky, *Dynamics of phase transition in the new inflationary universe scenario and generation of perturbations*, *Phys. Lett. B* **117** (1982) 175.
- [108] A.H. Guth and S.-Y. Pi, *Fluctuations in the new inflationary universe*, *Phys. Rev. Lett.* **49** (1982) 1110.
- [109] J.M. Bardeen, P.J. Steinhardt and M.S. Turner, *Spontaneous creation of almost scale-free density perturbations in an inflationary universe*, *Phys. Rev. D* **28** (1983) 679.
- [110] G.F. Smoot, C.L. Bennett, A. Kogut, E.L. Wright, J. Aymon, N.W. Boggess et al., *Structure in the COBE differential microwave radiometer first-year maps*, *Astrophys. J. Lett.* **396** (1992) L1.
- [111] G. Hinshaw, D. Larson, E. Komatsu, D.N. Spergel, C.L. Bennett, J. Dunkley et al., *Nine-year wilkinson microwave anisotropy probe (WMAP) observations: Cosmological parameter results*, *Astrophys. J. Suppl.* **208** (2013) 19 [1212.5226].
- [112] R. Kallosh, A. Linde and D. Roest, *ACT, SPT, and chaotic inflation*, *arXiv e-print* (2025) [2503.21030].
- [113] P.A.R.e.a.B.C. Ade, *Improved constraints on primordial gravitational waves using Planck, WMAP, and BICEP/Keck observations through the 2018 observing season*, *Physical Review Letters* **127** (2021) 151301.
- [114] H.e.a.B.A.C. Hui, *BICEP Array: a multi-frequency degree-scale CMB polarimeter*, *arXiv e-print* (2018) [1808.00568].
- [115] SIMONS OBSERVATORY collaboration, *The simons observatory: Science goals and forecasts*, *JCAP* **02** (2019) 056 [1808.07445].
- [116] A.A. Starobinsky, *Spectrum of relict gravitational radiation and the early state of the universe*, *JETP Lett.* **30** (1979) 682.

- [117] E.W. Kolb and M.S. Turner, *The Early Universe*, vol. 69 of *Frontiers in Physics*, Addison-Wesley, Redwood City, USA (1990).
- [118] S. Dodelson and F. Schmidt, *Modern Cosmology*, Academic Press, Cambridge, MA, 2 ed. (2020).
- [119] R.H. Brandenberger, *Introduction to Early Universe Cosmology*, *PoS ICFI2010* (2010) 001 [[1103.2271](#)].
- [120] J.M. Cline, *TASI Lectures on Early Universe Cosmology: Inflation, Baryogenesis and Dark Matter*, *PoS TASI2018* (2019) 001 [[1807.08749](#)].
- [121] V.F. Mukhanov, *Physical Foundations of Cosmology*, Cambridge University Press, Cambridge, UK (2005), [10.1017/CBO9780511790553](#).
- [122] S. Weinberg, *Cosmology* (2008).
- [123] F.W.J. Olver, A.B.O. Daalhuis, D.W. Lozier, B.I. Schneider, R.F. Boisvert, C.W. Clark et al., eds., *NIST Digital Library of Mathematical Functions*, National Institute of Standards and Technology, Gaithersburg, Maryland (2023).
- [124] BICEP, KECK collaboration, *Improved Constraints on Primordial Gravitational Waves using Planck, WMAP, and BICEP/Keck Observations through the 2018 Observing Season*, *Phys. Rev. Lett.* **127** (2021) 151301 [[2110.00483](#)].
- [125] J.M. Bardeen, *Gauge Invariant Cosmological Perturbations*, *Phys. Rev. D* **22** (1980) 1882.
- [126] R.H. Brandenberger and R. Kahn, *COSMOLOGICAL PERTURBATIONS IN INFLATIONARY UNIVERSE MODELS*, *Phys. Rev. D* **29** (1984) 2172.
- [127] V.F. Mukhanov, L.R.W. Abramo and R.H. Brandenberger, *On the Back reaction problem for gravitational perturbations*, *Phys. Rev. Lett.* **78** (1997) 1624 [[gr-qc/9609026](#)].
- [128] A. Maleknejad, M.M. Sheikh-Jabbari and J. Soda, *Gauge Fields and Inflation*, *Phys. Rept.* **528** (2013) 161 [[1212.2921](#)].
- [129] P. Adshead, E. Martinec and M. Wyman, *Gauge fields and inflation: Chiral gravitational waves, fluctuations, and the Lyth bound*, *Phys. Rev.* **D88** (2013) 021302 [[1301.2598](#)].
- [130] E. Dimastrogiovanni and M. Peloso, *Stability analysis of chromo-natural inflation and possible evasion of Lyth's bound*, *Phys. Rev.* **D87** (2013) 103501 [[1212.5184](#)].
- [131] A. Maleknejad, *Axion Inflation with an $SU(2)$ Gauge Field: Detectable Chiral Gravity Waves*, *JHEP* **07** (2016) 104 [[1604.03327](#)].
- [132] A. Maleknejad and E. Komatsu, *Production and Backreaction of Spin-2 Particles of $SU(2)$ Gauge Field during Inflation*, *JHEP* **05** (2019) 174 [[1808.09076](#)].
- [133] PLANCK collaboration, *Planck 2018 results. X. Constraints on inflation*, [1807.06211](#).
- [134] E. Komatsu et al., *Non-Gaussianity as a Probe of the Physics of the Primordial Universe and the Astrophysics of the Low Redshift Universe*, [0902.4759](#).
- [135] E. Komatsu and D.N. Spergel, *Acoustic signatures in the primary microwave background bispectrum*, *Phys. Rev. D* **63** (2001) 063002 [[astro-ph/0005036](#)].
- [136] E. Komatsu, *Hunting for Primordial Non-Gaussianity in the Cosmic Microwave Background*, *Class. Quant. Grav.* **27** (2010) 124010 [[1003.6097](#)].
- [137] E. Pajer, F. Schmidt and M. Zaldarriaga, *The observed squeezed limit of cosmological three-point functions*, *Phys. Rev. D* **88** (2013) 083502 [[1305.0824](#)].

- [138] P. Creminelli, J. Noreña and M. Simonović, *Conformal consistency relations for single-field inflation*, *JCAP* **1207** (2012) 052 [[1203.4595](#)].
- [139] K. Hinterbichler, L. Hui and J. Khoury, *An Infinite Set of Ward Identities for Adiabatic Modes in Cosmology*, *JCAP* **1401** (2014) 039 [[1304.5527](#)].
- [140] E. Schrodinger, *The proper vibrations of the expanding universe*, *Physica* **6** (1939) 899.
- [141] L. Parker, *Particle creation in expanding universes*, *Phys. Rev. Lett.* **21** (1968) 562.
- [142] E.W. Kolb and A.J. Long, *Cosmological gravitational particle production and its implications for cosmological relics*, *Rev. Mod. Phys.* **96** (2024) 045005 [[2312.09042](#)].
- [143] X. Chen and Y. Wang, *Quasi-Single Field Inflation and Non-Gaussianities*, *JHEP* **08** (2010) 044 [[0911.3380](#)].
- [144] X. Chen, *Primordial Non-Gaussianities from Inflation Models*, *Adv. Astron.* **2010** (2010) 157080 [[1002.1416](#)].
- [145] T. Noumi, M. Yamaguchi and D. Yokoyama, *Effective field theory approach to quasi-single field inflation and effects of heavy fields*, *JHEP* **06** (2013) 051 [[1211.1624](#)].
- [146] N. Arkani-Hamed and J. Maldacena, *Cosmological Collider Physics*, [1503.08043](#).
- [147] X. Chen, M.H. Namjoo and Y. Wang, *Quantum Primordial Standard Clocks*, *JCAP* **02** (2016) 013 [[1509.03930](#)].
- [148] H. Lee, D. Baumann and G.L. Pimentel, *Non-Gaussianity as a Particle Detector*, *JHEP* **12** (2016) 040 [[1607.03735](#)].
- [149] N. Arkani-Hamed, D. Baumann, H. Lee and G.L. Pimentel, *The Cosmological Bootstrap: Inflationary Correlators from Symmetries and Singularities*, *JHEP* **04** (2020) 105 [[1811.00024](#)].
- [150] S. Jazayeri and S. Renaux-Petel, *Cosmological bootstrap in slow motion*, *JHEP* **12** (2022) 137 [[2205.10340](#)].
- [151] A. Bodas, S. Kumar and R. Sundrum, *The Scalar Chemical Potential in Cosmological Collider Physics*, *JHEP* **02** (2021) 079 [[2010.04727](#)].
- [152] S. Jazayeri, S. Renaux-Petel, X. Tong, D. Werth and Y. Zhu, *Parity violation from emergent nonlocality during inflation*, *Phys. Rev. D* **108** (2023) 123523 [[2308.11315](#)].
- [153] C. de Rham, S. Jazayeri and A.J. Tolley, *Bispectrum islands: Bootstrap bounds on cosmological correlators*, *Phys. Rev. D* **112** (2025) 083531 [[2506.19198](#)].
- [154] W. Sohn, D.-G. Wang, J.R. Fergusson and E.P.S. Shellard, *Searching for cosmological collider in the Planck CMB data*, *JCAP* **09** (2024) 016 [[2404.07203](#)].
- [155] G. Cabass, M.M. Ivanov, O.H.E. Philcox, M. Simonović and M. Zaldarriaga, *Constraints on Single-Field Inflation from the BOSS Galaxy Survey*, *Phys. Rev. Lett.* **129** (2022) 021301 [[2201.07238](#)].
- [156] D. Baumann, D. Green, A. Joyce, E. Pajer, G.L. Pimentel, C. Sleight et al., *Snowmass White Paper: The Cosmological Bootstrap*, *SciPost Phys. Comm. Rep.* **2024** (2024) 1 [[2203.08121](#)].
- [157] M. Maggiore, *Gravitational Waves. Vol. 2: Astrophysics and Cosmology*, Oxford University Press (2018).

- [158] Y. Watanabe and E. Komatsu, *Improved Calculation of the Primordial Gravitational Wave Spectrum in the Standard Model*, *Phys. Rev. D* **73** (2006) 123515 [[astro-ph/0604176](#)].
- [159] K. Saikawa and S. Shirai, *Primordial gravitational waves, precisely: The role of thermodynamics in the Standard Model*, *JCAP* **05** (2018) 035 [[1803.01038](#)].
- [160] R.K. Sachs and A.M. Wolfe, *Perturbations of a cosmological model and angular variations of the microwave background*, *Astrophys. J.* **147** (1967) 73.
- [161] J. Lesgourgues, *The cosmic linear anisotropy solving system (CLASS) III: Comparison with CAMB for Λ CDM*, *JCAP* **09** (2011) 032 [[1104.2934](#)].
- [162] T. Kite, A. Ravenni, S.P. Patil and J. Chluba, *Bridging the gap: spectral distortions meet gravitational waves*, *Mon. Not. Roy. Astron. Soc.* **505** (2021) 4396 [[2010.00040](#)].
- [163] R.S. Foster and D.C. Backer, *Constructing a pulsar timing array*, *Astrophys. J.* **361** (1990) 300.
- [164] R.N. Manchester et al., *The parkes pulsar timing array project*, *Publ. Astron. Soc. Australia* **30** (2013) e017 [[1309.7392](#)].
- [165] J.P.W. Verbiest, S.J. Vigeland, N.K. Porayko, S. Chen and D.J. Reardon, *Status report on global pulsar-timing-array efforts to detect gravitational waves*, *Results Phys.* **61** (2024) 107719 [[2404.19529](#)].
- [166] EPTA collaboration, *The second data release from the European Pulsar Timing Array - I. The dataset and timing analysis*, *Astron. Astrophys.* **678** (2023) A48 [[2306.16224](#)].
- [167] EPTA, INPTA: collaboration, *The second data release from the European Pulsar Timing Array - III. Search for gravitational wave signals*, *Astron. Astrophys.* **678** (2023) A50 [[2306.16214](#)].
- [168] P. Rana et al., *The Indian Pulsar Timing Array Data Release 2: I. Dataset and Timing Analysis*, [2506.16769](#).
- [169] D.J. Reardon et al., *Search for an Isotropic Gravitational-wave Background with the Parkes Pulsar Timing Array*, *Astrophys. J. Lett.* **951** (2023) L6 [[2306.16215](#)].
- [170] A. Zic et al., *The Parkes Pulsar Timing Array third data release*, *Publ. Astron. Soc. Austral.* **40** (2023) e049 [[2306.16230](#)].
- [171] H. Xu et al., *Searching for the Nano-Hertz Stochastic Gravitational Wave Background with the Chinese Pulsar Timing Array Data Release I*, *Res. Astron. Astrophys.* **23** (2023) 075024 [[2306.16216](#)].
- [172] A. Weltman et al., *Fundamental physics with the Square Kilometre Array*, *Publ. Astron. Soc. Austral.* **37** (2020) e002 [[1810.02680](#)].
- [173] G. Janssen et al., *Gravitational wave astronomy with the SKA*, *PoS AASKA14* (2015) 037 [[1501.00127](#)].
- [174] P.R. Saulson, *Fundamentals of Interferometric Gravitational Wave Detectors*, World Scientific, Singapore (1994).
- [175] W.-R. Hu and Y.-L. Wu, *The Taiji Program in Space for gravitational wave physics and the nature of gravity*, *Natl. Sci. Rev.* **4** (2017) 685.
- [176] W.-H. Ruan, C. Liu, Z.-K. Guo, Y.-L. Wu and R.-G. Cai, *The LISA-Taiji network*, *Nature Astron.* **4** (2020) 108 [[2002.03603](#)].

- [177] TIANQIN collaboration, *The TianQin project: current progress on science and technology*, *PTEP* **2021** (2021) 05A107 [[2008.10332](#)].
- [178] S. Kawamura et al., *Current status of space gravitational wave antenna DECIGO and B-DECIGO*, *PTEP* **2021** (2021) 05A105 [[2006.13545](#)].
- [179] A. Maleknejad and F. Rompineve, *Gravitational waves: a golden era*, *CERN Courier* (2023) .
- [180] N. Aggarwal et al., *Challenges and opportunities of gravitational-wave detection at high frequencies*, *Living Rev. Relativ.* (2025) .
- [181] J. Weber, *Detection and Generation of Gravitational Waves*, *Phys. Rev.* **117** (1960) 306.
- [182] A.S. Chou et al., *MHz gravitational wave constraints with decameter Michelson interferometers*, *Phys. Rev. D* **95** (2017) 063002 [[1611.05560](#)].
- [183] A. Patra et al., *Broadband Limits on Stochastic Length Fluctuations from a Pair of Table-Top Interferometers*, *Phys. Rev. Lett.* **135** (2025) 101402 [[2410.09175](#)].
- [184] AURIGA collaboration, *Present performance and future upgrades of the AURIGA capacitive readout*, *Class. Quant. Grav.* **23** (2006) S103.
- [185] N. Aggarwal, G.P. Winstone, M. Teo, M. Baryakhtar, S.L. Larson, V. Kalogera et al., *Searching for New Physics with a Levitated-Sensor-Based Gravitational-Wave Detector*, *Phys. Rev. Lett.* **128** (2022) 111101 [[2010.13157](#)].
- [186] V. Domcke, S.A.R. Ellis and N.L. Rodd, *Magnets are Weber Bar Gravitational Wave Detectors*, *Phys. Rev. Lett.* **134** (2025) 231401 [[2408.01483](#)].
- [187] A. Berlin, D. Blas, R. Tito D’Agnolo, S.A.R. Ellis, R. Harnik, Y. Kahn et al., *Detecting high-frequency gravitational waves with microwave cavities*, *Phys. Rev. D* **105** (2022) 116011 [[2112.11465](#)].
- [188] G. Marconato, J. Branlard, C. Dokuyucu, B. Giaccone, W. Hillert, T. Krokotsch et al., *High frequency gravitational wave sensing with superconducting microwave cavities*, .
- [189] R. Ballou et al., *Latest results of the OSQAR photon regeneration experiment*, *Phys. Rev. D* **92** (2015) 092002 [[1506.08082](#)].
- [190] O. Albrecht et al., *The ALPS II experiment: a laser-based search for new physics*, *JINST* **15** (2020) P10003 [[2003.05835](#)].
- [191] V. Anastassopoulos et al., *New CAST limit on the axion–photon interaction*, *Nature Phys.* **13** (2017) 584 [[1705.02290](#)].
- [192] A. Abeln et al., *Conceptual design of the international axion observatory (IAXO)*, *Eur. Phys. J. C* **80** (2020) 497 [[2010.12076](#)].
- [193] E. Armengaud et al., *Physics potential of the international axion observatory (IAXO)*, *JCAP* **06** (2019) 047 [[1904.09155](#)].
- [194] J. Beacham et al., *Physics beyond the standard model at CERN: beyond the LHC*, *Phys. Rept.* **873** (2020) 1 [[1901.09966](#)].
- [195] M.E. Gertsenshtein, *Wave resonance of light and gravitational waves*, *Sov. Phys. JETP* **14** (1962) 84.
- [196] D. Ejlli et al., *Probing high-frequency gravitational waves with photon regeneration*, *Eur. Phys. J. C* **79** (2019) 1032 [[1908.00232](#)].

- [197] W. Ratzinger, S. Schenk and P. Schwaller, *A coordinate-independent formalism for detecting high-frequency gravitational waves*, *JHEP* **08** (2024) 195 [2404.08572].
- [198] A. Blais, A.L. Grimsmo, S.M. Girvin and A. Wallraff, *Circuit quantum electrodynamics*, *Reviews of Modern Physics* **93** (2021) 025005.
- [199] T.J. Stavenger, E. Crane, K.C. Smith, C.T. Kang, S.M. Girvin and N. Wiebe, *Bosonic qiskit*, *arXiv e-prints* (2022) [2209.11153].
- [200] J.Y. Araz, M. Grau, J. Montgomery and F. Ringer, *Toward hybrid quantum simulations with qubits and qumodes on trapped-ion platforms*, *arXiv e-prints* (2024) [2410.07346].
- [201] R.W. Heeres, B. Vlastakis, E. Holland, S. Krastanov, V.V. Albert, L. Frunzio et al., *Cavity state manipulation using photon-number selective phase gates*, *Physical Review Letters* **115** (2015) 137002.
- [202] A. Eickbusch, V. Sivak, A.Z. Ding, S.S. Elder, S.R. Jha, J. Venkatraman et al., *Fast universal control of an oscillator with weak dispersive coupling to a qubit*, *Nature Physics* **18** (2022) 1464.
- [203] R. Cheng, Y. Zhou, S. Wang, M. Shen, T. Taher and H.X. Tang, *A 100-pixel photon-number-resolving detector unveiling photon statistics*, *Nature Photonics* **17** (2023) 112.
- [204] F. Dyson, *Is a graviton detectable?*, *International Journal of Modern Physics A* **28** (2013) 1330041.
- [205] T. Rothman and S. Boughn, *Can gravitons be detected?*, *Foundations of Physics* **36** (2006) 1801 [gr-qc/0601043].
- [206] D. Carney, V. Domcke and N.L. Rodd, *Graviton detection and the quantization of gravity*, *Physical Review D* **109** (2024) 044009 [2308.12988].
- [207] T. Clifton, P.G. Ferreira, A. Padilla and C. Skordis, *Modified Gravity and Cosmology*, *Phys. Rept.* **513** (2012) 1 [1106.2476].
- [208] M. Lewandowski, A. Maleknejad and L. Senatore, *An effective description of dark matter and dark energy in the mildly non-linear regime*, *JCAP* **05** (2017) 038 [1611.07966].
- [209] S. Capozziello, M. De Laurentis, S. Nojiri and S.D. Odintsov, *Evolution of gravitons in accelerating cosmologies: The case of extended gravity*, *Phys. Rev. D* **95** (2017) 083524 [1702.05517].
- [210] P. Creminelli and F. Vernizzi, *Dark Energy after GW170817 and GRB170817A*, *Phys. Rev. Lett.* **119** (2017) 251302 [1710.05877].
- [211] T. Baker, E. Bellini, P.G. Ferreira, M. Lagos, J. Noller and I. Sawicki, *Strong constraints on cosmological gravity from GW170817 and GRB 170817A*, *Phys. Rev. Lett.* **119** (2017) 251301 [1710.06394].
- [212] N. Frusciante and L. Perenon, *Effective field theory of dark energy: A review*, *Phys. Rept.* **857** (2020) 1 [1907.03150].
- [213] LIGO SCIENTIFIC AND VIRGO collaboration, *GW170817: Observation of gravitational waves from a binary neutron star inspiral*, *Phys. Rev. Lett.* **119** (2017) 161101 [1710.05832].
- [214] L. Barack et al., *Black holes, gravitational waves and fundamental physics: A roadmap*, *Class. Quant. Grav.* **36** (2019) 143001 [1806.05195].

- [215] M.C. Begelman, R.D. Blandford and M.J. Rees, *Massive black hole binaries in active galactic nuclei*, *Nature* **287** (1980) 307.
- [216] M. Volonteri, *Formation of supermassive black holes*, *Astron. Astrophys. Rev.* **18** (2010) 279.
- [217] P. Amaro-Seoane et al., *Low-frequency gravitational-wave science with eLISA/NGO*, *Class. Quant. Grav.* **29** (2012) 124016 [[1201.3621](#)].
- [218] L. Barack and C. Cutler, *LISA capture sources: Approximate waveforms, signal-to-noise ratios and parameter estimation accuracy*, *Phys. Rev. D* **75** (2007) 042003 [[gr-qc/0612029](#)].
- [219] S. Babak et al., *Science with the space-based interferometer LISA. V: Extreme mass-ratio inspirals*, *Phys. Rev. D* **95** (2017) 103012 [[1703.09722](#)].
- [220] P. Amaro-Seoane, *Gravitational waves from compact binaries and their detection with LISA*, *Living Rev. Rel.* **25** (2022) 4 [[2203.12508](#)].
- [221] S. Burke-Spolaor et al., *The astrophysics of nanohertz gravitational waves*, *Astron. Astrophys. Rev.* **27** (2019) 5 [[1811.08826](#)].
- [222] L. Mayer, *Massive black hole binaries in gas-rich galaxy mergers*, *Class. Quant. Grav.* **30** (2013) 244008.
- [223] J. Abedi, H. Dykaar and N. Afshordi, *Echoes from the Abyss: Evidence for Planck-scale structure at black hole horizons*, *Phys. Rev. D* **96** (2017) 082004 [[1612.00266](#)].
- [224] J. Abedi, H. Dykaar and N. Afshordi, *Echoes from the Abyss: The Holiday Edition!*, *arXiv e-prints* (2017) [[1701.03485](#)].
- [225] N. Afshordi, J. Abedi and H. Dykaar, *Echoes from the Abyss: A highly spinning black hole remnant for GW150914*, *Phys. Rev. D* **98** (2018) 104046 [[1803.10454](#)].
- [226] N. Andersson and K.D. Kokkotas, *The r-mode instability in rotating neutron stars*, *Int. J. Mod. Phys. D* **10** (2001) 381 [[gr-qc/0010102](#)].
- [227] K. Riles, *Recent searches for continuous gravitational waves*, *Living Rev. Rel.* **25** (2022) 3 [[2206.06447](#)].
- [228] J. Kopp, S. Reddy, L. Roberts and X.-N. Zhou, *Neutron stars and the dark matter problem*, *Phys. Rev. Lett.* **120** (2018) 201102 [[1801.09738](#)].
- [229] A.E. Nelson, S. Reddy and D. Zhou, *Dark halos around neutron stars and gravitational waves*, *JCAP* **07** (2019) 012 [[1803.03266](#)].
- [230] J. Ellis, A. Hektor, G. Hütsi, K. Kannike, L. Marzola, M. Raidal et al., *Search for dark matter effects on gravitational signals from neutron star mergers*, *Phys. Lett. B* **781** (2018) 607 [[1710.05540](#)].
- [231] M. Baryakhtar, R. Lasenby and M.S. Teo, *Dark matter in extreme astrophysical environments*, *Phys. Rev. D* **96** (2017) 035019 [[1704.05081](#)].
- [232] L. Shao, *Tests of gravity with pulsars and neutron stars*, *Universe* **6** (2020) 173 [[2012.10233](#)].
- [233] G. Grippa, G. Montani, M. Orsaria and I.F. Ranea-Sandoval, *Dark matter admixed neutron stars: A review*, *Universe* **8** (2022) 326 [[2203.08684](#)].
- [234] K. Kotake, *Multiple physical elements governing core-collapse supernova explosions*, *Comptes Rendus Physique* **14** (2013) 318 [[1110.5107](#)].

- [235] C.D. Ott, *The gravitational wave signature of core-collapse supernovae*, *Class. Quant. Grav.* **26** (2009) 063001 [0809.0695].
- [236] A. Corsi, *Gravitational waves from gamma-ray burst progenitors*, *Front. Astron. Space Sci.* **6** (2019) 29 [1902.01335].
- [237] A. Sesana, *Systematic investigation of the expected gravitational wave signal from supermassive black hole binaries in the pulsar timing band*, *Mon. Not. Roy. Astron. Soc.* **433** (2013) L1.
- [238] J. Antoniadis and others (EPTA Collaboration), *The european pulsar timing array: Evidence for a gravitational-wave background*, *Astron. Astrophys.* **678** (2023) A50 [2306.16214].
- [239] D.J. Reardon and others (PPTA Collaboration), *Search for an astrophysical gravitational-wave background in the second data release of the parkes pulsar timing array*, *Astrophys. J. Lett.* **951** (2023) L6 [2306.16215].
- [240] ET collaboration, *The Science of the Einstein Telescope*, 2503.12263.
- [241] LISA COSMOLOGY WORKING GROUP collaboration, *Gravitational waves from inflation in LISA: reconstruction pipeline and physics interpretation*, *JCAP* **11** (2024) 032 [2407.04356].
- [242] J.-F. Dufaux, J. Bergman, G.N. Felder, L. Kofman and J.-P. Uzan, *Theory and numerics of gravitational waves from preheating after inflation*, *Phys. Rev. D* **76** (2007) 123517.
- [243] D.G. Figueroa and F. Torrenti, *Gravitational waves from nonlinear dynamics of gauge fields during preheating*, *JCAP* **2017** (2017) 057.
- [244] P. Adshead, J.T. Giblin and M. Pieroni, *Gravitational waves from gauge preheating*, *JCAP* **2019** (2019) 057.
- [245] K.D. Lozanov and M.A. Amin, *Gravitational perturbations from resonant non-abelian gauge-field production after inflation*, *Phys. Rev. D* **99** (2019) 123504.
- [246] T. Clarke, R. Caldwell and K. Hinterbichler, *Primordial gravitational waves and cosmology*, *Phys. Rev. D* **103** (2021) 043512.
- [247] L. Pagano, L. Salvati and A. Melchiorri, *New constraints on primordial gravitational waves from planck data*, *Phys. Lett. B* **760** (2016) 823.
- [248] C. Caprini and D.G. Figueroa, *Cosmological backgrounds of gravitational waves*, *Class. Quant. Grav.* **37** (2020) 163001.
- [249] K.N. Ananda, C. Clarkson and D. Wands, *The cosmological gravitational wave background from primordial density perturbations*, *Physical Review D* **75** (2007) 123518.
- [250] D. Baumann, P.J. Steinhardt, K. Takahashi and K. Ichiki, *Gravitational wave spectrum induced by primordial scalar perturbations*, *Physical Review D* **76** (2007) 084019.
- [251] R. Saito and J. Yokoyama, *Gravitational-wave background as a probe of the primordial black-hole abundance*, *Physical Review Letters* **102** (2009) 161101.
- [252] K. Kohri and T. Terada, *Semianalytic calculation of gravitational wave spectrum nonlinearly induced from primordial curvature perturbations*, *Phys. Rev. D* **97** (2018) 123532.
- [253] M. Biagetti, M. Fasiello and A. Riotto, *Enhancing the tensor-to-scalar ratio in simple inflationary models*, *Phys. Rev. D* **88** (2013) 103518.

- [254] J. García-Bellido, M. Peloso, L. Sorbo and C. Ünal, *Gravitational wave signatures from inflationary particle production*, *JCAP* **2021** (2021) 029.
- [255] G. Domènech, *Scalar induced gravitational waves review*, *Universe* **7** (2021) 398.
- [256] C. Yuan and Q.-G. Huang, *A topic review on probing primordial black hole dark matter with scalar induced gravitational waves*, *iScience* **24** (2021) 102860.
- [257] R.D. Peccei and H.R. Quinn, *CP conservation in the presence of instantons*, *Phys. Rev. Lett.* **38** (1977) 1440.
- [258] R.D. Peccei and H.R. Quinn, *Constraints imposed by CP conservation in the presence of instantons*, *Phys. Rev. D* **16** (1977) 1791.
- [259] S. Weinberg, *A new light boson?*, *Phys. Rev. Lett.* **40** (1978) 223.
- [260] F. Wilczek, *Problem of strong P and T invariance in the presence of instantons*, *Phys. Rev. Lett.* **40** (1978) 279.
- [261] M. Dine, W. Fischler and M. Srednicki, *A simple solution to the strong CP problem with a harmless axion*, *Phys. Lett. B* **104** (1981) 199.
- [262] L.F. Abbott and M.B. Wise, *Constraints on generalized axion models*, *Nucl. Phys. B* **244** (1984) 541.
- [263] M.S. Turner and L.M. Widrow, *Inflation-produced, large-scale magnetic fields*, *Phys. Rev. D* **37** (1988) 2743.
- [264] K. Freese, J.A. Frieman and A.V. Olinto, *Natural inflation with pseudo nambu-goldstone bosons*, *Phys. Rev. Lett.* **65** (1990) 3233.
- [265] F.C. Adams, J.R. Bond, K. Freese, J.A. Frieman and A.V. Olinto, *Natural inflation: Particle physics models, power-law spectra for large-scale structure, and constraints from COBE*, *Phys. Rev. D* **47** (1993) 426.
- [266] W.D. Garretson, G.B. Field and S.M. Carroll, *Primordial magnetic fields from pseudo-goldstone bosons*, *Phys. Rev. D* **46** (1992) 5346.
- [267] R. Contino, A. Podo and F. Revello, *Chiral models of composite axions and accidental Peccei-Quinn symmetry*, *JHEP* **04** (2022) 180 [2112.09635].
- [268] A. Maleknejad and E. McDonough, *Ultralight pion and superheavy baryon dark matter*, *Phys. Rev. D* **106** (2022) 095011 [2205.12983].
- [269] D.J.E. Marsh, *Axion Cosmology*, *Phys. Rept.* **643** (2016) 1 [1510.07633].
- [270] P.W. Graham, I.G. Irastorza, S.K. Lamoreaux, A. Lindner and K.A. van Bibber, *Experimental Searches for the Axion and Axion-Like Particles*, *Ann. Rev. Nucl. Part. Sci.* **65** (2015) 485 [1602.00039].
- [271] I.G. Irastorza and J. Redondo, *New experimental approaches in the search for axion-like particles*, *Prog. Part. Nucl. Phys.* **102** (2018) 89 [1801.08127].
- [272] E.G.M. Ferreira, *Ultra-light dark matter*, *Astron. Astrophys. Rev.* **29** (2021) 7 [2005.03254].
- [273] C.B. Adams et al., *Axion Dark Matter*, in *Snowmass 2021*, 3, 2022 [2203.14923].
- [274] A. Ringwald, *Axion dark matter (theory & experiment)*, *PoS TAUP2023* (2024) 015 [2311.11660].
- [275] A. Ringwald, *Review on Axions*, *J. Phys. Conf. Ser.* **3162** (2025) 012006 [2404.09036].

- [276] M.M. Anber and L. Sorbo, *N-flationary magnetic fields*, *JCAP* **10** (2006) 018 [[astro-ph/0606534](#)].
- [277] M.M. Anber and L. Sorbo, *Naturally inflating on steep potentials through electromagnetic dissipation*, *Phys. Rev. D* **81** (2010) 043534 [[0908.4089](#)].
- [278] N. Barnaby, E. Pajer and M. Peloso, *Gauge field production in axion inflation: Consequences for monodromy, non-gaussianity and gravitational waves*, *Phys. Rev. D* **85** (2012) 023525 [[1110.3327](#)].
- [279] A. Maleknejad and M.M. Sheikh-Jabbari, *Gauge-flation: Inflation From Non-Abelian Gauge Fields*, *Phys. Lett.* **B723** (2013) 224 [[1102.1513](#)].
- [280] A. Maleknejad and M.M. Sheikh-Jabbari, *Non-Abelian Gauge Field Inflation*, *Phys. Rev.* **D84** (2011) 043515 [[1102.1932](#)].
- [281] P. Adshead and M. Wyman, *Chromo-Natural Inflation: Natural inflation on a steep potential with classical non-Abelian gauge fields*, *Phys. Rev. Lett.* **108** (2012) 261302 [[1202.2366](#)].
- [282] E. Dimastrogiovanni, M. Fasiello and T. Fujita, *Primordial Gravitational Waves from Axion-Gauge Fields Dynamics*, *JCAP* **1701** (2017) 019 [[1608.04216](#)].
- [283] P. Adshead, E. Martinec and M. Wyman, *Perturbations in Chromo-Natural Inflation*, *JHEP* **09** (2013) 087 [[1305.2930](#)].
- [284] P. Adshead and E.I. Sfakianakis, *Higgsed Gauge-flation*, *JHEP* **08** (2017) 130 [[1705.03024](#)].
- [285] A. Agrawal, T. Fujita and E. Komatsu, *Large tensor non-Gaussianity from axion-gauge field dynamics*, *Phys. Rev. D* **97** (2018) 103526 [[1707.03023](#)].
- [286] A. Agrawal, T. Fujita and E. Komatsu, *Tensor Non-Gaussianity from Axion-Gauge-Fields Dynamics : Parameter Search*, *JCAP* **06** (2018) 027 [[1802.09284](#)].
- [287] A. Maleknejad and M. Zarei, *Slow-roll trajectories in Chromo-Natural and Gauge-flation Models, an exhaustive analysis*, *Phys. Rev.* **D88** (2013) 043509 [[1212.6760](#)].
- [288] C.M. Nieto and Y. Rodriguez, *Massive Gauge-flation*, *Mod. Phys. Lett. A* **31** (2016) 1640005 [[1602.07197](#)].
- [289] P. Adshead, E. Martinec, E.I. Sfakianakis and M. Wyman, *Higgsed Chromo-Natural Inflation*, *JHEP* **12** (2016) 137 [[1609.04025](#)].
- [290] E. McDonough and S. Alexander, *Observable Chiral Gravitational Waves from Inflation in String Theory*, *JCAP* **11** (2018) 030 [[1806.05684](#)].
- [291] J. Holland, I. Zavala and G. Tasinato, *On chromonatural inflation in string theory*, *JCAP* **12** (2020) 026 [[2009.00653](#)].
- [292] Y. Watanabe and E. Komatsu, *Gravitational Wave from Axion-SU(2) Gauge Fields: Effective Field Theory for Kinetically Driven Inflation*, [2004.04350](#).
- [293] A. Maleknejad, *SU(2)R and its axion in cosmology: A common origin for inflation, cold sterile neutrinos, and baryogenesis*, *Phys. Rev. D* **104** (2021) 083518 [[2012.11516](#)].
- [294] O. Iarygina and E.I. Sfakianakis, *Gravitational waves from spectator Gauge-flation*, *JCAP* **11** (2021) 023 [[2105.06972](#)].
- [295] E. Dimastrogiovanni, M. Fasiello, J.M. Leedom, M. Putti and A. Westphal, *Gravitational axiverse spectroscopy: seeing the forest for the axions*, *JHEP* **08** (2024) 072 [[2312.13431](#)].

- [296] A. Maleknejad, M.M. Sheikh-Jabbari and J. Soda, *Gauge-flaton and Cosmic No-Hair Conjecture*, *JCAP* **1201** (2012) 016 [[1109.5573](#)].
- [297] A. Maleknejad and E. Erfani, *Chromo-Natural Model in Anisotropic Background*, *JCAP* **1403** (2014) 016 [[1311.3361](#)].
- [298] I. Wolfson, A. Maleknejad and E. Komatsu, *How attractive is the isotropic attractor solution of axion- $SU(2)$ inflation?*, *JCAP* **09** (2020) 047 [[2003.01617](#)].
- [299] I. Wolfson, A. Maleknejad, T. Murata, E. Komatsu and T. Kobayashi, *The isotropic attractor solution of axion- $SU(2)$ inflation: universal isotropization in Bianchi type-I geometry*, *JCAP* **09** (2021) 031 [[2105.06259](#)].
- [300] P. Adshead and A. Liu, *Anisotropic Massive Gauge-flaton*, *JCAP* **07** (2018) 052 [[1803.07168](#)].
- [301] V. Kamali, *Warm pseudoscalar inflation*, *Phys. Rev. D* **100** (2019) 043520 [[1901.01897](#)].
- [302] K.V. Berghaus, P.W. Graham and D.E. Kaplan, *Minimal Warm Inflation*, *JCAP* **03** (2020) 034 [[1910.07525](#)].
- [303] A. Mehrabi, A. Maleknejad and V. Kamali, *Gaugessence: a dark energy model with early time radiation-like equation of state*, *Astrophys. Space Sci.* **362** (2017) 53 [[1510.00838](#)].
- [304] L. Heisenberg, R. Kase and S. Tsujikawa, *Anisotropic cosmological solutions in massive vector theories*, *JCAP* **11** (2016) 008 [[1607.03175](#)].
- [305] R.R. Caldwell and C. Devulder, *Gravitational Wave Opacity from Gauge Field Dark Energy*, *Phys. Rev. D* **100** (2019) 103510 [[1802.07371](#)].
- [306] A. Guarnizo, J.B. Orjuela-Quintana and C.A. Valenzuela-Toledo, *Dynamical analysis of cosmological models with non-Abelian gauge vector fields*, *Phys. Rev. D* **102** (2020) 083507 [[2007.12964](#)].
- [307] K. Kaneta, H.-S. Lee, J. Lee and J. Yi, *Dark energy under a gauge symmetry: A review of gauged quintessence and its implications*, *Int. J. Mod. Phys. A* **40** (2025) 2530009 [[2504.04820](#)].
- [308] L. Mirzaghali, A. Maleknejad and K.D. Lozanov, *Production and backreaction of fermions from axion- $SU(2)$ gauge fields during inflation*, *Phys. Rev. D* **101** (2020) 083528 [[1905.09258](#)].
- [309] K.D. Lozanov, A. Maleknejad and E. Komatsu, *Schwinger Effect by an $SU(2)$ Gauge Field during Inflation*, *JHEP* **02** (2019) 041 [[1805.09318](#)].
- [310] A. Maleknejad, *Dark Fermions and Spontaneous CP violation in $SU(2)$ -axion Inflation*, *JHEP* **07** (2020) 154 [[1909.11545](#)].
- [311] L. Vicente García-Consuegra and A. Maleknejad, *The Stochastic Schwinger Effect*, [2510.14468](#).
- [312] A. Maleknejad, *Chiral anomaly in $SU(2)_R$ -axion inflation and the new prediction for particle cosmology*, *JHEP* **21** (2020) 113 [[2103.14611](#)].
- [313] G. Elor et al., *New Ideas in Baryogenesis: A Snowmass White Paper*, in *Snowmass 2021*, 3, 2022 [[2203.05010](#)].
- [314] Y. Minami and E. Komatsu, *New extraction of the cosmic birefringence from the planck 2018 polarization data*, *Phys. Rev. Lett.* **125** (2020) 221301 [[2011.11254](#)].

- [315] P. Diego-Palazuelos et al., *Cosmic birefringence from the planck data release 4*, *Phys. Rev. Lett.* **128** (2022) 091302 [[2201.07682](#)].
- [316] J.R. Eskilt and E. Komatsu, *Improved constraints on cosmic birefringence from the WMAP and Planck cosmic microwave background polarization data*, *Phys. Rev. D* **106** (2022) 063503 [[2205.13962](#)].
- [317] P. Diego-Palazuelos and E. Komatsu, *Cosmic birefringence from the atacama cosmology telescope data release 6*, *arXiv e-prints* (2025) [[2509.13654](#)].
- [318] A. Lue, L. Wang and M. Kamionkowski, *Cosmological signature of new parity-violating interactions*, *Phys. Rev. Lett.* **83** (1999) 1506 [[astro-ph/9812088](#)].
- [319] S. Saito, K. Ichiki and A. Taruya, *Probing polarization states of primordial gravitational waves with CMB anisotropies*, *JCAP* **09** (2007) 002 [[0705.3701](#)].
- [320] L. Sorbo, *Parity violation in the Cosmic Microwave Background from a pseudoscalar inflaton*, *JCAP* **06** (2011) 003 [[1101.1525](#)].
- [321] B. Thorne, T. Fujita, M. Hazumi, N. Katayama, E. Komatsu and M. Shiraishi, *Finding the chiral gravitational wave background of an axion-SU(2) inflationary model using CMB observations and laser interferometers*, *Phys. Rev. D* **97** (2018) 043506 [[1707.03240](#)].
- [322] N. Seto and A. Taruya, *Measuring a parity violation signature in the early universe via ground-based laser interferometers*, *Phys. Rev. Lett.* **99** (2007) 121101 [[0707.0535](#)].
- [323] J.L. Cook and L. Sorbo, *Particle production during inflation and gravitational waves detectable by ground-based interferometers*, *Phys. Rev. D* **85** (2012) 023534 [[1109.0022](#)].
- [324] J. Crowder and N.J. Cornish, *Beyond LISA: Exploring future gravitational wave missions*, *Phys. Rev. D* **88** (2013) 083005 [[1307.5330](#)].
- [325] J. Chen, C. Liu, Y.-L. Zhang and G. Wang, *Alternative LISA-TAIJI networks: Detectability of parity violation in stochastic gravitational wave background*, *Phys. Rev. D* **111** (2025) 084026 [[2412.18420](#)].
- [326] G. Sato-Polito and M. Kamionkowski, *Pulsar-timing measurement of the circular polarization of the stochastic gravitational-wave background*, *Phys. Rev. D* **106** (2022) 023004 [[2111.05867](#)].
- [327] T. Kurita, D. Jamieson, E. Komatsu and F. Schmidt, *Parity Violation in Galaxy Shapes: Primordial Non-Gaussianity*, [2509.08787](#).
- [328] O.H.E. Philcox, *Probing parity violation with the four-point correlation function of BOSS galaxies*, *Phys. Rev. D* **106** (2022) 063501 [[2206.04227](#)].
- [329] J. Hou, Z. Slepian and R.N. Cahn, *Measurement of parity-odd modes in the large-scale four-point correlation function of SDSS BOSS galaxies*, *Mon. Not. Roy. Astron. Soc.* **522** (2023) 5701 [[2206.03625](#)].
- [330] A. Krolewski, S. May, K. Smith and P. Hopkins, *No evidence for parity violation in BOSS*, *JCAP* **08** (2024) 044 [[2407.03397](#)].
- [331] Z. Slepian et al., *Measurement of parity-violating modes of the DESI year 1 luminous red galaxies four-point correlation function*, *arXiv e-prints* (2025) [[2508.09133](#)].
- [332] E. Witten, *Cosmic separation of phases*, *Phys. Rev. D* **30** (1984) 272.
- [333] C.J. Hogan, *Gravitational radiation from cosmological phase transitions*, *Mon. Not. R. Astron. Soc.* **218** (1986) 629.

- [334] M. Kamionkowski, A. Kosowsky and M.S. Turner, *Gravitational radiation from first-order phase transitions*, *Physical Review D* **49** (1994) 2837.
- [335] R. Aureda, M. Maggiore, A. Nicolis and A. Riotto, *Gravitational waves from electroweak phase transitions*, *Nuclear Physics B* **631** (2002) 342.
- [336] C. Caprini, R. Durrer and G. Servant, *Gravitational wave generation from bubble collisions in first-order phase transitions*, *Physical Review D* **77** (2008) 124015.
- [337] P. Schwaller, *Gravitational waves from a dark phase transition*, *Phys. Rev. Lett.* **115** (2015) 181101 [[1504.07263](#)].
- [338] M. Breitbach, J. Kopp, E. Madge, T. Opferkuch and P. Schwaller, *Dark, cold, and noisy: Constraining secluded hidden sectors with gravitational waves*, *JCAP* **07** (2019) 007 [[1811.11175](#)].
- [339] D. Croon et al., *Classifying dark sectors that give rise to a first-order phase transition*, *JHEP* **08** (2018) 203 [[1806.02332](#)].
- [340] Y. Nakai, M. Suzuki, F. Takahashi and M. Yamada, *Gravitational waves and dark radiation from dark phase transition*, *Phys. Rev. D* **102** (2020) 083521 [[2009.09754](#)].
- [341] R. Pasechnik, M. Reichert, F. Sannino and Z.-W. Wang, *Gravitational waves from composite dark sectors*, *JHEP* **02** (2024) 159 [[2309.16755](#)].
- [342] C. Caprini and R. Durrer, *Gravitational waves from stochastic relativistic sources: Primordial magnetic fields*, *Phys. Rev. D* **65** (2001) 023517.
- [343] C. Caprini and R. Durrer, *Gravitational wave production from primordial helical magnetic fields*, *Phys. Rev. D* **74** (2006) 063521.
- [344] C. Caprini, R. Durrer and G. Servant, *The stochastic gravitational wave background from turbulence and magnetic fields generated by a first-order phase transition*, *Journal of Cosmology and Astroparticle Physics* **2009** (2009) 024 [[0909.0622](#)].
- [345] M. Hindmarsh, S.J. Huber, K. Rummukainen and D.J. Weir, *Numerical simulations of acoustically generated gravitational waves at a first-order phase transition*, *Physical Review D* **92** (2015) 123009.
- [346] M. Hindmarsh, S.J. Huber, K. Rummukainen and D.J. Weir, *Shape of the acoustic gravitational wave power spectrum from a first-order phase transition*, *Physical Review D* **96** (2017) 103520.
- [347] C. Caprini et al., *Science with the space-based interferometer eLISA. II: Gravitational waves from cosmological phase transitions*, *Journal of Cosmology and Astroparticle Physics* **2016** (2016) 001.
- [348] A. Mazumdar and G. White, *Review article: Cosmic phase transitions and their gravitational-wave signatures*, *Reports on Progress in Physics* **86** (2023) 122901.
- [349] P. Simakachorn, *Charting Cosmological History and New Particle Physics with Primordial Gravitational Waves*, Ph.D. thesis, U. Hamburg (main), Hamburg U., 2022.
- [350] T.W.B. Kibble, *Topology of cosmic domains and strings*, *Journal of Physics A* **9** (1976) 1387.
- [351] A. Vilenkin and E.P.S. Shellard, *Cosmic Strings and Other Topological Defects*, Cambridge University Press, Cambridge, UK (1994).
- [352] A. Vilenkin, *Gravitational radiation from cosmic strings*, *Phys. Lett. B* **107** (1981) 47.

- [353] R.H. Brandenberger, A. Albrecht and N. Turok, *Gravitational Radiation From Cosmic Strings and the Microwave Background*, *Nucl. Phys. B* **277** (1986) 605.
- [354] R. Brandenberger, *Topological defects and structure formation*, *Int. J. Mod. Phys. A* **9** (1994) 2117.
- [355] T. Vachaspati and A. Vilenkin, *Gravitational radiation from cosmic strings*, *Phys. Rev. D* **31** (1985) 3052.
- [356] B. Allen and E.P.S. Shellard, *Gravitational radiation from cosmic strings*, *Phys. Rev. D* **45** (1992) 1898.
- [357] T. Damour and A. Vilenkin, *Gravitational wave bursts from cosmic strings*, *Phys. Rev. Lett.* **85** (2000) 3761.
- [358] J.J. Blanco-Pillado, K.D. Olum and X. Siemens, *New limits on cosmic strings from gravitational wave observation*, *Phys. Lett. B* **778** (2018) 392 [[1709.02434](#)].
- [359] E. Witten, *Superconducting strings*, *Nucl. Phys. B* **249** (1985) 557.
- [360] P. Auclair, S. Blasi, V. Brdar and K. Schmitz, *Gravitational waves from current-carrying cosmic strings*, *JCAP* **2023** (2023) 009 [[2207.03510](#)].
- [361] P. Auclair et al., *Probing the gravitational wave background from cosmic strings with LISA*, *JCAP* **04** (2020) 034 [[1909.00819](#)].
- [362] Y. Gouttenoire, G. Servant and P. Simakachorn, *Beyond the Standard Models with Cosmic Strings*, *JCAP* **07** (2020) 032 [[1912.02569](#)].
- [363] K. Schmitz and T. Schröder, *Gravitational waves from cosmic strings for pedestrians*, [2412.20907](#).
- [364] N. Turok, *Global texture as the origin of cosmic structure*, *Physical Review Letters* **63** (1989) 2625.
- [365] R. Durrer, A. Gangui and M. Sakellariadou, *The CMB anisotropies from scaling seeds*, *Physical Review D* **59** (1999) 103501.
- [366] J. Preskill, *Semilocal defects*, *Physical Review D* **46** (1992) 4218.
- [367] T. Vachaspati and A. Vilenkin, *Evolution of cosmic string loops*, *Physical Review D* **35** (1987) 1131.
- [368] S. Blasi, A. Mariotti, A. Sevrin, T. Van Proeyen and A. Van Steenhuyse, *Domain-wall induced cosmological phase transitions and gravitational waves*, *JCAP* **2023** (2023) 051 [[2210.06432](#)].
- [369] K. Kohri and T. Terada, *Solar-Mass Primordial Black Holes Explain NANOGrav Hint of Gravitational Waves*, *Phys. Lett. B* **813** (2021) 136040 [[2009.11853](#)].
- [370] S. Hawking, *Gravitationally collapsed objects of very low mass*, *Monthly Notices of the Royal Astronomical Society* **152** (1971) 75.
- [371] S. Bird, I. Cholis, J.B. Muñoz, Y. Ali-Haïmoud, M. Kamionkowski, E.D. Kovetz et al., *Did LIGO detect dark matter?*, *Physical Review Letters* **116** (2016) 201301.
- [372] LISA COSMOLOGY WORKING GROUP collaboration, *Primordial black holes and their gravitational-wave signatures*, *Living Rev. Rel.* **28** (2025) 1 [[2310.19857](#)].
- [373] C. Yuan and Q.-G. Huang, *A topic review on probing primordial black hole dark matter with scalar induced gravitational waves*, *iScience* **24** (2021) 102860.